

**FACULTY
OF MATHEMATICS
AND PHYSICS**
Charles University

DOCTORAL THESIS

Michal Kloc

**Quantum phase transitions in systems with a
finite number of degrees of freedom**

Institute of Particle and Nuclear Physics

Supervisor of the doctoral thesis: prof. RNDr. Pavel Cejnar, Dr., DSc.

Study programme: Physics

Study branch: Nuclear Physics

Prague 2018

I declare that I carried out this doctoral thesis independently, and only with the cited sources, literature and other professional sources.

I understand that my work relates to the rights and obligations under the Act No. 121/2000 Sb., the Copyright Act, as amended, in particular the fact that the Charles University has the right to conclude a license agreement on the use of this work as a school work pursuant to Section 60 subsection 1 of the Copyright Act.

Prague, 29th June 2018

signature of the author

Title: Quantum phase transitions in systems with a finite number of degrees of freedom

Author: Michal Kloc

Institute: Institute of Particle and Nuclear Physics

Supervisor: prof. RNDr. Pavel Cejnar, Dr., DSc., Institute of Particle and Nuclear Physics

Abstract: In the thesis we investigate and classify critical phenomena in the extended Dicke model (EDM) which describes the interaction between two-level atoms and a single-mode bosonic field (schematic model for cavity quantum electrodynamics). The model belongs to the class of so-called finite models, which keep the number of degrees of freedom f constant independently on the size of the system N . The important property of these systems is that the thermodynamic limit $N \rightarrow \infty$ coincides with the classical limit $\hbar \rightarrow 0$. This allows us to study various quantum critical phenomena, in particular the ground-state quantum phase transitions (QPTs) and the excited-state quantum phase transitions (ESQPTs), by means of semiclassical methods.

Using the semiclassical approach we identify and classify the QPTs and ESQPTs in various settings of the EDM and make a link to thermal phase transitions. We study the entanglement properties of both the ground state and the excited states as a function of the atom-field interaction strength. In the integrable version of the EDM we make a link between the ESQPT and monodromy, and discuss its effect on classical dynamics. The fate of monodromy under a non-integrable perturbation is observed. The dynamical consequences of the ESQPTs are examined using quantum quenches. The influence of the ESQPTs on quench dynamics is shown to depend on the quench protocol, type of the ESQPT and on the degree of chaoticity in the system.

Keywords: Quantum phase transitions, Excited-state quantum phase transitions, Extended Dicke model, Entanglement, Quench dynamics, Monodromy

Acknowledgements

In the first place, I would like to thank Prof. Pavel Cejnar and Dr. Pavel Stránský for being great mentors with enough patience and willingness to discuss physics at any time and any place. I also appreciate the friendly atmosphere in our working group which made many of the scientific problems easier to handle.

I am very grateful to my family and close friends. Your endless support helped me through the times when ‘things simply didn’t go according to the plans’.

Last but not least I would like to thank to my colleagues from the Institute of Particle and Nuclear Physics for the supportive environment. Special thanks for this then go to two of my colleagues and friends Stano Štefánik and Tomáš Kadavý.

Contents

Introduction	4
1 Criticality in many-body quantum systems	5
1.1 Quantum phase transitions	5
1.1.1 General features	5
1.1.2 QPTs in condensed matter physics	5
1.1.3 QPTs in nuclear and atomic physics	6
1.1.4 Finite models	6
1.1.5 Mean-field description	6
1.2 Excited-state quantum phase transitions	7
1.2.1 Level density	7
1.2.2 Stationary points of the classical Hamiltonian	8
1.2.3 Related concepts	8
2 Extended Dicke model	9
2.1 The Hamiltonian	9
2.2 Conserved quantities	9
2.3 Limit regimes	10
2.3.1 Dicke model	10
2.3.2 Tavis-Cummings model	10
2.4 Semiclassical form of the Hamiltonian	11
2.4.1 Full model	11
2.4.2 Tavis-Cummings limit	12
2.5 Phase transitions	12
2.5.1 TPTs	12
2.5.2 QPTs	12
2.5.3 ESQPTs	13
2.5.4 Quantum phases	15
2.6 Critical subspace of Tavis-Cummings model	15
2.7 Experimental relevance	17
3 ESQPT-related effects in EDM	18
3.1 Monodromy	18
3.1.1 Energy-momentum map of Tavis-Cummings model	18
3.1.2 Monodromy point	18
3.1.3 Physical interpretation of quantum monodromy	19

3.1.4	Semiclassical viewpoint	20
3.1.5	Fate of monodromy under non-integrable perturbation	20
3.2	Bipartite entanglement	20
3.2.1	Entanglement entropy	20
3.2.2	Entanglement of formation	21
3.2.3	Concurrence	21
3.2.4	Critical entanglement in a QPT	22
3.2.5	Entanglement in excited states of EDM	22
3.2.6	Participation ratio	23
3.3	Quantum quench dynamics	24
3.3.1	Non-adiabatic dynamics and ESQPTs	24
3.3.2	Survival probability	24
3.3.3	Strength function	24
3.3.4	Autocorrelation function	25
3.3.5	Quench protocols in the phase diagram	25
3.3.6	Quenches from the unperturbed ground state	26
3.3.7	Quenches from the superradiant ground state	27
3.3.8	Observables	28
Conclusion		30
A Convergence of the spectrum		31
B Superradiance		33
B.1	Dynamic superradiance - coherent spontaneous emission	33
B.2	Redistribution of decay widths	34
B.3	Equilibrium superradiance	35
C Polaron transformation		37
D Stationary points of the classical Hamiltonian		39
D.1	General $\delta \neq 0$ case	39
D.2	Critical M -subspace of the $\delta = 0$ model	40
E Computation of <i>concurrence</i> in EDM		42
F Reprint: Quantum phases and entanglement properties of an extended Dicke model		44
E.1	Main Achievements	44
G Reprint: Monodromy in Dicke superradiance		72
G.1	Main Achievements	72
H Reprint: Quantum quench dynamics in Dicke superradiance models		89
H.1	Main Achievements	89
Bibliography		104
List of Abbreviations		108

Introduction

Phase transitions belong to the class of physical phenomena which are a part of an every-day life experience. If an ice cube is thrown into a glass of water at the room temperature, it starts melting due to the increasing thermal fluctuations of the molecules. When these fluctuations become sufficiently strong, the molecules can break free from the crystalline lattice, hence the phase becomes liquid. To highlight the fact that the transition is governed by the temperature T , one often uses an explicit term *thermal* phase transition (TPT).

Quantum phase transitions (QPTs) are, however, not governed by the temperature as they affect only the ground state of a quantum system at $T = 0$ K. As the thermal movement is not present anymore, these are the quantum fluctuations (determined by Heisenberg uncertainties) which are responsible for the phase transition. We usually consider parameter-dependent Hamiltonians of the linear type $H(\lambda) = H_0 + \lambda V$ where a tunable (non-thermal) parameter λ controls the strength of a perturbation V to a free Hamiltonian H_0 . For some systems there exists a certain critical value λ_c for which the energy of the ground state changes abruptly. This change becomes truly non-analytic in the thermodynamic (infinite-size) limit of the system. We say that the system undergoes a QPT at $\lambda = \lambda_c$ and apart from the eigenenergy, it affects various properties of the ground state.

In so-called *finite systems*, where the number of degrees of freedom f is independent on the system's size, the mean-field description becomes exact in thermodynamic limit. A QPT is associated with a sudden structural change of the mean field where a new global minimum is formed. Various stationary points may also appear in the region of excitation energies. These give rise to the excited-state quantum phase transitions (ESQPTs) where the (smoothed) energy dependence of the observables changes abruptly and the level density $\rho(E)$ has a singularity in $(f - 1)$ st energy derivative.

The aim of the PhD. thesis is to put the author's main publications (Refs. [1, 2, 3]) into a broader context of current knowledge of quantum critical phenomena in many-body systems and to summarize the main results. The information in the thesis is intended to be rather dense but hopefully clear with references to the relevant literature.

The structure of the thesis is as follows: In Chapter 1 we introduce a concept of ground-state QPTs and ESQPTs. The following Chapter 2 contains a detailed description of the Extended Dicke model showing multiple ESQPTs whose effects on the system's properties are further discussed in Chapter 3. Some more technical parts are presented in Appendices in order to keep the fluency of the main text. We also enclose the reprints of the author's significant articles.

Criticality in many-body quantum systems

1.1 Quantum phase transitions

1.1.1 General features

Consider a many-body system described by the Hamiltonian $H(\{\lambda_i\})$ depending on some control parameters $\{\lambda_i\}$. A quantum phase transition (QPT) occurs when a smooth variance of these parameters leads to a sudden change of the properties of the ground state [4, 5, 6]. The abruptness of the change becomes truly non-analytic in thermodynamic limit $N \rightarrow \infty$ where N denotes the number of particles. Suppose $E_{\text{g.s.}}(\lambda)$ is the energy of the ground state as it evolves with a control parameter λ (for simplicity we consider here only one such parameter). An Ehrenfest classification can be used in context of QPTs: *first order* phase transitions have discontinuity if the first derivative of $E_{\text{g.s.}}(\lambda)$ with respect to the control parameter, *second order* phase transitions have singularity in the second derivative etc. In the case of a divergence in the k -th derivative (instead of discontinuity) the transition has no Ehrenfest classification.

1.1.2 QPTs in condensed matter physics

The best studied systems with QPTs are the spin models of magnetization in condensed matter physics. One such archetypal example is the Ising model in transverse field [7, 8]

$$H_{\text{TI}} = -\Gamma \sum_i \sigma_z^i - J \sum_{\langle ij \rangle} \sigma_x^i \sigma_x^j \quad (1.1)$$

where $\{\sigma_x^i, \sigma_y^i, \sigma_z^i\}$ are the Pauli matrices acting on the spin site i , the symbol $\langle i, j \rangle$ in the summation indicates the nearest-neighbor interaction in the spin chain, J and Γ are real parameters.

The original Ising model with $\Gamma = 0$ shows a TPT from magnetic order (all spins aligned) to disorder where the total magnetization is zero. The magnetic order at $T = 0$ can also be broken by adding the the transverse field while the temperature remains unchanged. If the strength of the external field reaches the critical value $\Gamma_c = J$, the QPT takes place.

1.1.3 QPTs in nuclear and atomic physics

In nuclear physics, QPTs have been discussed in context of equilibrium shapes of nuclei [9]. However, one has to keep in mind that nuclei are strictly finite objects composed of several nucleons so QPTs appear only as precursors. The relevant Interacting Boson Model (IBM) [10] is based on the dynamical algebra $U(6)$ composed by a scalar boson s and five-component (spin 2) boson d where the components are marked as d_m , $m = (-2, -1, 0, 1, 2)$. The Hamiltonian reads as

$$H_{\text{IBM}} = \eta(d^\dagger \cdot d) - \frac{1-\eta}{N} Q_m^{(2)} \cdot Q_m^{(2)}, \quad Q_m^{(2)} \equiv d_m^\dagger s + s^\dagger d_m + \chi d^\dagger \cdot d \quad (1.2)$$

where $\eta \in [0, 1]$ is the control parameter, $N = s^\dagger s + \sum_m d_m^\dagger d_m$ is the conserved total number of bosons, $Q_m^{(2)}$ is a quadrupole operator depending on $\chi \in \left[-\frac{\sqrt{7}}{2}, \frac{\sqrt{7}}{2}\right]$. The model describes shape transitions in the isotopic chains of some even-even nuclei (the *bosons* in the model are the pairs of the nucleons) where the neutron number acts as a control parameter [11].

A similar type of an algebraic model with lower dynamical algebras are relevant for molecular and atomic physics [12, 13]. We mention the simplest $U(2)$ -based Lipkin-Meshkov-Glick (LMG) [14] where the d bosons are pseudoscalars. After a proper energy shift and considering $\chi = 0$, we can employ Schwinger mapping and rewrite the Hamiltonian using collective pseudospin operators as

$$H_{\text{LMG}} = -hJ_z - \frac{\gamma}{N} J_x^2, \quad J_x = \frac{1}{2}(d^\dagger s + s^\dagger d), \quad J_z = \frac{1}{2}(d^\dagger d - s^\dagger s), \quad (1.3)$$

where the new parameters are $h = \eta$, $\gamma = 4(1 - \eta)$. LMG model can be also obtained from the Ising model (1.1) by considering infinite spin-spin interaction.

In the next Chapter we will describe in detail the Dicke model of superradiance [15] widely used in quantum optics and atomic physics.

1.1.4 Finite models

We will refer to a class of models as *finite* if the number of degrees of freedom f stays constant when increasing the size of the system, i.e., when approaching the thermodynamic limit [16]. Such models exhibit long-range interactions and describe some collective properties of the system.

A unique feature of these models is that the thermodynamic limit $N \rightarrow \infty$ where N is the size parameter (mostly the number of particles in the system) coincides with the classical limit. Indeed, the Hamiltonian of the model can be generally defined in terms of operators $H(\mathcal{G}_i)$ forming a certain dynamical algebra $[\mathcal{G}_i, \mathcal{G}_j] = f_{ijk}\mathcal{G}_k$ where f_{ijk} is its structure constant. After scaling the Hamiltonian with N it can be rewritten using the operators $g_i = \mathcal{G}_i/N^\kappa$ (where $\kappa > 0$) satisfying $H/N = H(g_i)$. In the limit $N \rightarrow \infty$ the commutation relation of the rescaled operators vanishes $[g_i, g_j] \rightarrow 0$. Now we can identify system's Planck constant with N^{-1} . By making the system larger, the 'quantumness' is being suppressed and we approach the classical limit with commuting variables.

1.1.5 Mean-field description

It is known that for collective (finite) models the mean field predicts a QPT exactly [9, 17]. This approach supposes that individual particles act independently on each

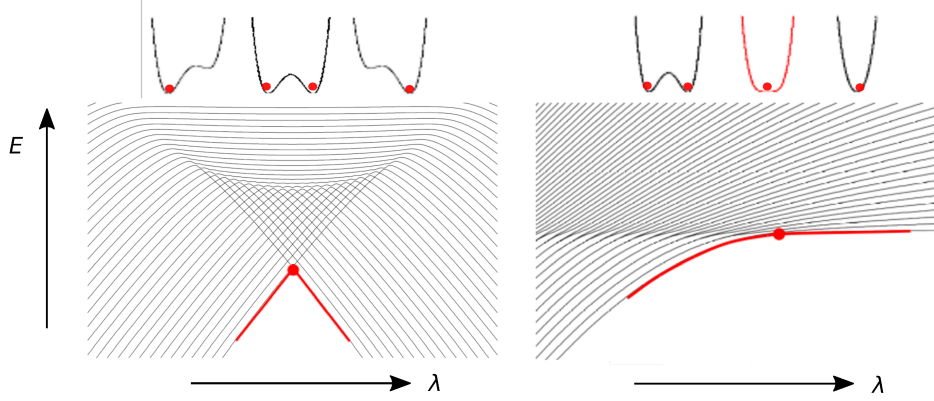


Figure 1.1: A sketch of a one-dimensional mean-field potential as it changes with parameter λ and respective quantum spectra in the plane $\lambda \times \text{Energy}$. Left panel corresponds to the first order QPT, right panel corresponds to the second order QPT. ESQPTs are visible among the excited states either as avoided crossings separating areas with different mean average slope of the levels (left panel) or as level bunching (right panel).

other and the evolution is given by a certain one-body Hamiltonian. The origin of a QPT can be understood as a structural change in the mean field with control parameters.

In Fig. [1.1](#) we show a sketch of quantum spectra related to one-dimensional potential as a function of λ . Left panel depicts a first order QPT induced by two wells moving against one another, so at the critical coupling (both wells are degenerate) the ground state is swapped. A second order QPT (right panel) appears when the respective potential undergoes a structural change from quadratic to a double-well form.

1.2 Excited-state quantum phase transitions

1.2.1 Level density

The level density $\rho(E, \lambda)$ of a bounded system as a function of excitation energy E and a control parameter λ is simply defined as

$$\rho(E, \lambda) = \sum_i \delta(E - E_i(\lambda)) \quad (1.4)$$

where $E_i(\lambda)$ are the eigenenergies. It can be decomposed into a smooth and oscillatory part $\rho(E, \lambda) = \bar{\rho}(E, \lambda) + \tilde{\rho}(E, \lambda)$. As the oscillatory part averages to zero over energy $\langle \tilde{\rho}(E, \lambda) \rangle_E = 0$, the mean energy dependence of the level density is captured by its smooth component $\bar{\rho}(E, \lambda)$. It can be obtained from the real spectrum by applying some smoothening function to $\rho(E, \lambda)$ or it can be computed semi-classically in the $N \rightarrow \infty$ limit. Indeed, the semi-classical level density is defined as

$$\rho_{\text{cl}}(E, \lambda) = \left(\frac{1}{2\pi}\right)^f \int \delta(E - H_{\text{cl}}(\mathbf{q}, \mathbf{p}, \lambda)) d^f \mathbf{q} d^f \mathbf{p} = \left(\frac{1}{2\pi}\right)^f \frac{\partial}{\partial E} \int_{E \leq H_{\text{cl}}} d^f \mathbf{q} d^f \mathbf{p} \quad (1.5)$$

where H_{cl} is a classical Hamiltonian which is a function of f -dimensional vectors of conjugate positions and momenta \mathbf{q}, \mathbf{p} and a coupling parameter λ .

1.2.2 Stationary points of the classical Hamiltonian

We suppose that H_{cl} is a smooth function. Further we define $2f$ -dimensional vector $\mathbf{x} = (\mathbf{q}, \mathbf{p})$ and rewrite (1.5) using substitution formula for delta function

$$\rho_{\text{cl}}(E, \lambda) = \left(\frac{1}{2\pi}\right)^f \int \frac{\delta(\mathbf{x}_0 - \mathbf{x})}{|\nabla_{2f} H_{\text{cl}}(\mathbf{x}_0, \lambda)|} d^{2f} \mathbf{x} \quad (1.6)$$

where \mathbf{x}_0 satisfies $H_{\text{cl}}(\mathbf{x}_0, \lambda) = E$ and ∇_{2f} is $2f$ -dimensional gradient.

From Eq. (1.6) we see that whenever the classical Hamiltonian has a stationary point $|\nabla_{2f} H_{\text{cl}}(\mathbf{x}_0, \lambda)| = 0$, the level density shows a singularity. These singularities in level density always appear in $(f-1)$ st energy derivative and are referred to as excited-state quantum phase transitions (ESQPTs) [18, 19, 20, 21, 22, 23, 24]. In quantum spectra of $f = 1$ systems with finite N , the precursors of ESQPTs can be traced directly from the level dynamics (the singularity appears already in the zeroth derivative of the level density). In Fig. 1.1) the examples are sketched. Similarly as in the case of QPTs, the ESQPTs are fully pronounced only in the infinite-size limit $N \rightarrow \infty$ as then $\bar{\rho} \rightarrow \rho_{\text{cl}}$.

ESQPTs induced by non-degenerate (locally quadratic) stationary points are classified with a pair of numbers (f, r) - number of degrees of freedom of the system and the number of negative Hessian eigenvalues of the stationary point [24]. The inequality $r \leq 2f$ must hold, however in common systems we usually have $r \leq f$.

1.2.3 Related concepts

The theory of the ESQPTs is rather general and does not assume any concrete physical system. In crystals the divergence in the density of states is known as *Van Hove singularity* [25] and it can be observed for example in twisted graphene layers [26].

In molecular physics, the term *quantum monodromy* is used as an analog of an ESQPT [27, 28, 29, 30, 31]. In highly excited spectra of some quasi-linear molecules one can recognize a transition from rotational to vibrational motion in a so-called quantum energy-momentum map which indicates a structural change between bent and linear conformations. We will come back to this topic in Chapter 3) where we will provide a more detailed description.

In $f = 1$ classical dynamics a similar concept to the ESQPT is called the *separatrix* [32, 33]. It is the trajectory which separates bound and unbound types of motion in the configuration space. A simple example is a pendulum where the increasing energy leads to the swings along the whole circle. The separatrix corresponds to the motion with the precise energy of the local maximum of the classical potential (the unstable equilibrium).

Extended Dicke model

2.1 The Hamiltonian

Consider an ensemble of N two-level atoms with transition energy ω_0 interacting with a monochromatic light (with energy ω) in a cavity. We assume that the atomic condensate is localized in a small volume compared to the wavelength of light, therefore the dipole approximation can be employed (assumption that all atoms have the same phase when interacting with the field). The atoms can be represented as a chain of spin- $\frac{1}{2}$ sites with a spin-flip frequency ω_0 . We define the collective pseudospin operators $J_\alpha = \sum_i \frac{1}{2} \sigma_\alpha^i$ where index $i = 1, 2, \dots, N$ runs through individual spin sites, σ_α^i is the Pauli matrix at site i with $\alpha = \{+, -, z\}$. The collective ladder operators are defined as $J_\pm = \sum_i \sigma_\pm^i$ where σ_\pm^i operator flips the i -th atom.

The respective Hamiltonian of an extended Dicke model (EDM) can then be written in the form [1, 15, 34, 35]

$$H(\lambda, \delta) = \omega b^\dagger b + \omega_0 J_z + \frac{\lambda}{\sqrt{N}} [b^\dagger J_- + b J_+ + \delta (b^\dagger J_+ + b J_-)], \quad (2.1)$$

where b, b^\dagger are the annihilation and creation operators of light quanta and λ, δ are tunable parameters. The former, λ , controls the overall strength of the interaction. Its values range from $\lambda = 0$ to, in principle, $\lambda \rightarrow \infty$. The role of parameter $\delta \in [0, 1]$ is discussed below. A comment on the numerical solution of (2.1) can be found in Appendix A.

2.2 Conserved quantities

The Hamiltonian conserves the squared pseudospin $J^2 = J_x^2 + J_y^2 + J_z^2$ with eigenvalues $j(j+1)$ where j is integer for N even and half-integer for N odd. The full Hilbert space of atoms \mathcal{H}_A spans dimension 2^N . However the dynamics can be separately examined in different J^2 conserving subspaces $\mathcal{H}_A^{j,l}$ (we call these single- j subspaces). So we can decompose the full Hilbert space [1, 36, 37, 38]

$$\mathcal{H}_A = \bigoplus_{j=0 \text{ or } \frac{1}{2}}^{\frac{N}{2}} \left(\bigoplus_{l=1}^{R_j} \mathcal{H}_A^{j,l} \right), \quad R_j = \frac{N!(2j+1)}{(\frac{N}{2}+j+1)!(\frac{N}{2}-j)!}, \quad (2.2)$$

where superscript l denotes how many replicas of the given single- j subspace exist in the decomposition (their number is R_j) which is given by the exchange symmetry of the atomic components.

In a general single- j subspace, $2j$ atoms can be independently excited while the remaining $N - 2j$ act only as the ‘observers’ and compensate each other (have total spin equal to zero). In most cases the subspace of maximal $2j = N$ is considered as this captures the maximal collectivity of the atomic response (no ‘observers’). In the thesis we will consider this subspace if not explicitly stated otherwise.

The Hamiltonian also has a parity symmetry for any values of the parameters $[H(\lambda, \delta), \Pi] = 0$ where $\Pi = e^{i\pi(b^\dagger b + J_z + j)}$.

2.3 Limit regimes

2.3.1 Dicke model

If we fix parameter $\delta = 1$, the Hamiltonian (2.1) takes the form of the original Dicke model [15]

$$H_D(\lambda) = \omega b^\dagger b + \omega_0 J_z + \frac{\lambda}{\sqrt{N}}(J_+ + J_-)(b + b^\dagger) = \omega b^\dagger b + \omega_0 J_z + \frac{2\lambda J_x}{\sqrt{N}}(b + b^\dagger), \quad (2.3)$$

where we used identity $J_x = \frac{1}{2}(J_+ + J_-)$. The model was proposed to describe *dynamic superradiance* [39, 40], i.e., non-exponential coherent decay of N radiators with a peak of maximal intensity $\propto N^2$, see Appendix B. The related phenomena have also been described in nuclei and other mesoscopic systems, see Refs. [41, 42, 43, 44].

Later a TPT [37, 38] and QPT [45] were described in the model. When increasing either temperature or the coupling strength, the system enters the superradiant phase where the ground state acquires macroscopic excitations of both field and the atoms (sometimes referred to as a *superradiant phase transition*).

There are two analytically solvable limits of the model. The trivial one $\lambda = 0$ and the ultra-strong limit $\lambda \rightarrow \infty$. In the latter limit the Hamiltonian (2.3) can be transformed to the form with decoupled atomic and field variables (see Appendix C)

$$H_2^{\lambda \rightarrow \infty} = \omega b^\dagger b - \frac{(2\lambda)^2}{\omega N} J_z^2. \quad (2.4)$$

Note that Hamiltonian (2.4) gives rise to twofold degenerate states with $\pm m$ which are the eigenvalues of J_z .

2.3.2 Tavis-Cummings model

Rotating wave approximation

By taking $\delta = 0$, the so-called *counter-rotating* terms $b^\dagger J_+$, $b J_-$ in the interaction part of (2.1) disappear and the Hamiltonian takes the form of the Tavis-Cummings model [46]

$$H_{TC}(\lambda) = \omega b^\dagger b + \omega_0 J_z + \frac{\lambda}{\sqrt{N}}(b J_+ + b^\dagger J_-). \quad (2.5)$$

This Hamiltonian is obtained by the *rotating wave approximation* (RWA) of the full Dicke model (2.3). In RWA the fast oscillating terms are neglected as they average to zero over time. Indeed, when transformed to interaction picture $H_D \rightarrow H_D^I$ the evolution of the operators is given by the free part of (2.3) $H_0 = \omega b^\dagger b + \omega_0 J_z$. For example the annihilation operator b evolves in the interaction picture as

$$\frac{db}{dt} = i[H_0, b] = i\omega[b^\dagger b, b] = -i\omega b \Rightarrow b(t) = b(0)e^{-i\omega t}. \quad (2.6)$$

Similarly we can obtain

$$b^\dagger(t) = b^\dagger(0)e^{i\omega t}, \quad J_-(t) = J_-(0)e^{-i\omega_0 t}, \quad J_+(t) = J_+(0)e^{i\omega_0 t}. \quad (2.7)$$

The counter-rotating terms oscillate with frequency $\omega + \omega_0$ while the terms $b^\dagger J_-$ and $b J_+$ have frequency $\pm\Delta\omega$ where we set $\Delta\omega \equiv \omega - \omega_0$. Therefore in the nearly resonant regimes $\omega \approx \omega_0$ and for small values of λ , the fast evolution of the counter-rotating terms can be neglected compared to the slow evolution of the remaining terms. If we move back to the Schrödinger picture, we arrive at (2.5).

M -subspaces

The Tavis-Cummings Hamiltonian acquires additional symmetry which effectively reduces the number of degrees of freedom to $f = 1$ (unlike any other $\delta \neq 0$ case where $f = 2$). Indeed, the operator $\mathcal{M} = b^\dagger b + J_z + j$ does commute with the Hamiltonian (2.5) $[H_{TC}, \mathcal{M}] = 0$.

One can express \mathcal{M} in the eigenbasis $|m, n\rangle$ of the $\lambda = 0$ limit where m is the pseudo-spin z -projection and n denotes the total number of photons. We then obtain

$$M = n + m + j = n + n^*, \quad (2.8)$$

where M are the eigenvalues of \mathcal{M} and $n^* = m + j$ denotes the total number of excitations in the atomic subsystem. So in the Tavis-Cummings limit $\delta = 0$ the respective Hilbert space splits into mutually non-interacting subspaces due to the symmetry (2.8). These are numbered by M (let us note that M takes values of integer numbers or zero) and the dynamics can be studied separately in any M -subspace whose dimension is $d = \min(M + 1, N + 1)$ [1, 2].

2.4 Semiclassical form of the Hamiltonian

2.4.1 Full model

The semiclassical form of EDM Hamiltonian can be written as [35]

$$H_{cl}(\lambda, \delta) = \omega \frac{p^2 + x^2}{2} + \omega_0 j_z + \lambda \sqrt{j} \sqrt{1 - \frac{j_z^2}{j^2}} \left[(1 + \delta)x \cos \phi - (1 - \delta)p \sin \phi \right], \quad (2.9)$$

which is obtained from (2.1) by the mapping

$$\begin{aligned} (J_x, J_y, J_z) &\mapsto j(\sin \theta \cos \phi, \sin \theta \sin \phi, -\cos \theta), \\ (b, b^\dagger) &\mapsto \frac{1}{\sqrt{2}}(x + ip, x - ip), \end{aligned} \quad (2.10)$$

where (ϕ, θ) and (x, p) are the canonically conjugate variables associated with the atoms and the photons respectively. The z -projection of the pseudo-spin j_z in (2.9) is measured from the south pole of the Bloch sphere, so $j_z = -j \cos \theta$.

2.4.2 Tavis-Cummings limit

In the Tavis-Cummings limit $\delta = 0$, one degree of freedom can be effectively taken away by means of the following canonical transformation [1, 2]

$$\begin{pmatrix} x \\ p \\ \phi \\ j_z \end{pmatrix} \mapsto \begin{pmatrix} x' = x \cos \phi - p \sin \phi \\ p' = p \cos \phi + x \sin \phi \\ \phi' = \phi + j_z + (p^2 + x^2)/2 \\ M' = j_z + (p^2 + x^2)/2 \end{pmatrix}. \quad (2.11)$$

Considering the classical form of (2.8) we obtain $M' = M - j$. By inserting the new set of variable into Eq. (2.9) we obtain

$$H_{\text{cl}}^{\text{TC}} = (\omega - \omega_0) \frac{p'^2 + x'^2}{2} + \omega_0 M' + \lambda x' \sqrt{\frac{1}{j} \left[j^2 - \left(M' - \frac{p'^2 + x'^2}{2} \right)^2 \right]}. \quad (2.12)$$

2.5 Phase transitions

2.5.1 TPTs

In order to obtain standard thermodynamics in the sense of converging canonical and microcanonical description, one has to consider the all- j Hilbert space \mathcal{H}_A from (2.2) within which the thermodynamic limit implies also $f \rightarrow \infty$ [47]. A TPT to the superradiant phase can be then found in the model. The phase diagram in the plane $\lambda \times$ Temperature can be found in Ref. [1], see also Appendix B. A recent results on the connection between thermodynamical properties and the ESQPT in the Dicke model can be found in Refs. [48, 49].

2.5.2 QPTs

Now we return to the single- j subspace with $N = 2j$ where the number of degrees of freedom is fixed for any size of the system. If the coupling in the EDM reaches the critical value [1]

$$\lambda_c(\delta) = \frac{\sqrt{\omega\omega_0}}{1 + \delta}, \quad (2.13)$$

a QPT takes place. Indeed, for $\lambda < \lambda_c$ the expectation values (strictly in thermodynamic limit) in the ground state are $\langle b^\dagger b \rangle_{\text{g.s.}} = 0$, $\langle J_z \rangle_{\text{g.s.}} = -j$. This is the state with no photons and all atoms deexcited. However, for $\lambda > \lambda_c$ we obtain $\langle b^\dagger b \rangle_{\text{g.s.}} > 0$, $\langle J_z \rangle_{\text{g.s.}} > -j$ which shows that this *superradiant* ground state energetically favors non-zero excitations of both the atoms and the field [45].

The energy of the ground state as a function of the coupling parameter λ evolves according to the formula (see Appendix D)

$$\frac{E_{\text{g.s.}}}{\omega_0 j} = \begin{cases} -1 & \text{for } \lambda \in [0, \lambda_c), \\ -\frac{1}{2} \left(\frac{\lambda_c^2}{\lambda^2} + \frac{\lambda^2}{\lambda_c^2} \right) & \text{for } \lambda \in [\lambda_c, \infty), \end{cases} \quad (2.14)$$

2.5.3 ESQPTs

Computation of the level density

In order to detect ESQPTs we need to find stationary points of the classical Hamiltonian (2.9). This is performed in Appendix D. Here we show how to visualize the stationary points on the energy landscape on the pseudospin Bloch sphere.

We employ the following transformation of the field variables

$$\begin{pmatrix} x \\ p \end{pmatrix} \mapsto \begin{pmatrix} X = x + \frac{(1+\delta)\lambda}{\omega} \sqrt{j} \sqrt{1 - \frac{j_z^2}{j^2}} \cos \phi \\ P = p - \frac{(1-\delta)\lambda}{\omega} \sqrt{j} \sqrt{1 - \frac{j_z^2}{j^2}} \sin \phi \end{pmatrix}. \quad (2.15)$$

by which means we obtain the Hamiltonian with separated variables

$$H'_{\text{cl}} = \omega \frac{X^2 + P^2}{2} + \omega_0 j_z - \underbrace{\frac{\lambda^2}{\omega} \frac{j^2 - j_z^2}{2j}}_{h_{\text{cl}}(\phi, j_z)} (1 + 2\delta \cos 2\phi + \delta^2). \quad (2.16)$$

Due to the fact that the transformation (2.15) is volume-preserving (though not canonical) we can compute the level density using the new variables without changing the form of (1.5)

$$\begin{aligned} \rho(E) &= \frac{1}{(2\pi)^2} \int \delta(E - H'_{\text{cl}}) dX dP d\phi dj_z \\ &= \frac{1}{(2\pi)^2} \int \delta\left(E - \frac{\omega}{2}(X^2 + P^2) - h_{\text{cl}}(\phi, j_z)\right) dX dP d\phi dj_z. \end{aligned} \quad (2.17)$$

The shifted atomic variables can be integrated using the polar coordinates $X = R \cos \varphi$, $P = R \sin \varphi$ (they have the form of a simple oscillator with a constant level density)

$$\rho(E) = \frac{1}{(2\pi)^2} \int \delta\left(E - \frac{\omega}{2} R^2 - h_{\text{cl}}(\phi, j_z)\right) R dR d\varphi d\phi dj_z \quad (2.18)$$

$$= \frac{1}{2\pi\omega} \int \delta(R - R_0) dR d\phi dj_z \quad (2.19)$$

where $R_0 = \frac{1}{\omega} 2\sqrt{E - h_{\text{cl}}(\phi, j_z)}$. Such R_0 apparently exists only if $E > h_{\text{cl}}(\phi, j_z)$. Therefore we can write

$$\rho(E) = \frac{1}{(2\pi)^2} \int \Theta(E - h_{\text{cl}}(\phi, j_z)) d\phi dj_z, \quad (2.20)$$

where Θ is the Heaviside step function.

One can interpret the expression for level density (2.20) in the following way: The function $h_{\text{cl}}(\phi, j_z)$ sets energy landscape on the Bloch sphere (which changes with λ). The level density at energy E corresponds to the area of the sphere reachable with the given energy. It must also contain all information on the ESQPTs. By examining the stationary points of $h_{\text{cl}}(\phi, j_z)$ we can identify critical energies for different types of ESQPTs according to their (f, r) classification [24].

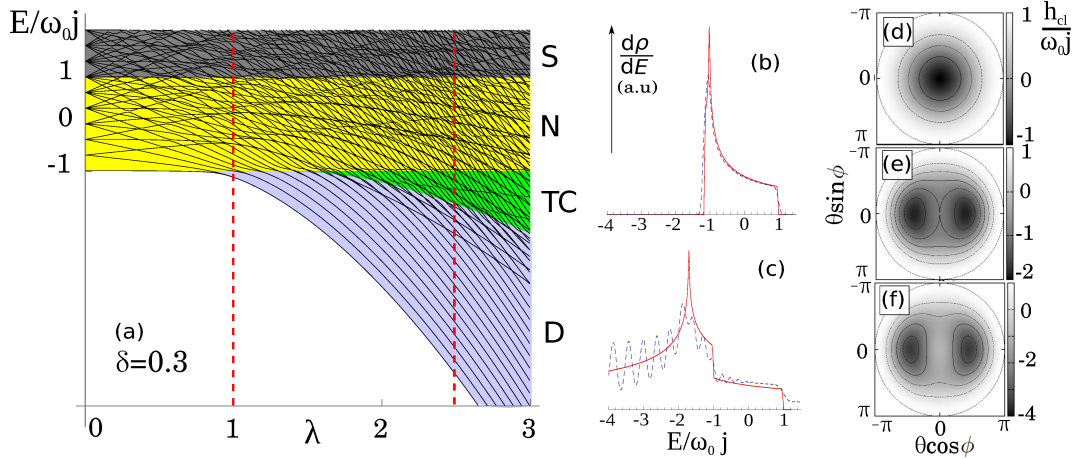


Figure 2.1: Panel (a): The evolution of energy levels with parameter λ of the EDM with $\delta = 0.3$, $j = 3$, $\omega = \omega_0 = 1$. The ‘phase diagram’ is divided into four parts distinguished by different colors. The acronyms are explained in the text. Panels (b) and (c): The first derivative of level density as a function of excitation energy for fixed $\lambda = 1$ and $\lambda = 2.5$ respectively. The dashed blue line is computed by Gaussian smoothing of the real spectrum with $N = 40$ (the values of smoothing parameters are $\sigma = 0.04$ in panel b and $\sigma = 0.07$ in panel c). Panels (d)–(f): The evolution of $h_{cl}(\theta, \phi)$ on the Bloch sphere with parameter λ (depicted as a two-dimensional projection). Panel (d) corresponds to $\lambda = 0$, (e) to $\lambda = 1.43$, (f) to $\lambda = 2$.

Critical borderlines

In Fig. 2.1(a) we show a schematic ‘phase diagram’ in the plane $\lambda \times E$ of an EDM with $\delta = 0.3$ [1]. The energetically allowed area is then divided by multiple ESQPT critical borderlines into four ‘quantum phases’ which are denoted S for Saturated phase, N for Normal phase, TC for Tavis-Cummings phase and D for Dicke phase.

In panels (b) and (c) the behavior of the first derivative of level density as a function of the excitation energy is shown for two different fixed values of λ . There are logarithmic divergences as well as jumps marking the critical energies of the ESQPTs.

In panels (d)–(f) the function h_{cl} is plotted for three values of λ . The Bloch sphere is projected onto the plane with variables $(\theta \cos \phi, \theta \sin \phi)$ where we used $j_z = -j \cos \theta$. We observe that with increasing λ the minimum deviates from the south pole ($\theta = 0$) to the equator in the ‘horizontal direction’. A detailed look discloses that the original minimum becomes a saddle point at $\lambda = \lambda_c$ and for even stronger coupling it changes to the local maximum while two new saddle points start to deviate in the ‘vertical direction’.

We can analytically express the evolution of the critical borderlines related to different ESQPTs. The one of the type $(f, r) = (2, 1)$ (saddle point) connected with the QPT at $\lambda = \lambda_c$ at the energy $E/(\omega_0 j) = -1$ evolves as

$$\frac{E_{cl}}{\omega_0 j} = \begin{cases} -1 & \text{for } \lambda \in [\lambda_c, \lambda_0), \\ -\frac{1}{2} \left(\frac{\lambda_0^2}{\lambda^2} + \frac{\lambda^2}{\lambda_0^2} \right) & \text{for } \lambda \in [\lambda_0, \infty), \end{cases} \quad (2.21)$$

where we have defined another special value of the coupling

$$\lambda_0(\delta) = \frac{\sqrt{\omega \omega_0}}{1 - \delta}. \quad (2.22)$$

There are also ESQPTs of the type $(f, r) = (2, 2)$ giving rise to a jump discontinuity in the first derivative of $\rho(E)$. Their borderlines are

$$\frac{E_{c2}}{\omega_0 j} = -1 \quad \text{for } \lambda \in [\lambda_0, \infty), \quad (2.23)$$

$$\frac{E_{c3}}{\omega_0 j} = +1 \quad \text{for } \lambda \in [0, \infty). \quad (2.24)$$

For details see Appendix [D](#).

2.5.4 Quantum phases

A natural question is whether there exist suitable order parameters to distinguish individual phases in the plane $\lambda \times E$. In contrast to QPTs, simple order parameter which would be zero in one phase and abruptly become non-zero when crossing an ESQPT cannot be generally found. However, different phases show qualitatively different energy dependence of smoothed observables (see Ref. [\[1\]](#)).

Different quantum phases can also be distinguished by different averaged slopes of the energy levels in the $\lambda \times E$ plane. Feynman-Hellmann theorem $dE_i/d\lambda = \langle dH/d\lambda \rangle_i$ connects the slope of i -th energy level and the expectation value of the full Hamiltonian differentiated according to λ in the respective eigenstates. In our case $H = H_0 + \lambda V$ where H_0 is the non-interacting part of the Hamiltonian and V is the interaction, we can write

$$\frac{dE_i}{d\lambda} = \langle V \rangle = \frac{E_i - \omega_0 \langle J_z \rangle_i - \omega \langle n \rangle_i}{\lambda}. \quad (2.25)$$

In Fig. [2.2](#) we present the average slope of the levels computed according to [\(2.25\)](#). The piecewise fits show that the average slope of the levels changes from one phase to another.

The reason for calling the phases D, TC, N and S is related to the fact that the smoothed observables follow specific trends. For instance in the D phase this trend is very similar to that of superradiant states (below the ESQPT energy) in a standard Dicke model with $\delta = 1$, similarly for the TC phase. For a detailed explanation see Ref. [\[1\]](#).

2.6 Critical subspace of Tavis-Cummings model

Within a single- M subspace where $M = 2j$ a QPT and an ESQPT can be found, however this time in the effectively $f = 1$ system. In Fig. [2.3](#), panel (a) the evolution of energy levels in the plane $\lambda \times E$ is depicted. In panel (b) the level density (not the energy derivative this time) for fixed $\lambda = 1.5$ is plotted as a function of energy. We observe a logarithmic divergence at $E/(\omega_0 j) = 1$ as a signature of an ESQPT. Similarly, in panel (c) we show that at the same energy the observable corresponding to mean excitation $\langle J_z \rangle$ forms a cusp. This dependence also motivated calling the phase below the ESQPT as A atomic (along with the growing excitation energy the number of excitations in the atomic ensemble grows) and the phase above as F field (the number of photons grows with excitation energy) [\[2\]](#).

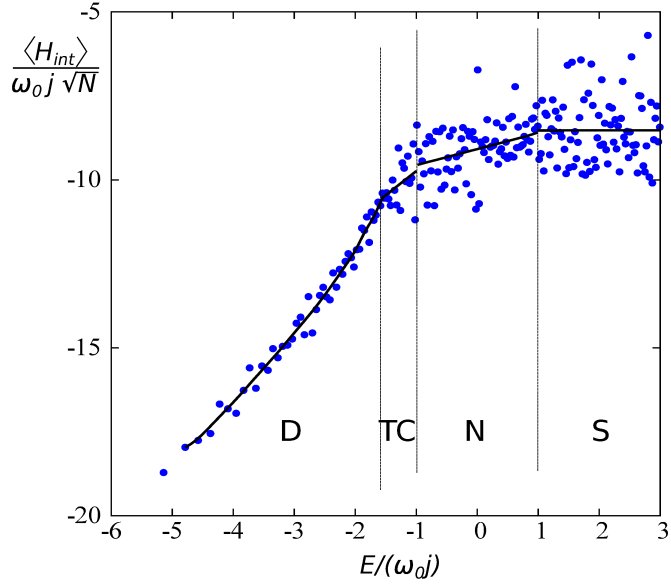


Figure 2.2: Average slopes of the bunches of neighboring 20 levels for the $j = N/2$ Hamiltonian (2.1) with $N = 40$, $\omega = \omega_0 = 1$ and $\delta = 0.3$ at $\lambda = 2.5$. Quantum phases D, TC, N and S are distinguished by different smoothed energy dependences of the average slopes—see the piecewise fits indicated by full black lines. Figure taken from Ref. [1].

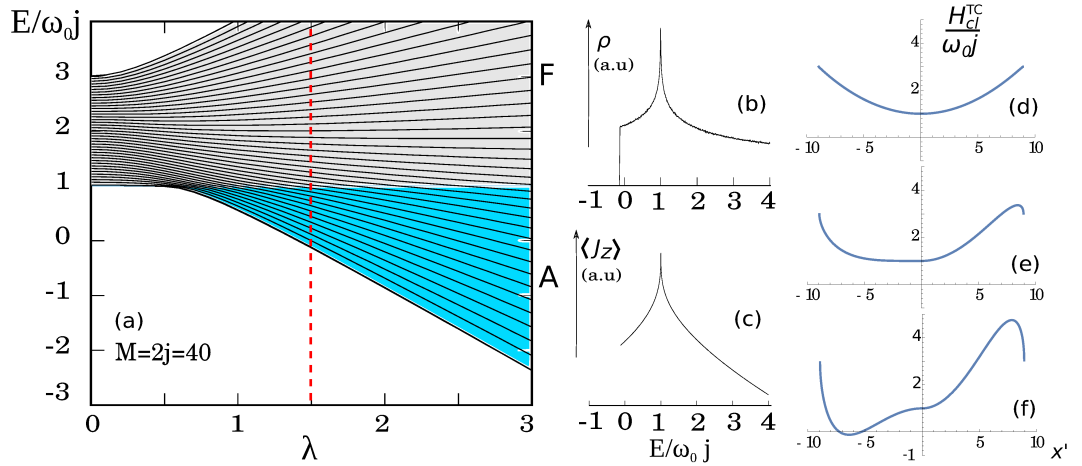


Figure 2.3: Panel (a): The evolution of energy levels with parameter λ of within the critical subspace $M = 2j = 40$ of the integrable $\delta = 0$ EDM. The frequencies are detuned $\omega_0 = \omega/2 = 1$. The ‘phase diagram’ is divided into two parts distinguished by different colors. The acronyms are explained in the text. Panel (b): The level density as a function of excitation energy for fixed $\lambda = 1.5$. Panel (c): The average value of J_z as a function of excitation energy for fixed $\lambda = 1.5$ (computed for $j = 2000$). Panels (d)-(f): The evolution of $H_{cl}^{TC}(x', p' \equiv 0)$ on the Bloch sphere with parameter λ . Panel (d) corresponds to $\lambda = 0$, (e) to $\lambda = 0.5$, (f) to $\lambda = 2.5$.

The nature of the ESQPT can be revealed from the respective classical Hamiltonian $H_{\text{cl}}^{\text{TC}}$ from (2.12). The minimum of the Hamiltonian is always obtained for $p' = 0$, we therefore focus on the evolution of the function $H_{\text{cl}}^{\text{TC}}(x', p' \equiv 0)$ with the control parameter λ , see panels (d)–(f). We observe that the original minimum becomes a stationary point for certain critical value of coupling. Supposing the detuning hierarchy¹ $\omega > \omega_0$, the critical coupling reads as

$$\bar{\lambda}_c = \frac{\omega - \omega_0}{2}. \quad (2.26)$$

The ESQPT energy borderline then reads as

$$\frac{E_{c4}}{\omega_0 j} = +1 \quad \text{for } \lambda \in [\bar{\lambda}_c, \infty). \quad (2.27)$$

The evolution of the lowest state in the critical subspace can be expressed as follows (see Appendix D)

$$\frac{E_{\text{l.s.}}}{\omega_0 j} = \begin{cases} +1 & \lambda \leq \bar{\lambda}_c, \\ +1 - \frac{4}{\omega_0} g(\lambda) \left[\lambda \sqrt{1 - g(\lambda)} - \bar{\lambda}_c \right] & \lambda > \bar{\lambda}_c, \end{cases} \quad (2.28)$$

$$g(\lambda) = \frac{2}{3} - \frac{2}{9} \left(\frac{\bar{\lambda}_c}{\lambda} \right)^2 - \frac{2}{9} \frac{\bar{\lambda}_c}{\lambda} \sqrt{\left(\frac{\bar{\lambda}_c}{\lambda} \right)^2 + 3}.$$

2.7 Experimental relevance

Even though we use the EDM as a purely theoretical ‘playground’ well equipped to study ESQPTs and related phenomena, a natural question comes to one’s mind about its experimental relevance. The progress in manipulation of cold atoms in optical cavities apparently opens new possibilities of simulations of various complex quantum systems. A tremendous success was achieved [50, 51] by realizing the Dicke-like superradiant QPT which had been shown to be unrealistic in the original simple atom-field setting due to neglecting the diabatic term $\propto (b + b^\dagger)^2$ in the Hamiltonian [52]. The relevant commentary on adaptation of the current experimental setup into more general EDM can be found in [53]. A recent experimental paper [54] shows the real measurements on the system with tunable counter-rotating terms in the EDM.

¹The inverse hierarchy $\omega < \omega_0$ can be mapped onto the system with $\omega > \omega_0$, see Ref. [2].

ESQPT-related effects in EDM

3.1 Monodromy

3.1.1 Energy-momentum map of Tavis-Cummings model

We have briefly mentioned quantum monodromy at the end of Chapter 1 as an equivalent concept to the ESQPT, used in molecular spectroscopy. However, the equivalence is not absolute because unlike ESQPTs, monodromy is well-defined only in integrable systems.

It can be recognized in a so-called energy-momentum map which is, in a broader sense, a lattice plot of two observables in the system's eigenstates plotted against each other (like energy vs. momentum). Such plots are also known as Peres lattices [55]. For an integrable system, the lattice is regular but may show some local defects.

One can search for monodromy in the Tavis-Cummings regime of the EDM as the integral of motion M from (2.8) makes the full system integrable. In Fig. 3.1 we present the energy-momentum map¹ for the Tavis-Cummings ($\delta = 0$) Hamiltonian with $N = 40$ atoms [2, 56].

3.1.2 Monodromy point

With a naked eye one can identify a point defect in the lattice in Fig. 3.1 (monodromy point highlighted by a red dot). It has coordinates $(40, -1)$ and coincides with the critical energy (2.24) and the critical subspace $M = 2j$. The presence of such a defect does not allow us to define a global set of smoothly varying quantum numbers for the entire spectrum (which is often used as a definition of quantum monodromy [27]).

Indeed, the lattice can be indexed by two quantum numbers: M and k which is a principal quantum in any M -subspace defined by Bohr-Sommerfeld quantization rule

$$\oint_{E_k} p dq = kh, \quad (3.1)$$

where we have used the explicit form with the Planck constant h , E_k marks the energy of the k -th state in the M -subspace. If we connect the points with the same low k (for example $k = 1$ and $k = 2$) we obtain smooth curves. However, if we want to connect the points with high k (for example $k = 38$ and $k = 39$), the curves have different

¹The energy axis is slightly modified by observable M in order to obtain more lucid lattice.

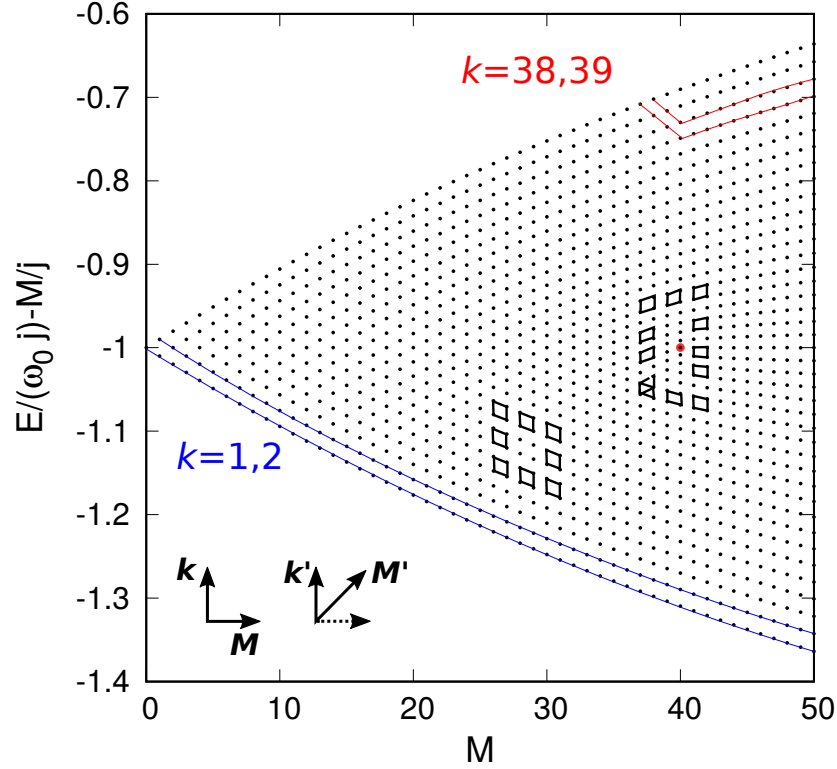


Figure 3.1: The energy-momentum map for the Tavis-Cummings model ($\delta = 0$) with parameters $j = 20$, $\omega = \omega_0 = 1$ and $\lambda = 2.5$. The monodromy point is highlighted by a red dot. The highlighted chains of points correspond to the eigenstates with the same principal quantum number k . Two examples of the transformation of an elementary cell along a closed curve are shown. In the left bottom corner a non-trivial transformation of the initial cell after encircling the monodromy point is sketched.

shapes and have a pike. It means that the quantum number k does not smoothly vary in the lattice.

The same effect is captured when an elementary cell of the lattice is transformed along any closed loop around the monodromy point. One finds that after closing the loop, the original cell is not transformed into itself (that is where the name *monodromy* comes from as it translates as 'once around').

3.1.3 Physical interpretation of quantum monodromy

The states below and above the critical energy have different physical interpretation. For example in the case of the water molecule [28], the energy-momentum map shows a quadratic dependence of energy on the momentum below the critical energy and a linear dependence above. This marks a transition from the bent shape (with rotational type of excitations) to the linear (with vibrational type of excitations). These two dependences correspond to different effective dynamical symmetries governing the two segments of the spectrum [57, 58].

In the Tavis-Cummings model, the symmetry-based interpretation of the monodromy was not yet given. Nevertheless, it is clear that the motion below the critical energy is bound in a limited part of the Bloch sphere which represents the system's phase space. In contrast, the motion above the critical energy explores the whole

sphere, so the corresponding states are unbound in this sense.

3.1.4 Semiclassical viewpoint

In Ref. [2] it is argued that the system's classical dynamics resembles the one of a spherical pendulum (swings on a sphere). Indeed, the evolution of the atomic ensemble is given by a pseudospin trajectory on the Bloch sphere with conserved value M . The point of an unstable equilibrium in the north pole gives rise to the focus-focus type of monodromy (the same as a spherical pendulum shows [59, 60]).

In the Tavis-Cummings model, the *critical* trajectories passing through this unstable equilibrium show a specific time evolution. In the vicinity of the north pole, the motion becomes infinitely slow. For $\lambda > \lambda_c$, the maximal speed is achieved close to the equator and slows down again when it reaches the south pole area. One can compute the photon rate related to these trajectories where an analog of a superradiance in a closed system can be observed. For the fully excited ensemble the rate is small, then forms a peak at maximal intensity when the system is half-deexcited and then becomes slow again. For details see Ref. [2].

3.1.5 Fate of monodromy under non-integrable perturbation

If we now slightly break the integrability with $\delta > 0$ we can observe the decay of monodromy in the Peres lattice². The regular pattern in the lattice starts breaking and one of the most sensitive areas is at the monodromy point. At the classical level, the critical trajectories become chaotic as the first ones even with a very small perturbation. See Ref. [2] for details.

3.2 Bipartite entanglement

3.2.1 Entanglement entropy

A general eigenstate $|\Phi\rangle$ of any composite Hilbert space $\mathcal{H} = \mathcal{H}^l \otimes \mathcal{H}^r$ ('l' for *left*, 'r' for *right*) can be written in a suitable basis as

$$|\Phi\rangle = \sum_{i=1}^d \sqrt{\rho_i} |\phi_i^l\rangle |\phi_i^r\rangle, \quad d = \min(\dim\mathcal{H}^l, \dim\mathcal{H}^r), \quad (3.2)$$

where ρ_i are the common eigenvalues of the reduced density matrices obtained by partial traces over the complementary subspace $\rho^l = \text{Tr}_r|\Phi\rangle\langle\Phi|$ or $\rho^r = \text{Tr}_l|\Phi\rangle\langle\Phi|$. Two subsystems are entangled if the formula (3.2) (called the Schmidt decomposition [61, 62]) contains at least two terms.

It is quantified via *entanglement entropy*

$$S(\rho^r) = S(\rho^l) = - \sum_{i=1}^d \rho_i \log \rho_i \quad (3.3)$$

which takes values between zero (factorized states) to d (maximally entangled states).

²Energy-momentum map like in Fig. 3.1 but M is no more a conserved quantum number, so we consider the average value in the given eigenstate $\langle M \rangle$.

3.2.2 Entanglement of formation

Any statistical mixture on \mathcal{H} can be described by a density matrix

$$\rho = \sum_{j=1}^{\dim \mathcal{H}} p_j \underbrace{|\Phi_j\rangle\langle\Phi_j|}_{\equiv \rho_j} \quad (3.4)$$

where p_j 's are the probabilities of finding the system in the pure states $|\Phi_j\rangle$'s forming an arbitrary (not necessarily orthonormal) basis on \mathcal{H} . In the case of mixed states, the entanglement entropy (3.3) may be non-zero even in the case of the mixture of the pure states. Because the density matrix is not uniquely defined (depends on the selection of the basis states $\{|\Phi_j\rangle\}$), a minimizing over all possible decompositions (3.4) must be employed in the definition of a proper entanglement measure. Indeed, a so-called *entanglement of formation* is defined as [63, 64]

$$E_f(\rho) = \inf \sum_{j=1}^{\dim \mathcal{H}} p_j S(\rho_j). \quad (3.5)$$

3.2.3 Concurrence

Pure states

A direct implementation of formula (3.5) is a computationally difficult task. However, in the case of two qubits we can bypass this problem by defining a new measure of entanglement called *concurrence* [65, 66]. Let $|\phi\rangle$ be an arbitrary pure state of a pair of qubits. Then concurrence $C(\phi)$ is defined as

$$C(\phi) = \left| \langle \phi | \tilde{\phi} \rangle \right|, \quad |\tilde{\phi}\rangle \equiv (\sigma_y \otimes \sigma_y) |\phi^*\rangle, \quad (3.6)$$

where σ_y is the respective Pauli matrix and the star symbol denotes complex conjugation. So it computes the overlap between the state $|\phi\rangle$ and its spin-flipped conjugate state.

For example, a general state³ $|\phi\rangle = \alpha|00\rangle + \beta|01\rangle + \gamma|10\rangle + \delta|11\rangle$ can be factorized only if the coefficients satisfy $\alpha\delta = \beta\gamma$. On the other hand, the maximally entangled states are those with $\alpha = \delta = 0$, $|\beta| = |\gamma|$. The concurrence is expressed as $C(\phi) = 2|\alpha\delta - \beta\gamma|$ and it changes from zero (factorized states) to unity (maximally entangled states).

Mixed states

Nice property of concurrence is that it can be used for mixed states of qubits without a need to minimize some quantity with respect to multiple basis options. Let ϱ be a density matrix of the pair of qubits. We define a spin-flipped complex conjugate matrix $\tilde{\varrho} = (\sigma_y \otimes \sigma_y) \varrho^* (\sigma_y \otimes \sigma_y)$. Let $\{\lambda_1, \lambda_2, \lambda_3, \lambda_4\}$ be a set of the real positive eigenvalues of the matrix $\varrho \tilde{\varrho}$ ordered as $\lambda_1 > \lambda_2 > \lambda_3 > \lambda_4$. Then, concurrence of the given mixture is computed as [65, 66, 67]

$$C(\varrho) = \max\{0, \sqrt{\lambda_1} - \sqrt{\lambda_2} - \sqrt{\lambda_3} - \sqrt{\lambda_4}\}. \quad (3.7)$$

³The state $|0\rangle$ has 1/2 projection and the state $|1\rangle$ has $-1/2$ projection.

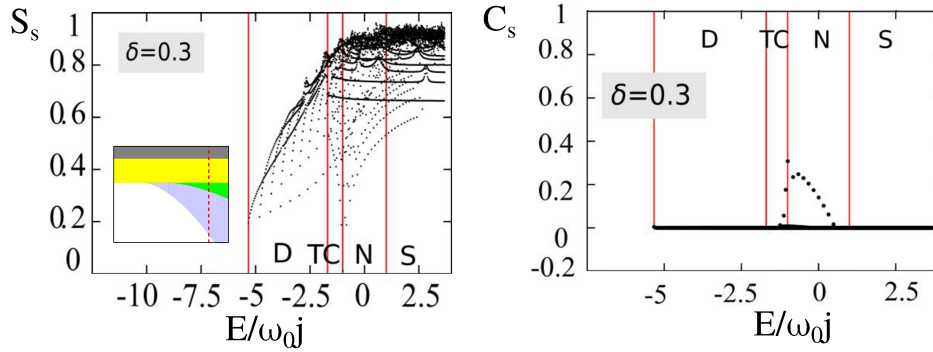


Figure 3.2: Atom-field (left panel) and atom-atom entanglement (right panel) in the excited states of the EDM expressed via scaled entanglement entropy S_s and scaled concurrence C_s , respectively. The parameters are $\delta = 0.3$, $\lambda = 2.5$, $j = 20$, $\omega = \omega_0 = 1$. Red vertical lines mark the ESQPT energies and the respective phases are denoted by their acronyms. The inset in the left panel visualizes the position of the selected excited spectrum for $\lambda = 2.5$ in the phase diagram. Taken from Ref. [1].

It takes the same scale of values as for the pure states, zero means disentangled qubits and unity means maximally entangled qubits. If we apply a density matrix for a pure state in (3.7), it reduces to (3.6). See Appendix E to see how the concurrence is computed in the EDM.

3.2.4 Critical entanglement in a QPT

It is known that entanglement shows a singular growth at a continuous QPT as an analog of a diverging correlation length in continuous classical TPTs [68, 69, 70, 71]. For the Dicke model the computations relating entanglement and the QPT in $j \rightarrow \infty$ limit were performed in Refs. [72, 73]. The entanglement entropy between the atomic and photon subsystems (atom-field entanglement) shows a logarithmic divergence at the critical point. One can also study the entanglement between a pair of atoms (atom-atom entanglement). They are, however, in the mixed state, so the appropriate entanglement measure is the concurrence which shows a cusp maximum at the QPT. For further reading on entanglement in Dicke and related models see Refs. [74, 75, 76].

3.2.5 Entanglement in excited states of EDM

In Ref. [1] the behavior of entanglement in the EDM with intermediate $\delta \in (0, 1)$ across the excited spectrum is thoroughly studied. For the ground-state QPT the same singular behavior can be observed for the atom-field and atom-atom entanglement as in the standard Dicke model. As shown in Chapter 2, multiple ESQPTs appear in the spectrum and an interesting question is whether they affect entanglement in some way. The answer is, however, not unique.

In Fig. 3.2 we show an example of numerically computed entanglement entropy and concurrence in the excited states of the EDM with fixed $\lambda = 2.5$. The values are properly scaled $S_s = S / \ln(N + 1)$, $C_s = C(N - 1)$ to guarantee their range is within the interval $[0, 1]$ with 0 corresponding to disentangled states and 1 to fully entangled ones, see Ref. [1]. One can observe that the ESQPT between TC and N phases gives rise

to certain anomalies in the plots. Indeed, there is a group of states around this critical energy $E_c/\omega_0 j = -1$ with very low atom-field entanglement (left panel). These are also the only states with a non-zero atom-atom entanglement (right panel). The effect of other ESQPTs is not observed.

The key observation is that the state $|\psi_c\rangle$ closest to this ESQPT has extremely high overlap with the unperturbed $\lambda = 0$ ground state $|\langle\psi_c|m = -j, n = 0\rangle|^2 \approx 0.96$. In other words, this state is nearly perfectly localized in the unperturbed basis consisting of the fully separable states which is the reason why atom-field entanglement falls to zero. On the other hand, the growth of concurrence in the state $|\psi_c\rangle$ is rather surprising because the unperturbed eigenstate $| -j, 0\rangle$ alone would give $C_s = 0$ (indeed, all spins are aligned downward independently on one another). So it means that the 4% impurity in $|\psi_c\rangle$ causes significant atom-atom correlations. Moreover, these correlations are the strongest among all other excited states in which the atom-field entanglement is significantly higher.

3.2.6 Participation ratio

In order to quantify the degree of localization of the state $|\psi\rangle$ in the basis $|\phi_l\rangle$, a so-called participation ratio \mathcal{N} is used

$$\mathcal{N} = \frac{1}{\sum_{l=1}^d |\langle\psi|\phi_l\rangle|^4}, \quad (3.8)$$

where d is the dimension of the basis. Participation ratio can vary between 1 (perfectly localized state) to d (perfectly delocalized state).

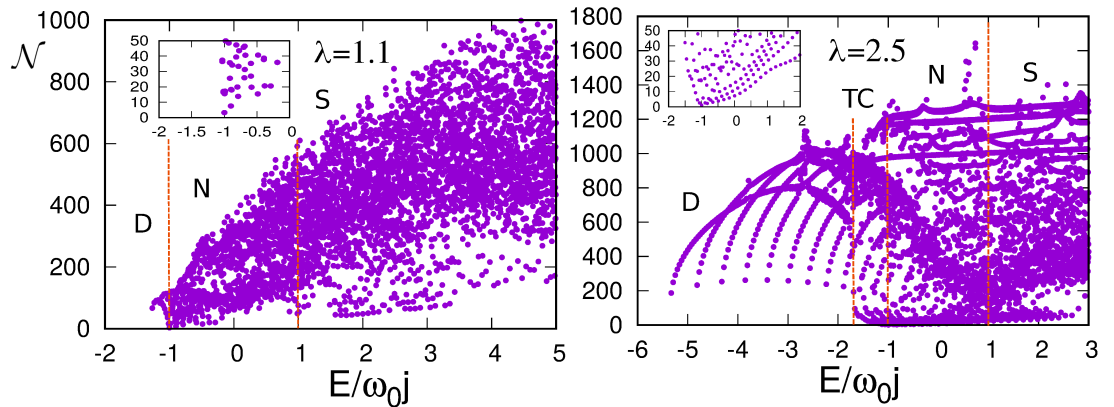


Figure 3.3: Localization of the excited states of the EDM in the unperturbed ($\lambda = 0$) basis expressed via participation ratio \mathcal{N} for two values $\lambda = 1.1$ and $\lambda = 2.5$. The red vertical lines mark the ESQPT energies and the acronyms denote individual phases. Parameters of the model are $j = 20, \omega = \omega_0 = 1$.

In Fig. 3.3 we show the localization of the excited states of the EDM in the unperturbed $|m, n\rangle$ basis for two values of λ . The right panel of the figure corresponds to $\lambda = 2.5$ (parameters are the same as in Fig. 3.2). The inset shows that there is a group of states around the ESQPT of the type $(f, r) = (2, 2)$ at energy $E_c/\omega_0 j = -1$ which are very well localized. The state corresponding to the one with extremely low atom-field entanglement has $\mathcal{N} = 1.09$. In the left panel the case with $\lambda = 1.1$ is depicted. The ESQPT at energy $E_c/\omega_0 j = -1$ divides D and N phases and this time is of the type

$(f, r) = (2, 1)$. The inset shows, that the localization is also very good ($\mathcal{N} = 3.6$), but it can be numerically shown that the atom-field entanglement does not fall to zero in this case (see Ref. [1]). There is another ESQPT of the type $(f, r) = (2, 2)$ at energy $E_c/\omega_0 j = +1$ in the spectrum (the one between N and S phases) where no obvious effect on entanglement was observed in Fig. 3.2.

It demonstrates that the type of the ESQPT generally cannot be the only criterion for the localization (hence the anomaly of entanglement). However, as we have just discussed, the type of the singularity matters (compare the effects of $(f, r) = (2, 2)$ and $(f, r) = (2, 1)$ ESQPTs at $E_c/\omega_0 j = -1$).

3.3 Quantum quench dynamics

3.3.1 Non-adiabatic dynamics and ESQPTs

In this section we focus on some dynamical manifestations of ESQPTs. We prepare the system in an eigenstate $H_i|\psi_i\rangle = E_i|\psi_i\rangle$ where H_i is the EDM Hamiltonian for some initial value of the coupling parameter λ_i . *Quantum quench* is a rapid, highly non-adiabatic change of the Hamiltonian $H_i \rightarrow H_f$ (in our case we consider $\lambda_i \rightarrow \lambda_f$) [77, 78]. So the initial state further evolves with the *new* Hamiltonian as $|\psi_f(t)\rangle = e^{-iH_f t}|\psi_i\rangle$.

Quench dynamics and its relation to the ESQPTs in similar systems has been studied in [79, 80, 81, 82]. In Ref. [3] an attempt to unify the description of the ESQPT-induced effects with respect to various quench protocols was performed within the framework of the EDM.

3.3.2 Survival probability

We can monitor the evolution using the survival probability

$$P(t) = |\langle\psi_i|\psi_f(t)\rangle|^2 = |\langle\psi_i|e^{-iH_f t}|\psi_i\rangle|^2. \quad (3.9)$$

After inserting the basis of the final states $|\phi_{fl}\rangle$ we can write

$$P(t) = \underbrace{\sum_l |s_l|^4}_{\mathcal{N}^{-1}} + 2 \sum_l \sum_{l'(<l)} |s_l|^2 |s_{l'}|^2 \cos[(E_l - E_{l'})t], \quad (3.10)$$

where $s_l \equiv \langle\psi_i|\phi_{fl}\rangle$ and \mathcal{N}^{-1} is the inverse participation ratio, cf. (3.8). From (3.10) one can directly see that for sufficiently long time the survival probability oscillates around the mean value given as \mathcal{N}^{-1} (we call it a saturation regime).

3.3.3 Strength function

The energy distribution of the initial state in the final eigenbasis is called a strength function (or sometimes local density of states)

$$S(E) = \sum_l |s_l|^2 \delta(E - E_{fl}), \quad (3.11)$$

where E_{fl} are the final eigenenergies. It is connected with survival probability via a squared Fourier transform

$$\begin{aligned} P(t) &= \left| \sum_l |s_l|^2 e^{-iE_{fl}t} \right|^2 = \left| \int \sum_l |s_l|^2 e^{-iEt} \delta(E - E_{fl}) dE \right|^2 \\ &= \left| \int e^{-iEt} S(E) dE \right|^2. \end{aligned} \quad (3.12)$$

So in principle, all information on the decay must be encoded in properties of the strength function. In [3] a detailed discussion on which properties of the strength function affect different phases of the decay.

3.3.4 Autocorrelation function

We define the autocorrelation function of the energy distribution $S(E)$

$$\begin{aligned} C(E) &= \int dE' S(E') S(E' + E) = \int \sum_{ll'} |s_l|^2 |s_{l'}|^2 \delta(E' - E_{fl}) \delta(E' + E - E_{f'l'}) dE' \\ &= \sum_{ll'} |s_l|^2 |s_{l'}|^2 \delta(\omega_{ll'} + E), \end{aligned} \quad (3.13)$$

where we have denoted $\omega_{ll'} = E_{fl} - E_{f'l'}$. The survival probability can be expressed as

$$\begin{aligned} P(t) &= \left| \sum_l |s_l|^2 e^{-iE_{fl}t} \right|^2 = \sum_{ll'} |s_l|^2 |s_{l'}|^2 e^{-i\omega_{ll'}t} \\ &= \int e^{+iEt} C(E) dE, \end{aligned} \quad (3.14)$$

so it is linked to the autocorrelation function via a direct Fourier transform.

A valuable insight into the decay can then be obtained by studying the properties of $C(E)$. For example, from the formula (3.14) one can deduce that if the values $|s_l|$ are sharply centered around an energy region where $\omega_{ll'} \ll 1$ the time evolution will be very slow. On the contrary, if the strength function has equally large contributions $|s_l|$ at large energy distances $\omega_{ll'}$ then the decay will be significantly faster.

3.3.5 Quench protocols in the phase diagram

We will provide a few examples of the quenches which are visibly affected by the presence of an ESQPT. The quench protocols will be visualized with arrows in the quantum phase diagram connecting the initial state with the centroid of the strength function in the final eigenbasis.

Let us denote $H_i = H_0 + \lambda_i V$, $H_f = H_0 + \lambda_f V$ where H_0 is the free part of the EDM and V is the interaction. One can combine these expressions as $H_f = H_i + \Delta\lambda V$ with $\Delta\lambda \equiv \lambda_f - \lambda_i$. By taking the average of this equation in the initial state we obtain

$$\langle H_f \rangle_i = E_i + \Delta\lambda \langle V \rangle_i = E_i + \Delta\lambda \frac{dE_i}{d\lambda}(\lambda), \quad (3.15)$$

where the second equality is a consequence of the Feynman-Hellmann theorem. The first term $\langle H_f \rangle_i$ is the mean energy of the initial state after the quench which is, indeed, the centroid of the strength function

$$\begin{aligned}
\int E S(E) dE &= \int E \sum_l |s_l|^2 \delta(E - E_{fl}) dE = \sum_l E_{fl} |s_l|^2 \\
&= \sum_l E_{fl} \langle \psi_i | \phi_{fl} \rangle \langle \phi_{fl} | \psi_i \rangle = \sum_l \langle \psi_i | H_f | \phi_{fl} \rangle \langle \phi_{fl} | \psi_i \rangle \\
&= \langle H_f \rangle_i.
\end{aligned} \tag{3.16}$$

So, according to (3.15) a tangent line to the initial energy level defines the orientation of the arrow and its length is fixed by $\Delta\lambda$.

3.3.6 Quenches from the unperturbed ground state

Stabilization of the initial state

In Fig. 3.4 the survival probability and the strength function after a quantum quench is depicted. The initial state was the ground state of the unperturbed EDM with $\delta = 0.3$ and two different values of λ_f were chosen. The phase diagram inset reveals why values $\lambda_f = 1.1$ and $\lambda_f = 2.5$ were selected. In the first case, the respective strength function is centered at the ESQPT between D and N phases of the type $(f, r) = (2, 1)$ whereas in the other case it is centered at the ESQPT between TC and N phases of the type $(f, r) = (2, 2)$.

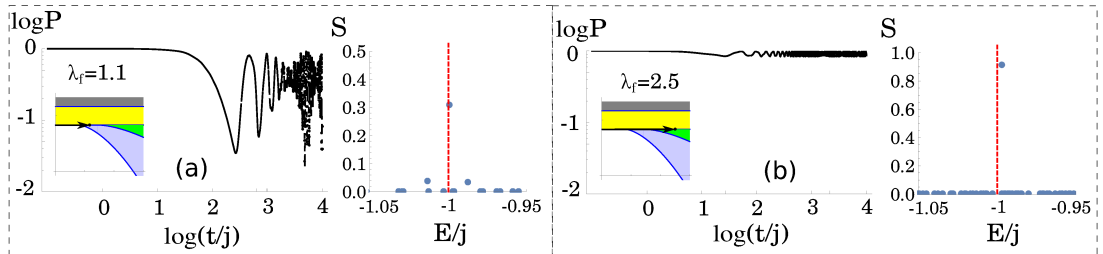


Figure 3.4: A quench of the initial unperturbed $\lambda_i = 0$ ground state within the EDM with $\delta = 0.3$. The survival probability and the respective strength function is plotted (with the ESQPT critical energy marked). The final values of $\lambda_f = 1.1$ and $\lambda_f = 2.5$ are shown. Other parameters of the model are $\omega = \omega_0 = 1$, $j = 20$. Taken from Ref. [3].

In both cases the initial decay is very slow due to the sharp localization of the strength function. However, at a medium time scale the decay is different. For $\lambda_f = 2.5$ the initial state is nearly perfectly stabilized as the survival probability oscillates with a small amplitude around $P \approx 0.85$. This is due to the almost perfect overlap between the initial state and the final eigenstate closest to the ESQPT energy as discussed in Subsec. 3.2.6.

Semiclassical interpretation

From the semiclassical perspective, a quench is represented as a sudden change of the functional $h_{cl}(\phi, j_z)$ from (2.16). The quench protocol from Fig. 3.4 means that the initial state of the classical particle is localized in the global minimum which becomes

a general stationary point after $\lambda_i \rightarrow \lambda_f$. The particle remains at rest until any small perturbation makes it fall from this unstable equilibrium. In a strictly finite system the quantum fluctuations always cause the survival probability to deviate from unity. Figure 3.4, however, demonstrates that different types of stationary points (ESQPTs) may induce different degree of stabilization against the quantum fluctuations at medium and long time scales.

3.3.7 Quenches from the superradiant ground state

Suppression of the $1/t$ modulated decay at medium time scales

Another quench protocol employed takes the superradiant ground state as the initial one and the final value of coupling is chosen as $\lambda_f < \lambda_i$. There exists a critical quench when the strength function is centered at the ESQPT energy.

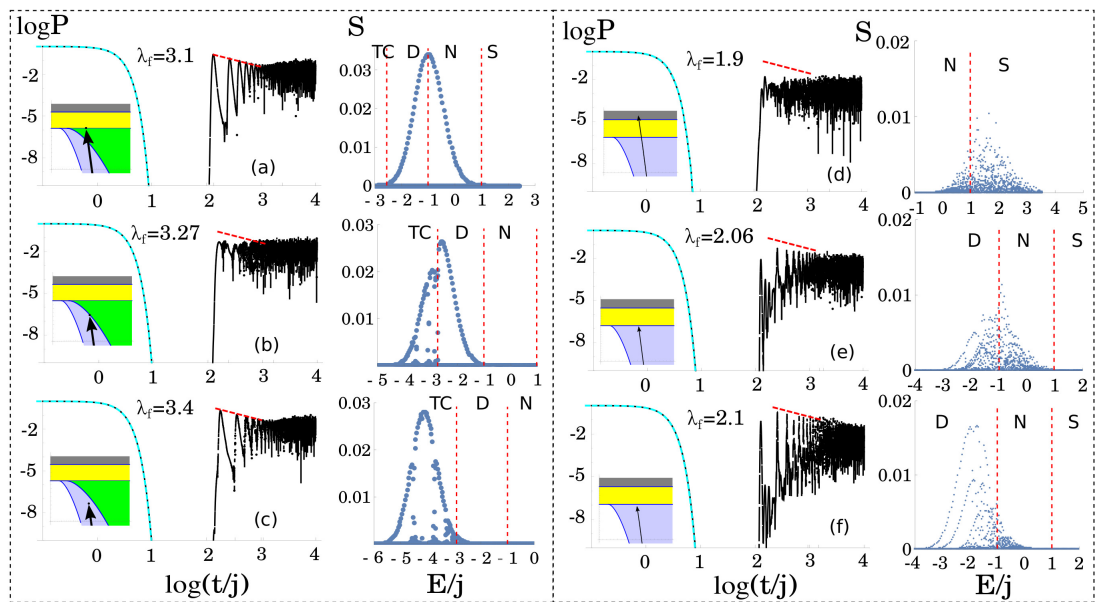


Figure 3.5: A quench of the initial superradiant $\lambda_i > \lambda_c$ ground state within the EDM with $\delta = 0.3$ (panels a–c) and $\delta = 1$ (panels d–f). For $\delta = 0.3$ the initial coupling is $\lambda_i = 6$, for $\delta = 1$ we considered $\lambda_i = 4$. Power-law dependence $\propto 1/t$ is plotted in the survival probability plots as a red dashed line. The survival probability and the respective strength function is plotted (with the ESQPT critical energy marked). The final values of λ_f are written in the individual panels. Other parameters of the model are $\omega = \omega_0 = 1$, $j = 20$. Taken from Ref. [3].

In Fig. 3.5 we show the survival probability and the strength function for several quenches within $\delta = 0.3$ and $\delta = 1$ EDM. For $\delta = 0.3$ we can see that the strength functions have a rather regular pattern and the survival probability shows decaying oscillations at the medium time scale. The oscillations decay as $\propto 1/t$ in panels (a) and (c), however in panel (b) this dependence is suppressed. This is due to the fact that the ESQPT between TC and D phases of the type $(f, r) = (2, 1)$ causes a splitting of the strength function and different energy sampling of it in both quantum phases (see below and Refs. [3, 83, 84] for details).

Obviously, the $(f, r) = (2, 2)$ ESQPT between D and N phases (panel a) has no effect on the strength function. In the $\delta = 0.3$ model the strength functions form a

rather regular Gaussian shape where many of the final eigenstates do not contribute. One can show (for example using Peres lattices as in Ref. [3]) that in such cases mostly the regular final eigenstates contribute to the strength function. As we observe in panels (a)–(c) of Fig. 3.5 the singularity of the full spectrum may not be captured. From the results presented we anticipate that the ESQPT type $(f, r) = (2, 2)$ induces no effect when it is in the semi-regular part of the spectrum, however the type $(f, r) = (2, 1)$ does.

ESQPT-related effects versus chaos

The right panel of Fig. 3.5 depicts the same quench protocol in the $\delta = 1$ mode. This time the $(f, r) = (2, 1)$ ESQPT forms a borderline between D and N phases. The effect of a sudden suppression of the power-law decay of oscillations is not observed. The reason can be anticipated from the complex structure of the respective strength functions (compared to the $\delta = 0.3$ case). One can show that strength function in $\delta = 1$ case lies in a chaotic part of the spectrum whereas in $\delta = 0.3$ case it lies mostly in a regular part. So the effect of an ESQPT competes with chaos in the spectrum.

Numerical experiments: Artificial examples of Gaussian strength functions

For the $\delta = 0.3$ case we observed in Fig. 3.5 the suppression of the power-law modulation in the decay at medium time scales (panel b). As shown in Ref. [83] this $1/t$ modulation comes from two conditions: first, the Gaussian envelope of the strength function, second, its ‘proper’ discrete approximately polynomial sampling as $E_{fl} \approx e_0 + e_1 l + e_2 l^2$ where the coefficients e_0, e_1 satisfy $e_2, |e_2| \ll |e_1|$. It is argued in Ref. [3] that this power-law modulation may be suppressed due to the presence of an ESQPT as the energy sampling may differ in the energy regions on below and above the ESQPT energy.

In Fig. 3.6 we numerically examine the cases of artificially made-up strength function which have the same Gaussian envelope but differ by their discrete structure. In panel (a) we observe the $1/t$ power-law decay is obtained for the quadratic sampling of E_{fl} . If the level density is constant (equidistant sampling in panel b) the revivals do not decay as $1/t$ but rather stay constant at the full⁴ survival $P \approx 1$. On the other hand, if the sampling is inconsistent (panel c) we can observe that the oscillations are not constant neither follow any power-law.

3.3.8 Observables

One can derive how the observables evolve after the quench. For example the average number of photons $\langle n \rangle$ evolves as

$$\begin{aligned} \langle n \rangle &= \langle \psi_i | e^{iH_{\text{f}}t} n e^{-iH_{\text{f}}t} | \psi_i \rangle = \sum_{ll'} \langle \psi_i | \phi_{fl} \rangle e^{iE_{fl}t} \langle \phi_{fl} | n | \phi_{l'l} \rangle e^{-iE_{l'l}t} \langle \phi_{l'l} | \psi_i \rangle \\ &= \sum_{ll'} s_l s_{l'}^* e^{i\omega_{ll'}t} n_{ll'} = \sum_l |s_l|^2 n_{ll} + 2 \sum_{l>l'} \text{Re}[s_l s_{l'}^* e^{i\omega_{ll'}t}] n_{ll'}, \end{aligned} \quad (3.17)$$

⁴In our case, as the strength function was artificially created, the survival probability does not satisfy exactly $P(t=0) = 1$ which, however, does not qualitatively affect the decay.

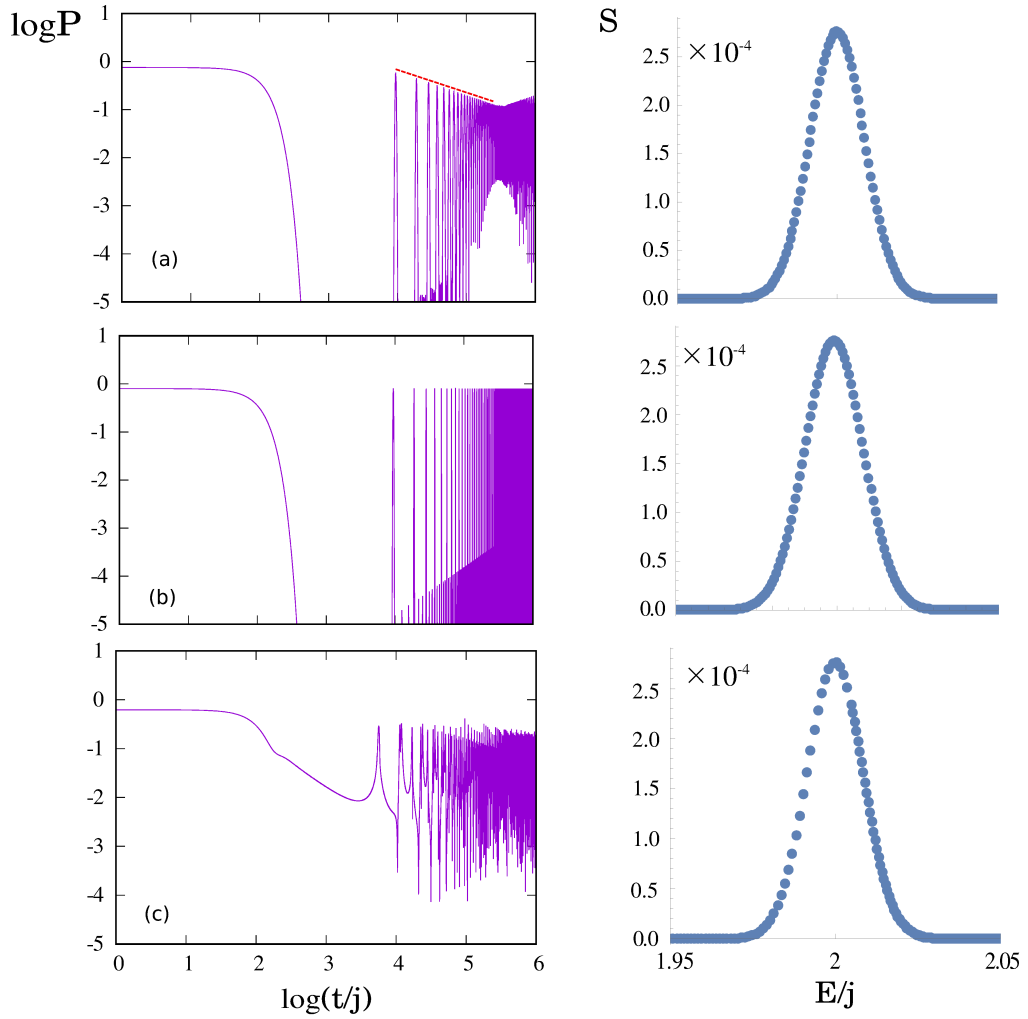


Figure 3.6: A comparison of the decay depending on the discretization of the artificial Gaussian strength function. In panel (a) a quadratic dependence $E_{fl} \approx e_0 + e_1 l + e_2 l^2$ is demonstrated giving rise to $1/t$ decay at medium times (indicated with red dashed line). Panel (b) shows an equidistant sampling of the strength function. Panel (c) depicts the case when the sampling of the strength function changes so it cannot be polynomially approximated.

where we denoted $n_{ll'} \equiv \langle \phi_{fl} | n | \phi_{fl'} \rangle$. It can be shown that the time evolution of the observable consists of qualitatively similar patterns as evolution of the survival probability, again see Ref. [3]. This in principle provides a possibility to detect indirectly the presence of an ESQPT in the spectrum by measuring the time evolution of a certain observable after the quench.

Conclusion

Since the first publications ten years ago, a general theory of ESQPTs has been well established. ESQPTs have been identified in models from various branches of physics. In the thesis, the Extended Dicke model as one of them was thoroughly studied. Here we summarize the main outcomes of our work

- We showed that in order to define ‘quantum phases’ among excited states, one has to investigate the smoothed behavior of the observables as functions of energy. Different quantum phases then have different trends of these dependences which sharply change at the ESQPT critical energies.
- Both atom-field and atom-atom entanglement shows critical behavior in the EDM for the ground-state QPT similarly as in the standard Dicke model ($\delta = 1$ case). Some ESQPTs give rise to an anomalous entanglement in excited states but not a generic rule can be established.
- In the integrable Tavis-Cummings limit ($\delta = 0$) we linked the ESQPT with monodromy in the system. The classical trajectories at the critical energy represent an analog of the Dicke superradiance in a closed system meaning that the photon flux has maximal intensity for half deexcited system of the atoms. We observed that these trajectories become chaotic as the first ones, if one breaks the integrability even with a very small $\delta > 0$.
- The dynamical consequences of the ESQPTs were studied using various quench protocols. We showed that depending on the protocol, the initial state can be either stabilized or, on the contrary, it can decay to the equilibrated regime much faster. Quantum chaos in the final basis can suppress the effects of the ESQPTs on the quench dynamics. Qualitatively similar evolution of the observables after the quench was observed which, in a principle, provides a way to indirect detection of the ESQPTs in the system.

Convergence of the spectrum

In numerical diagonalization of the EDM Hamiltonian (2.1), the Hilbert space of the photons, which is in principle infinite, must be truncated. So it is necessary to check the convergence of the energy levels as the function of maximal photon number N_γ considered in the numerics. In this Appendix we explain how the convergence of the energy levels was tested in our numerical computations.

Suppose we compute the energy spectrum E_l with a certain N_γ and the spectrum E'_l with $N'_\gamma = N_\gamma + \Delta N_\gamma$. We define a quantity measuring the difference in level spacings of the l -th excited state

$$\Delta\varepsilon_l = \left| \frac{\Delta E'_l - \Delta E_l}{\Delta E_l} \right|, \quad \Delta E'_l = E'_l - E_{\text{gs}}, \quad \Delta E_l = E_l - E_{\text{gs}}, \quad (\text{A.1})$$

where E_{gs} is the ground-state energy computed with N_γ . One can define the precision of the convergence by choosing a certain value ε_c . The spectrum is well-converged if $\varepsilon_l < \varepsilon_c$ for all the levels considered.

In Fig. A.1 an example of convergence of the energy levels as a function of N_γ is depicted. We set $\Delta N_\gamma = 10$ which defines the scale of the photon number variations under which we want the spectrum to be invariant. The qualitative dependence is the same for all the levels. After the initial period a sudden drop of $\Delta\varepsilon$ is observed indicating that the energy has converged. Obviously, the lower-lying states converge faster as this drop appears for smaller N_γ . Indeed, in order to get the first excited state converged with precision $\Delta\varepsilon = 10^{-3}$ one needs roughly 50 photons. For the same precision and the ninth excited state one needs more than 70 photons.

A need for the truncation sets the limitation on the numerical studies of excited states of the EDM. In our calculations we were able to work with $j = 20$ and 5000 well-converged energy levels (both parities).

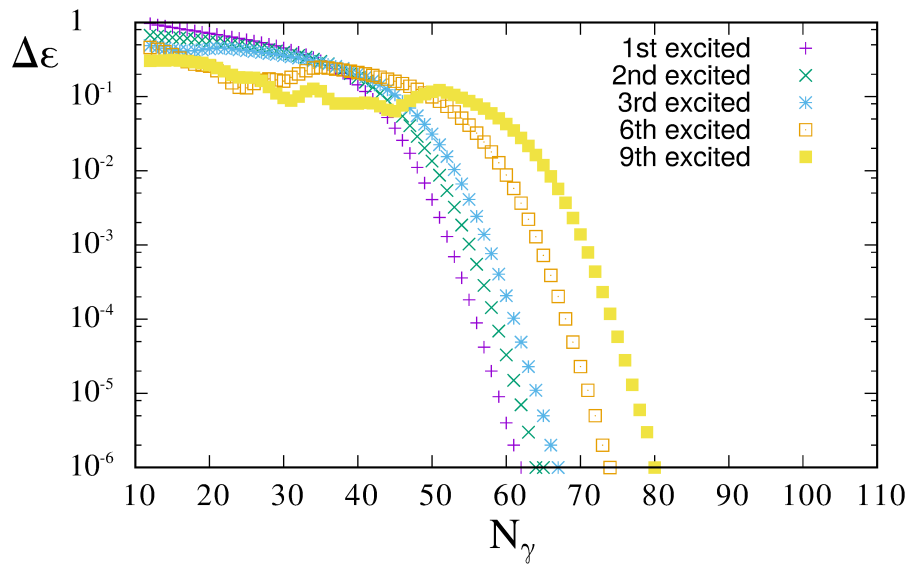


Figure A.1: The convergence of several eigenstates of the EDM. The parameters of the model are $j = 10$, $\lambda = 2.5$, $\omega = \omega_0 = 1$, $\delta = 0.3$, $\Delta N_\gamma = 10$, even parity sector.

Appendix B

Superradiance

B.1 Dynamic superradiance - coherent spontaneous emission

Suppose we have N two-level atoms, all of which are in the excited state. If these atoms form a diluted gas and act as individual radiators, the decay follows the exponential rule $N_{\uparrow}(t) = Ne^{-\frac{t}{\tau}}$ where $N_{\uparrow}(t)$ is the number of excited atoms at time t and τ is a mean lifetime. Intensity of the radiation is simply given as

$$I(t) = -\frac{dN_{\uparrow}(t)}{dt} = \frac{N}{\tau}e^{-\frac{t}{\tau}} \quad (\text{B.1})$$

so the maximal intensity is proportional to N .

On the other hand, if we suppose N coherent radiators in the maximal excited collective state $|j = N/2, m = N/2\rangle$, the time evolution is different. The decay can be monitored using the projection $m(t)$ (equivalent to the number of excited atoms). In the following we consider the large- N limit and quasi-continuous values of m . The decay can be approximated as [39]

$$I(t) = -\frac{dm(t)}{dt} = \frac{1}{\tau} |\langle m-1 | J_- | m \rangle|^2 = \frac{1}{\tau} (j+m(t))(j-m(t)+1). \quad (\text{B.2})$$

Here we directly see that $I \propto N$ for $m \approx j$, $I \propto N^2$ for $m \approx 0$ and again $I \propto N$ for $m \approx -j$.

As most of the time $m(t) \gg 1$ the equation (B.2) can be written as

$$-\frac{dm(t)}{dt} = \frac{1}{\tau} (j^2 - m(t)^2). \quad (\text{B.3})$$

Equation (B.3) can be solved using the ansatz $m = j \tanh \chi$. We obtain

$$-\frac{d\chi}{dt} = \frac{j}{\tau} \rightsquigarrow \chi(t) = \frac{j}{\tau}(t - t_0), \quad (\text{B.4})$$

which can be recast as

$$m(t) = -\frac{N}{2} \tanh \left(\frac{N}{2} \frac{(t - t_0)}{\tau} \right) \quad (\text{B.5})$$

where the integration constant t_0 corresponds to the time of a zero projection $m = 0$ (half deexcited system). The respective intensity reads as

$$I(t) = \frac{N^2}{4\tau} \frac{1}{\cosh^2\left(\frac{N}{2} \frac{(t-t_0)}{\tau}\right)}. \quad (\text{B.6})$$

It forms a sharp peak around $t \approx t_0$ of the maximal intensity $I \propto N^2$.

B.2 Redistribution of decay widths

In Dicke superradiance all the atoms interact via a common radiation field which leads to the non-exponential decay as shown in the previous section. An analogy to this phenomenon has been described in the *continuum shell model* of a weakly bound quantum system (for example nuclei far from the valley of stability). In these systems the coupling between the bound states and the quasi-bound resonant states in the continuum with non-zero widths plays a crucial role in the system's dynamics.

The existence of so-called ‘superradiant states’ can be shown in the following simple model [41]. Suppose a two-level system which, in a suitable basis, is described by the Hamiltonian

$$H = \begin{pmatrix} e_0 - i\gamma & v \\ v^* & e_0 \end{pmatrix}. \quad (\text{B.7})$$

The interaction between the two levels is v , the unperturbed eigenenergies are degenerate e_0 . We now open the system and assume one of the unperturbed levels has a width $\gamma > 0$. Due to the interaction, this decay channel is shared by both eigenstates of (B.7). Indeed, the diagonalization of the Hamiltonian gives the eigenenergies

$$E_{\pm} = e_0 \pm \sqrt{|v|^2 - \frac{\gamma^2}{4}} - i\frac{\gamma}{2}. \quad (\text{B.8})$$

It is interesting to study the evolution of (B.8) with γ . For $\gamma = 0$ the energies are real and the system is closed. By turning on $\gamma > 0$ the energies evolve in the complex plane. Their real parts move towards each other because the square-root term in (B.8) is getting smaller. For ‘critical’ $\gamma = 2|v|$ this term vanishes and the eigenvalues E_{\pm} coalesce. If we consider $\gamma > 2|v|$, the evolution in the complex plane is qualitatively different. The square root gives a pure imaginary number, so the real parts of E_{\pm} remain the same. However, the imaginary part of one solution becomes more stabilized as it moves towards the real axis (long-lived state E_+) whereas the other *superradiant state* deviates further from the real axis (short-lived state E_-). The redistribution of the widths into a short-lived and long-lived states can be naturally generalized to larger systems. The ‘criticality’ can be achieved by the existence of overlapping resonances which form a common decay channel [42].

Nuclear spectroscopic data show the cases where a narrow resonance is in a close vicinity of a wide one. For example in neutron-rich nuclei a small *Pygmy* resonance can be found at the low energy end of the *gigantic dipole resonance*. The formation of such structures is then naturally linked to the mechanism described above.

B.3 Equilibrium superradiance

A TPT to the superradiant phase, where the average number of photons in the ground state is non-zero $\langle n \rangle_{\text{g.s.}} = \langle b^\dagger b \rangle_{\text{g.s.}} > 0$, was described by Hepp and Lieb in the 1970's [37, 38]. We can re-derive the same phase transition for the EDM as well [1].

We consider Glauber coherent states

$$|\alpha\rangle = e^{-\frac{|\alpha|^2}{2}} e^{\alpha b^\dagger} |0\rangle \quad (\text{B.9})$$

where $|0\rangle \equiv |n = 0\rangle$ is the state with no photons. The partition function can be expressed as a function of $\alpha = \alpha' + i\alpha''$

$$Z_\alpha = \text{Tr}_A \langle \alpha | e^{-\beta H} | \alpha \rangle \quad (\text{B.10})$$

where the partial trace is performed over the atomic subspace, β is the inverse temperature and the Hamiltonian H of the EDM (2.1). Parameter α will serve as the order parameter for the phase transition as $\langle n \rangle_\alpha = |\alpha|^2$ so its non-zero absolute value means non-zero photon number in the system.

The EDM Hamiltonian expressed in the coherent states can be written as

$$H_{\alpha\alpha} = \sum_{i=1}^N \frac{\omega_0}{2} \sigma_z^i + \omega |\alpha|^2 + \frac{\lambda}{\sqrt{N}} \sum_{i=1}^N 2\sigma_x^i \alpha' - \frac{\lambda}{\sqrt{N}} (1-\delta) \sum_{i=1}^N (\sigma_+^i \alpha^* + \sigma_- \alpha). \quad (\text{B.11})$$

We can rewrite (B.10) as

$$Z_\alpha = e^{-\beta\omega|\alpha|^2} \prod_{i=1}^N \text{Tr}_A \exp \left(-\beta \underbrace{\left[\frac{\omega_0}{2} \sigma_z^i + \frac{\lambda}{\sqrt{N}} 2\sigma_x^i \alpha' - \frac{\lambda}{\sqrt{N}} (1-\delta) (\sigma_+^i \alpha^* + \sigma_- \alpha) \right]}_{h: 2 \times 2 \text{ matrix}} \right). \quad (\text{B.12})$$

If we use the explicit form of the Pauli matrices, we obtain

$$h = \begin{pmatrix} \frac{\omega_0}{2} & \frac{\lambda}{\sqrt{N}} [2\alpha' - (1-\delta)\alpha^*] \\ \frac{\lambda}{\sqrt{N}} [2\alpha' - (1-\delta)\alpha] & -\frac{\omega}{2} \end{pmatrix}. \quad (\text{B.13})$$

The respective eigenvalues of the matrix (B.13) are

$$E_{\alpha\pm} = \pm \sqrt{\left(\frac{\omega_0}{2}\right)^2 + \frac{\lambda^2}{N} [(1+\delta)^2 \alpha'^2 + (1-\delta)^2 \alpha''^2]} \equiv \pm E_\alpha \quad (\text{B.14})$$

so the partition function can be expressed as

$$Z_\alpha(\beta) = e^{-\beta\omega|\alpha|^2} \left(e^{+\beta E_\alpha} + e^{-\beta E_\alpha} \right). \quad (\text{B.15})$$

The free energy is linked with the partition function as $F_\alpha(\beta) = -\frac{1}{\beta} \ln Z_\alpha(\beta)$ and so we obtain $F_\alpha(\beta) = \omega |\alpha|^2 - \frac{N}{\beta} \ln(e^{+\beta E_\alpha} + e^{-\beta E_\alpha})$. The TPT will be studied as a structural change of the free energy per atom

$$\frac{F_{\tilde{\alpha}}(\beta)}{N} = \omega |\tilde{\alpha}|^2 - \frac{1}{\beta} \ln(2 \cosh(\beta E_{\tilde{\alpha}})) \quad (\text{B.16})$$

where the scaled order parameter $\tilde{\alpha} = \alpha/N$ is introduced and

$$E_{\tilde{\alpha}} = \sqrt{\left(\frac{\omega_0}{2}\right)^2 + \lambda^2[(1+\delta)^2\alpha'^2 + (1-\delta)^2\alpha''^2]}. \quad (\text{B.17})$$

We can now search for the stationary points of the scaled free energy with respect to $\tilde{\alpha}'$ and $\tilde{\alpha}''$

$$\frac{\partial}{\partial \tilde{\alpha}'} \frac{F_{\tilde{\alpha}}}{N} = \tilde{\alpha}' \left(2\omega - \frac{(1+\delta)^2\lambda^2}{E_{\tilde{\alpha}}} \tanh(\beta E_{\tilde{\alpha}}) \right) \equiv 0, \quad (\text{B.18})$$

$$\frac{\partial}{\partial \tilde{\alpha}''} \frac{F_{\tilde{\alpha}}}{N} = \tilde{\alpha}'' \left(2\omega - \frac{(1-\delta)^2\lambda^2}{E_{\tilde{\alpha}}} \tanh(\beta E_{\tilde{\alpha}}) \right) \equiv 0. \quad (\text{B.19})$$

The point $(\tilde{\alpha}', \tilde{\alpha}'') = (0, 0)$ is always stationary and forms a thermal equilibrium for sufficiently high temperature $T = 1/\beta$. This represents the normal ground state as $\langle n \rangle_{\tilde{\alpha}} = 0$.

We define two special values temperatures

$$T_c = \frac{\omega_0}{2} \operatorname{artanh}^{-1} \frac{\lambda_c^2}{\lambda^2}, \text{ for } \lambda > \lambda_c \equiv \frac{\sqrt{\omega\omega_0}}{1+\delta}. \quad (\text{B.20})$$

$$T_0 = \frac{\omega_0}{2} \operatorname{artanh}^{-1} \frac{\lambda_0^2}{\lambda^2}, \text{ for } \lambda > \lambda_0 \equiv \frac{\sqrt{\omega\omega_0}}{1-\delta}. \quad (\text{B.21})$$

If in the allowed region of the coupling strength $T < T_c$, a new superradiant solution of (B.18) appears. This solution corresponds to the new global minimum of the free energy with $\tilde{\alpha} \neq 0$, i.e., $\langle n \rangle_{\tilde{\alpha}} > 0$. The value of $T = T_0$ represents a saddle point of the free energy so crossing this value of temperature is not a real TPT. The effect of the states associated with the saddle points of the free energy was discussed in Ref. [48]. The full thermal phase diagram in the plane $\lambda \times T$ is in Ref. [1].

Polaron transformation

In the ultra-strong limit $\lambda \rightarrow \infty$ the interacting term in the Hamiltonian (2.3) dominates which is equivalent to considering $\omega_0 \rightarrow 0$. Note that the bosonic term $\propto \omega$ cannot be neglected as the number of photons can grow without restraint.

In the first step we rotate the spin variables and obtain a new Hamiltonian $H_1 = U_1 H_D U_1^\dagger$, where $U = e^{i\frac{\pi}{2} J_y}$. By this we transform $J_z \rightarrow -J_x$ and $J_x \rightarrow J_z$. So the Hamiltonian now reads as

$$H_1 = \omega b^\dagger b - \omega_0 J_x + \frac{2\lambda}{\sqrt{N}} J_z (a^\dagger + a). \quad (\text{C.1})$$

Using the well-known relations

$$b = \frac{1}{\sqrt{2}}(x + ip), \quad b^\dagger = \frac{1}{\sqrt{2}}(x - ip), \quad \longrightarrow b + b^\dagger = \sqrt{2} x, \quad b^\dagger - b = -i\sqrt{2} p \quad (\text{C.2})$$

we rewrite the interaction term as $\propto x J_z$. So the Hamiltonian represents a shifted oscillator. Because x and J_z commute, H_1 can be equivalently written as

$$H_1 = -\omega_0 J_x + \frac{\omega}{2} \left(x + \frac{2\sqrt{2}\lambda}{\omega\sqrt{N}} J_z \right)^2 + \frac{\omega}{2} p^2 - \frac{(2\lambda)^2}{\omega N} J_z^2. \quad (\text{C.3})$$

To compensate the shift in x direction we introduce an operator $U_2 = e^{-i\alpha p}$ (as the momentum operator is the generator of translation) with $\alpha = \frac{2\sqrt{2}\lambda}{\omega\sqrt{N}} J_z$. Written in terms of creation and annihilation operators $U_2 = e^{\frac{2\lambda}{\omega\sqrt{N}}(b^\dagger - b)J_z}$. The last two terms in (C.3) remain unchanged because both p and J_z commute with U_2 . However the first term does not.

We can write $J_z = 1/2 (J_+ + J_-)$. Together with a commutation relation $[J_z, J_\pm] = \pm J_\pm$ one can easily prove $J_z^n J_\pm = J_\pm (J_z \pm 1)^n$. Using this, the following chain of equalities is straightforward (we denote $\sigma = \frac{2\lambda}{\omega\sqrt{N}} (b^\dagger - b)$)

$$e^{\sigma J_z} J_\pm e^{-\sigma J_z} = \left(1 + \sigma J_z + \frac{\sigma^2}{2!} J_z^2 + \dots \right) J_\pm e^{-\sigma J_z} = J_\pm e^{\pm\sigma}. \quad (\text{C.4})$$

Therefore the new Hamiltonian $H_2 = U_2 H_1 U_2^\dagger$ takes the form

$$H_2 = -\frac{\omega_0}{2} (J_+ e^\sigma + J_- e^{-\sigma}) + \omega b^\dagger b - \frac{(2\lambda)^2}{\omega N} J_z^2. \quad (\text{C.5})$$

In the ultra-strong limit we neglect the first two terms as $\omega_0 \rightarrow 0$ the Hamiltonian (C.5) decouples bosonic and atomic variables so can be analytically solved.

Stationary points of the classical Hamiltonian

D.1 General $\delta \neq 0$ case

Here we explicitly perform the semiclassical analysis of the EDM. The pairs (x, p) and $(\phi \equiv \tan^{-1}(j_y/j_x), j_z)$ in (2.9) correspond to the classical coordinates and momenta for the bosonic field and the spin system, respectively. The ESQPTs are induced by stationary points so we write down the Hamilton's equations and set them to zero

$$\frac{\partial H_{\text{cl}}}{\partial p} = \frac{\partial x}{\partial t} = \omega p - (1 - \delta) \lambda \sqrt{j} \sqrt{1 - \frac{j_z^2}{j^2}} \sin \phi \equiv 0, \quad (\text{D.1})$$

$$\frac{\partial H_{\text{cl}}}{\partial x} = -\frac{\partial p}{\partial t} = \omega x + (1 + \delta) \lambda \sqrt{j} \sqrt{1 - \frac{j_z^2}{j^2}} \cos \phi \equiv 0, \quad (\text{D.2})$$

$$\frac{\partial H_{\text{cl}}}{\partial j_z} = \frac{\partial \phi}{\partial t} = \omega_0 - \frac{\lambda j_z}{j^{\frac{3}{2}} \sqrt{1 - \frac{j_z^2}{j^2}}} [(1 + \delta) x \cos \phi - (1 - \delta) p \sin \phi] \equiv 0, \quad (\text{D.3})$$

$$\frac{\partial H_{\text{cl}}}{\partial \phi} = -\frac{\partial j_z}{\partial t} = -\lambda \sqrt{j} \sqrt{1 - \frac{j_z^2}{j^2}} [(1 + \delta) x \sin \phi + (1 - \delta) p \cos \phi] \equiv 0. \quad (\text{D.4})$$

We substitute (D.1) and (D.2) into (D.3) and (D.4). The two resulting equations are

$$\omega_0 = \frac{\lambda j_z}{j^{\frac{3}{2}} \sqrt{1 - \frac{j_z^2}{j^2}}} \left[(1 + \delta) x \cos \phi - (1 - \delta)^2 \lambda \sqrt{j} \sqrt{1 - \frac{j_z^2}{j^2}} \sin^2 \phi \frac{1}{\omega} \right], \quad (\text{D.5})$$

$$0 = \left(\lambda \sqrt{j} \sqrt{1 - \frac{j_z^2}{j^2}} \right) \sin \phi \left[(1 + \delta) x + (1 - \delta)^2 \lambda \sqrt{j} \sqrt{1 - \frac{j_z^2}{j^2}} \frac{1}{\omega} \cos \phi \right]. \quad (\text{D.6})$$

From the three terms in multiplication in (D.6) we find three solutions of the stationary points.

1. $\lambda \sqrt{j} \sqrt{1 - \frac{j_z^2}{j^2}} = 0.$

This condition leads to the 'trivial' solution valid for any coupling and for any δ .

$$(x_s, p_s) = (0, 0), \quad (j_{zs}, \cos \phi_s) = (\pm j, \cos \phi) \quad (\text{D.7})$$

2. $\sin \phi = 0$.

This condition leads to the solution

$$\begin{aligned} (x_s, p_s) &= \mp \left((1 + \delta) \frac{\lambda \sqrt{j}}{\omega} \sqrt{1 - \left(\frac{\lambda_c}{\lambda}\right)^4}, 0 \right) \\ (j_{zs}, \cos \phi_s) &= \left(-j \left(\frac{\lambda_c}{\lambda}\right)^2, \pm 1 \right), \quad \text{with } \lambda_c = \frac{\sqrt{\omega_0 \omega}}{1 + \delta} \end{aligned} \quad (\text{D.8})$$

This solutions exists only for $\lambda > \lambda_c$.

3. $(1 + \delta)x + (1 - \delta)^2 \lambda \sqrt{j} \sqrt{1 - \frac{j_z^2}{j^2} \frac{1}{\omega}} \cos \phi = 0$.

Using (D.5) we get

$$\omega_0 = -\frac{\lambda^2 j_z (1 - \delta)^2}{j \omega} (\sin^2 \phi + \cos^2 \phi) = -\frac{\lambda^2 j_z (1 - \delta)^2}{j \omega}. \quad (\text{D.9})$$

So now for $\delta \neq 1$ we get

$$j_{zs} = -j \left(\frac{\lambda_0}{\lambda}\right)^2, \quad \text{with } \lambda_0 = \frac{\sqrt{\omega_0 \omega}}{1 - \delta} \quad (\text{D.10})$$

It is easy to complete the full solution.

$$\begin{aligned} (x_s, p_s) &= \frac{\lambda \sqrt{j}}{\omega} \sqrt{1 - \left(\frac{\lambda_0}{\lambda}\right)^4} \left(-(1 + \delta) \cos \phi, (1 - \delta) \sin \phi \right), \\ (j_{zs}, \cos \phi_s) &= \left(-j \left(\frac{\lambda_0}{\lambda}\right)^2, \cos \phi \right). \end{aligned} \quad (\text{D.11})$$

This solution exists for $\lambda > \lambda_0$.

The ground state evolution (2.14) is obtained by inserting (D.7) and (D.8) back into the Hamiltonian (2.9). Similarly, Eq. (2.21) is obtained from (D.11).

D.2 Critical M -subspace of the $\delta = 0$ model

Here we consider the Hamiltonian (2.12) for the critical subspace $M = 2j$. We suppose a detuning $\omega \geq \omega_0$ and denote $\Delta\omega \equiv \omega - \omega_0$. So the classical Hamiltonian reads as

$$H_{\text{cl}}^{\text{TC}}(x', p') = \frac{\Delta\omega}{2}(x'^2 + p'^2) + \omega_0 j + \lambda x' |x'^2 + p'^2| \sqrt{1 - \frac{x'^2 + p'^2}{4j}}. \quad (\text{D.12})$$

The stationary point related to the ground state corresponds to $p' = 0$ (one can check that $\frac{dx'}{dt} = \frac{\partial H_{\text{cl}}^{\text{TC}}}{\partial p'}$ gives zero then). We therefore investigate structural changes of a one-dimensional potential with λ .

In order to find the alternating minimum for some $\lambda > 0$, the interacting term in (D.12) must be added with the negative sign. So we will restrict the analysis on the

negative range $x' \in [-2\sqrt{j}, 0]$ where $|x'| = -x'$. We substitute $x' = 2\sqrt{j} \sin \xi$ where we consider $\xi \in [-\pi/2, 0]$. With this parametrization the potential takes form

$$H_{\text{cl}}^{\text{TC}}(\xi, p' = 0) = \omega_0 j + 2j \sin^2 \xi (\Delta\omega - 2\lambda \cos \xi). \quad (\text{D.13})$$

We perform the first derivative

$$\frac{dH_{\text{cl}}^{\text{TC}}}{d\xi} = 4j \sin \xi (\Delta\omega \cos \xi - 2\lambda \cos^2 \xi + \lambda \sin^2 \xi). \quad (\text{D.14})$$

The original minimum for $\lambda = 0$ is $\xi = 0$ (so $x' = 0$). We can check that it changes to local maximum (from the left as we deal with $x' \leq 0$ only) by taking the second derivative in $\xi = 0$

$$\frac{d^2 H_{\text{cl}}^{\text{TC}}}{d\xi^2}(\xi < 0) = 4j \cos \xi (\Delta\omega \cos \xi - 2\lambda \cos^2 \xi) + \text{terms including } \sin \xi. \quad (\text{D.15})$$

Obviously, the sign of the second derivative is given as $\text{sgn}(\Delta\omega - 2\lambda)$. If we increase coupling so that it reaches the critical value $\bar{\lambda} = \Delta\omega/2$, the original minimum becomes a maximum.

It is interesting to have a look at the behavior of the second derivative in this point for $x' > 0$ ($\xi > 0$). We obtain

$$\frac{d^2 H_{\text{cl}}^{\text{TC}}}{d\xi^2}(\xi > 0) = 4j \cos \xi (\Delta\omega \cos \xi + 2\lambda \cos^2 \xi) + \text{terms including } \sin \xi. \quad (\text{D.16})$$

So from the right, the second derivative remains positive for any λ . So after the QPT takes place for $\lambda = \bar{\lambda}_c$, the original minimum becomes a sort of an ‘inflection point’ (maximum from the left, minimum from the right). However, the Hamiltonian is non-analytic in this point as in the vicinity of $x' = 0$ it can be quadratically approximated as $\propto \text{sgn} x' x'^2$.

Even though this stationary point does not fully satisfy the conditions for the classification from Ref. [24] (due to the non-analyticity), the quadratic minimum from the left side gives rise to the logarithmic divergence in level density, see 2.3(b). So we can classify this ESQPT as *quasi* $(f, r) = (1, 1)$ type.

Let us now derive the formula for evolution of the ground state for $\lambda > \bar{\lambda}_c$. So from (D.14) we obtain the condition

$$(\Delta\omega \cos \xi - 2\lambda \cos^2 \xi + \lambda \sin^2 \xi) = 0. \quad (\text{D.17})$$

There are two possible solutions

$$\cos \xi_{\pm} = \frac{\bar{\lambda}_c}{3\lambda} \left(1 \pm \sqrt{1 + 3 \frac{\lambda^2}{\bar{\lambda}_c^2}} \right). \quad (\text{D.18})$$

As we are restricted onto the interval where cosine takes values between 0 and 1, the solution with the minus sign can be disregarded. The other solution is obviously valid only for $\lambda > \bar{\lambda}_c$. If it is inserted into (D.13) one obtains the analytic formula (2.28).

Computation of *concurrence* in EDM

A general density matrix of two qubits from a *multi*-qubit state ϱ_{12} symmetric under the exchange these two qubits can be written as [67].

$$\varrho_{12} = \begin{pmatrix} v_+ & x_+^* & x_+^* & u^* \\ x_+ & w & y^* & x_-^* \\ x_+ & y^* & w & x_-^* \\ u & x_- & x_- & v_- \end{pmatrix}. \quad (\text{E.1})$$

The constituents of the matrix can be expressed via Pauli matrices of the two qubits as

$$v_{\pm} = \frac{1}{4}(1 \pm 2\langle\sigma_{1z}\rangle + \langle\sigma_{1z}\sigma_{2z}\rangle), \quad (\text{E.2})$$

$$x_{\pm} = \frac{1}{2}(\langle\sigma_{1+}\rangle \pm \langle\sigma_{1+}\sigma_{2z}\rangle), \quad (\text{E.3})$$

$$w = \frac{1}{4}(1 - \langle\sigma_{1z}\sigma_{2z}\rangle), \quad (\text{E.4})$$

$$y = \langle\sigma_{1+}\sigma_{2-}\rangle, \quad (\text{E.5})$$

$$u = \frac{1}{4}(\langle\sigma_{1x}\sigma_{2x}\rangle - \langle\sigma_{1y}\sigma_{2y}\rangle + 2i\langle\sigma_{1x}\sigma_{2y}\rangle). \quad (\text{E.6})$$

As an example we show how (E.2) can be derived. In the basis $\{|00\rangle, |01\rangle, |10\rangle, |11\rangle\}$ one can express $\sigma_{1z} \equiv \sigma_z \otimes \mathbb{I} = \text{diag}(1, 1, -1, -1)$. So we can write

$$\langle\sigma_{1z}\rangle = \text{Tr}(\varrho_{12}\sigma_{1z}) = v_+ + w - w - v_- = v_+ - v_-. \quad (\text{E.7})$$

Similarly $\sigma_{1z}\sigma_{2z} = \text{diag}(1, -1, -1, 1)$, so

$$\langle\sigma_{1z}\sigma_{2z}\rangle = \text{Tr}(\varrho_{12}\sigma_{1z}\sigma_{2z}) = v_+ - 2w + v_-. \quad (\text{E.8})$$

Together with the condition $\text{Tr}(\varrho_{12}) = 1 = v_+ + 2w + v_-$ we can write

$$1 \pm 2\langle\sigma_{1z}\rangle + \langle\sigma_{1z}\sigma_{2z}\rangle = v_+ + 2w + v_- \pm 2v_+ \mp 2v_- + v_+ - 2w + v_- = 4v_{\pm} \quad (\text{E.9})$$

which is equivalent to (E.2).

As the pair of qubits is selected from a totally symmetric state $|j, m\rangle$ with respect to the exchange of any two qubits we can express the density matrix (E.1) using the expectation values of the global operators. Indeed, the global operators can be written

as $J_\circ = \sum_i \frac{1}{2} \sigma_\circ^i$ where $i = 1, 2, \dots, N = 2j$ indexes the spin sites (atoms) and the symbol \circ stands for $\{+, -, z\}$ or $\{x, y, z\}$. The following identities hold

$$\langle \sigma_{1\alpha} \rangle = \frac{2\langle J_\alpha \rangle}{N}, \quad \alpha = \{x, y, z\}, \quad (\text{E.10})$$

$$\langle \sigma_{1+} \rangle = \frac{\langle J_+ \rangle}{N}, \quad (\text{E.11})$$

$$\langle \sigma_{1\alpha} \sigma_{2\alpha} \rangle = \frac{4\langle J_\alpha^2 \rangle - N}{N(N-1)}, \quad (\text{E.12})$$

$$\langle \sigma_{1x} \sigma_{2y} \rangle = 2\langle \{J_x, J_y\} \rangle \quad (\text{E.13})$$

$$\langle \sigma_{1+} \sigma_{2z} \rangle = \frac{\langle \{J_+, J_z\} \rangle}{N(N-1)}, \quad (\text{E.14})$$

where $\{\circ, \circ\}$ in (E.13) and (E.14) is the anticommutator of two operators. The equalities (E.10) and (E.11) are straightforward as the mean value of a *single*-qubit operator is the same for all qubits. For example

$$\langle J_\alpha \rangle = \frac{1}{2} \sum_{i=1}^N \langle \sigma_{i\alpha} \rangle = \frac{N\langle \sigma_{1\alpha} \rangle}{2}, \quad \langle J_+ \rangle = \sum_{i=1}^N \langle \sigma_{i+} \rangle = N\langle \sigma_{1+} \rangle. \quad (\text{E.15})$$

The equality (E.12) can be obtained as follows

$$\begin{aligned} \langle J_\alpha^2 \rangle &= \left\langle \frac{1}{4} \sum_{i=1}^N \sigma_{i\alpha} \sum_{j=1}^N \sigma_{j\alpha} \right\rangle = \frac{1}{4} \left(\sum_{i=1}^N \langle \sigma_{i\alpha}^2 \rangle + \sum_{i \neq j}^N \langle \sigma_{i\alpha} \sigma_{j\alpha} \rangle \right) \\ &= \frac{1}{4} \left(N \underbrace{\langle \sigma_{1\alpha}^2 \rangle}_{=1} + N(N-1) \langle \sigma_{1\alpha} \sigma_{2\alpha} \rangle \right). \end{aligned} \quad (\text{E.16})$$

In a similar way (E.13) and (E.14) can be derived.

So the density matrix elements can be expressed as

$$v_\pm = \frac{N^2 - 2N + 4\langle J_z^2 \rangle \pm 4\langle J_z \rangle(N-1)}{4N(N-1)}, \quad (\text{E.17})$$

$$x_\pm = \frac{(N-1)\langle J_+ \rangle \pm \langle \{J_+, J_z\} \rangle}{2N(N-1)}, \quad (\text{E.18})$$

$$w = \frac{N^2 - 4\langle J_z^2 \rangle}{4N(N-1)}, \quad (\text{E.19})$$

$$y = \frac{2\langle J_x^2 + J_y^2 \rangle - N}{2N(N-1)}, \quad (\text{E.20})$$

$$u = \frac{\langle J_+^2 \rangle}{N(N-1)}. \quad (\text{E.21})$$

Moreover, if we consider only parity-symmetric states then $\langle J_+ \rangle = 0$ and so $x_\pm = 0$. This means that one is able to form the matrix (E.1) in the EDM by means of the expectations values of the spin collective operators $\langle J_z \rangle$, $\langle J_z^2 \rangle$ and $\langle J_+^2 \rangle$. The concurrence in the given state is then computed from the definition (3.6).

Reprint: Quantum phases and entanglement properties of an extended Dicke model

F.1 Main Achievements

- The thermal and quantum phase diagrams for the EDM are shown.
- Multiple ESQPTs in $j = N/2$ case are identified.
- The way how to distinguish quantum phases in the excited spectrum is proposed.
- Atom-field and atom-atom entanglement is investigated in the excited spectrum. Certain anomalies are detected in relation to some ESQPTs.

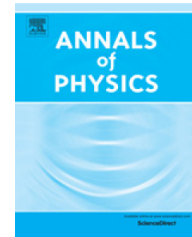


ELSEVIER

Contents lists available at ScienceDirect

Annals of Physics

journal homepage: www.elsevier.com/locate/aop



Quantum phases and entanglement properties of an extended Dicke model



Michal Kloc*, Pavel Stránský, Pavel Cejnar

Institute of Particle and Nuclear Physics, Faculty of Mathematics and Physics, Charles University, V Holešovičkách 2, Prague, 18000, Czech Republic

HIGHLIGHTS

- Dicke-like superradiance model with controllable breaking of integrability is studied.
- Thermal and excited-state quantum phase transitions (ESQPTs) are identified.
- Quantum phases are characterized by energy variations of smoothed expectation values.
- Atom–field and atom–atom entanglement is studied across wide excitation spectrum.
- Anomalies of entanglement are observed at certain ESQPT borderlines.

ARTICLE INFO

Article history:

Received 7 September 2016

Accepted 15 April 2017

Available online 29 April 2017

Keywords:

Single-mode superradiance model

Excited-state quantum phase transitions

Thermal phases

Quantum phases

Entanglement properties of excited states

ABSTRACT

We study a simple model describing superradiance in a system of two-level atoms interacting with a single-mode bosonic field. The model permits a continuous crossover between integrable and partially chaotic regimes and shows a complex thermodynamic and quantum phase structure. Several types of excited-state quantum phase transitions separate quantum phases that are characterized by specific energy dependences of various observables and by different atom–field and atom–atom entanglement properties. We observe an approximate revival of some states from the weak atom–field coupling limit in the strong coupling regime.

© 2017 Elsevier Inc. All rights reserved.

1. Introduction

Since its prediction in 1954 [1], the effect of superradiance has attracted a lot of theoretical and experimental attention [2–4]. Its basic principle – the fact that a coherent interaction of an unexcited

* Corresponding author.

E-mail address: kloc@ipnp.troja.mff.cuni.cz (M. Kloc).

gas with the vacuum of a common field can create a spontaneous macroscopic excitation of both matter and field subsystems – appears in various incarnations in diverse branches of physics [5,6].

The Dicke model [1,7,8] of superradiance resorts to a maximal simplification of the problem to capture the main features of the superradiant transition in the most transparent way. The model shows a thermal phase transition, analyzed and discussed in Refs. [9–12], as well as a zero-temperature (ground-state) Quantum Phase Transition (QPT) [13–15], which was addressed experimentally and realized with the aid of a superfluid gas in a cavity [16–18]. Recent theoretical analyses showed that the model exhibits also a novel type of criticality—the one observed in the spectrum of excited states [19–22]. These so-called Excited-State Quantum Phase Transitions (ESQPTs) affect both the density of quantum levels as a function of energy and their flow with varying control parameters, and are present in a wide variety of quantum models with low numbers of degrees of freedom [23–28].

In this work, we analyze properties of a simple superradiance model interpolating between the familiar Dicke [1] and Tavis–Cummings [7,8] Hamiltonians. A smooth crossover between both limiting cases is achieved by a continuous variation of a model parameter, which allows one to observe the system’s metamorphosis on the way from the fully integrable (hence at least partly understandable) to a partially chaotic (so entirely numerical) regime. One of the aims of our work is to survey the phase-transitional properties of the extended model and to investigate the nature of its *quantum phases*—the domains of the excited spectrum in between the ESQPT critical borderlines. A usual approach to characterize different phases related to the ground state of a quantum system makes use of suitable “order parameters”, i.e., expectation values of some observables. We show that an unmistakable characterization of phases involving excited states is not achieved through the expectation values alone but rather through their different smoothed energy dependences (trends).

The second part of our analysis is devoted to the *entanglement properties of excited states* across the whole spectrum and their potential links to the ESQPTs and quantum phases of the model. It is known that a continuous ground-state QPT in many models (including the present one) is characterized by a singular growth of entanglement within the system, which can be seen as a quantum counterpart of the diverging correlation length in continuous thermal phase transitions [29–36]. A question therefore appears whether there exist any entanglement-related signatures of ESQPTs. The extended Dicke model is rather suitable for a case study of this type since it allows one to analyze at once various types of entanglement—that between the field and all atoms, and that between individual atoms.

The plan of the paper is as follows: Basic quantum and classical features of the model are described in Section 2. Thermal and quantum critical properties and a classification of thermodynamic and quantum phases are presented in Section 3. The atom–field and atom–atom entanglement properties are investigated in Section 4. Conclusions come in Section 5.

2. Extended Dicke model

2.1. Hamiltonian, eigensolutions, classical limit

Consider single-mode electromagnetic field with photon energy ω (polarization neglected) interacting with an ensemble of N two-level atoms, all with the same level energies $\pm\omega_0/2$. The size of the atomic ensemble is assumed to be much smaller than the wavelength of photons (cavity size) so that all atoms interact with the field with the same phase. If we introduce an overall interaction strength λ and an additional interaction parameter δ (whose role will be explained later), the Hamiltonian can be written as

$$\begin{aligned}
 H &= \omega b^\dagger b + \omega_0 \sum_{k=1}^N \frac{1}{2} \sigma_z^k + \frac{\lambda}{\sqrt{N}} \left[(b^\dagger + b) \sum_{k=1}^N \frac{1}{2} (\sigma_+^k + \sigma_-^k) - (1 - \delta) \sum_{k=1}^N \frac{1}{2} (b^\dagger \sigma_+^k + b \sigma_-^k) \right] \\
 &= \underbrace{\omega b^\dagger b + \omega_0 J_z}_{H_{\text{free}}} + \frac{\lambda}{\sqrt{N}} \underbrace{[b^\dagger J_- + b J_+ + \delta b^\dagger J_+ + \delta b J_-]}_{H_{\text{int}}}, \tag{1}
 \end{aligned}$$

where operators b^\dagger and b create and annihilate photons, while σ_\bullet^k stands for the respective Pauli matrix with subscript $\{+, -, z\}$ or $\{x, y, z\}$ acting in the 2-state Hilbert space of the k th atom. The part of H

denoted as H_{free} represents the free Hamiltonian of the field and atomic ensemble, while the part H_{int} constitutes the atom–field interaction with a conveniently scaled strength λ/\sqrt{N} . Defining collective quasi-spin operators $J_{\bullet} = \sum_k \frac{1}{2} \sigma_{\bullet}^k$ for the whole atomic ensemble (which is possible due to the long wavelength assumption), we rewrite the whole Hamiltonian in the simplified form given in the second line of Eq. (1).

The interaction part of the Hamiltonian (1) contains a parameter δ . For $\delta = 1$ we obtain the standard Dicke Hamiltonian [1], in which the interaction is written in the dipole approximation (the dipole operator for the k th atom is proportional to $\sigma_+^k + \sigma_-^k = 2\sigma_x^k$ and the coupling strength in units of energy is given by $\lambda = \omega_0 d N^{1/2} / \epsilon_0 \omega V^{1/2}$, with the electric dipole moment matrix element d , vacuum permittivity ϵ_0 and cavity volume V). This Hamiltonian is sometimes simplified by omitting the terms $b^\dagger \sigma_+^k$ and $b \sigma_-^k$ that for very small λ yield negligible contributions to the transition amplitudes [7,8]. The reduced model with $\delta = 0$, in case of $N > 1$ atoms called the Tavis–Cummings Hamiltonian [8], conserves the sum of atomic and field excitation quanta and is integrable. In this work, following Refs. [21,22], we analyze properties of an extended model across the transition between both the above limiting cases. We assume that parameter δ in Eq. (1) varies smoothly within the interval $\delta \in [0, 1]$, whose boundary values represent the Tavis–Cummings and Dicke Hamiltonians.

The Hamiltonian (1) with any parameter setting conserves the squared quasi-spin $J^2 = J_x^2 + J_y^2 + J_z^2$ with eigenvalues $j(j + 1)$, where j is integer for N even or half-integer for N odd [1]. The full atomic Hilbert space \mathcal{H}_A is the span of all 2^N possible configurations of atoms, but due to the conservation of J^2 the dynamics can be investigated separately in any of the single- j subspaces $\mathcal{H}_A^{j,l}$ with dimension $2j + 1$. The decomposition reads as follows [8]

$$\mathcal{H}_A = \bigotimes_{k=1}^N \underbrace{\mathcal{H}_A^k}_{\mathbb{C}^2} = \bigoplus_{j=0 \text{ or } \frac{1}{2}}^{\frac{N}{2}} \left(\bigoplus_{l=1}^{R_j} \mathcal{H}_A^{j,l} \right), \quad (2)$$

where l enumerates replicas (their number is $R_j = [N!(2j + 1)] / [(\frac{N}{2} + j + 1)!(\frac{N}{2} - j)!]$) of the space with given j differing by the exchange symmetry of atomic components. In the following, we will investigate thermodynamic properties of the model in the full atomic space \mathcal{H}_A , as well as quantum properties in a single- j space $\mathcal{H}_A^{j,l}$. The most natural choice in the latter case is the unique ($R_j = 1$) subspace with maximal value $j = N/2$, which is fully symmetric under the exchange of atoms and therefore emphasizes the collective character of the superradiance phenomenon. A general- j subspace has a mixed exchange symmetry such that only a number $N^* = 2j \leq N$ of atoms can be excited independently, while excitations of the remaining $N - N^*$ atoms have to compensate each other (in Ref. [1] the quantum number j is called a “cooperation number of the atomic gas”). The reduced single- j model has only two effective degrees of freedom f , one associated with the bosonic field, the other with the SU(2) algebra of collective quasi-spin operators, hence $f = 2$ [13,14]. In contrast, in the full (all- j) model the SU(2) algebra of Pauli matrices for each atom brings an independent degree of freedom, so the whole atom–field system has $f = N + 1$.

The Tavis–Cummings Hamiltonian with $\delta = 0$ conserves the sum $M' = b^\dagger b + J_z$ [8]. For any fixed j , the conserved quantity can be written as

$$M = M' + j = \underbrace{b^\dagger b}_n + \underbrace{J_z + j}_{n^*}, \quad (3)$$

where n is the number of field bosons and n^* the number of excited atoms (taking values $n^* = m + j \in [0, N^*]$, where m is the J_z quantum number). The solutions of the $\delta = 0$ model are therefore restricted to any fixed- M subspace $\mathcal{H}_M^{j,l}$ of the full Hilbert space

$$\mathcal{H} = \mathcal{H}_A \otimes \mathcal{H}_F \supset \mathcal{H}_A^{j,l} \otimes \mathcal{H}_F = \bigoplus_{M=0}^{\infty} \mathcal{H}_M^{j,l}. \quad (4)$$

Quantity (3) is not conserved in $\delta \neq 0$ cases, but the full Hamiltonian (1) always conserves “parity” $\Pi = (-)^M$ as the sum of atomic and field excitation quanta is varied only in pairs.

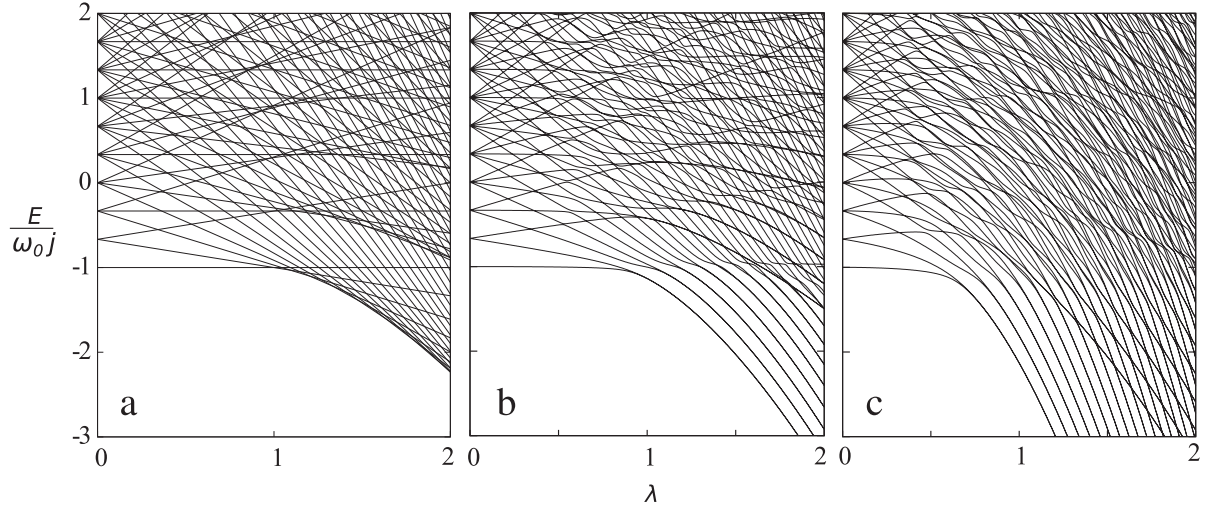


Fig. 1. Spectra of quantum energies of the $j = N/2$ extended Dicke model as a function of λ for $\omega = \omega_0 = 1$ and $N = 6$. The panels correspond to (a) the Tavis–Cummings limit $\delta = 0$, (b) intermediate regime $\delta = 0.3$ and (c) the Dicke limit $\delta = 1$.

Fig. 1 shows quantum spectra of Hamiltonian (1) with $j = N/2$ depending on the interaction parameter λ for three different values of δ . The evolution of the ground state, namely its sudden drop to lower energies above a certain value of λ , indicates the superradiant transition at zero temperature. We note that the eigensolutions of the model for a given j are in general obtained by a numerical diagonalization of Hamiltonian (1) in the space $\mathcal{H}_A^{j,l} \otimes \mathcal{H}_F$ from Eq. (4), using the basis $|m\rangle_A^{j,l} \equiv |m\rangle_A$ in $\mathcal{H}_A^{j,l}$ (with $m = -j, -j+1, \dots, +j$) and $|n\rangle_F$ in \mathcal{H}_F (with $n = 0, 1, 2, \dots$). Since the diagonalization procedure requires a truncation of \mathcal{H}_F , the eigensolutions must be checked for convergence.

A general state vector for any fixed j is expressed as

$$|\psi\rangle = \sum_{m=-j}^{+j} \sum_{n=0}^{\infty} \alpha_{mn} |m\rangle_A |n\rangle_F, \quad (5)$$

where α_{mn} are expansion coefficients satisfying the normalization condition $\sum_{m,n} |\alpha_{mn}|^2 = 1$. Note that for even- and odd-parity states, respectively, the sums in Eq. (5) go either over even or odd values of $M = n + m + j$. Any vector (5) can be visualized as a wave function $\psi(\phi, x)$, where the angle $\phi \in [0, 2\pi)$ comes from the quasi-spin representation of the atomic subsystem and variable $x \in (-\infty, +\infty)$ from the oscillator representation of the bosonic field. For integer j (even N), the wave function can be obtained by substitutions (up to normalization constants) $|m\rangle_A \mapsto e^{im\phi}$ and $|n\rangle_F \mapsto H_n(\omega^{1/2}x)e^{-\omega x^2/2}$, with H_n standing for the Hermite polynomial. For half-integer j (odd N), however, the wave function $\psi(\phi, x)$ acquires a spinorial character. A possible representation on the interval $\phi \in [0, 2\pi)$ can be obtained by coupling an integer angular momentum $j' = j - 1/2$ (the even core of $N - 1$ atoms) with $j'' = 1/2$ (the odd atom) to the total j as in the case of spinor spherical harmonics. This leads to a mapping of $|m\rangle_A$ to a 2-valued function $\propto C_{\pm} e^{i(m \pm 1/2)\phi}$, which is 2π -periodic, with C_{\pm} denoting the corresponding Clebsch–Gordan coefficients. Examples of squared wave functions of the $j = N/2$ Hamiltonian eigenstates for an even N in the medium- δ regime are depicted in Fig. 2. They are taken at the parameter and energy values indicated by dots in Fig. 3(d) ($\delta = 0.3$). All eigenstates have a good parity, which means that their wave functions are symmetric or antisymmetric under the transformation $\phi \mapsto (\phi - \pi) \bmod 2\pi$ and $x \mapsto -x$.

In the following, we will need the classical limit of the model. It is constructed by a simple operator to c-number mappings according to (see, e.g., Ref. [37])

$$(J_x, J_y, J_z) \mapsto j(\sin \theta \cos \phi, \sin \theta \sin \phi, -\cos \theta), \quad (6)$$

$$(b, b^\dagger) \mapsto \frac{1}{\sqrt{2}}(x + ip, x - ip). \quad (7)$$

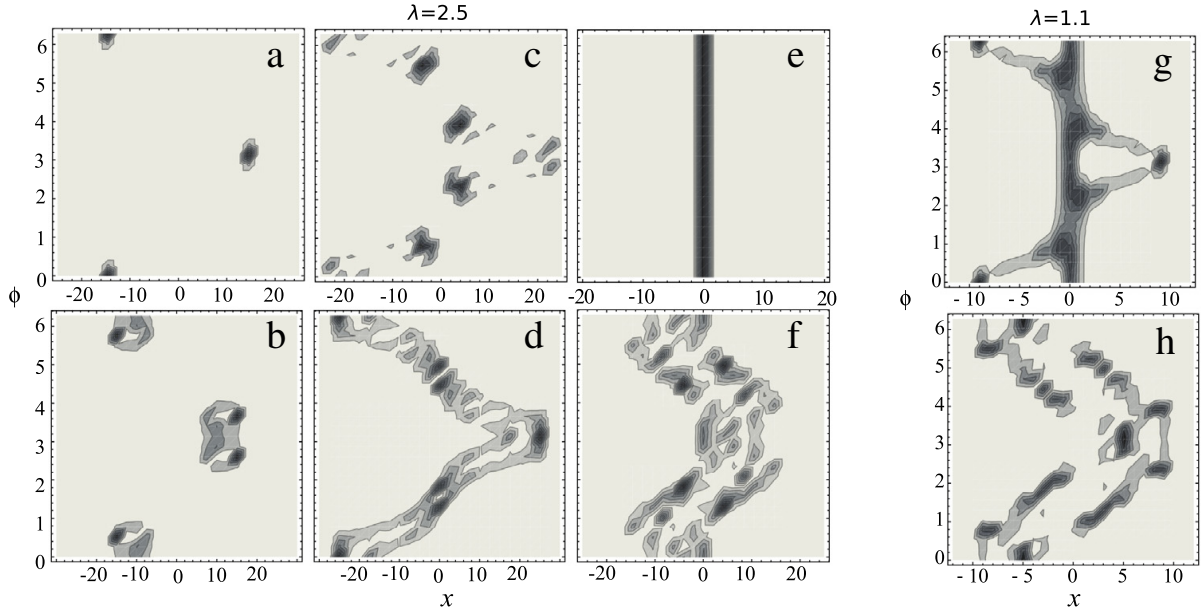


Fig. 2. Squared wave functions $|\psi(\phi, x)|^2$ of selected eigenvectors of the Hamiltonian (1) with $N = 40$, $\omega = \omega_0 = 1$ for $\delta = 0.3$ taken at the $\lambda \times E$ values indicated by dots in Fig. 3(d). Panels (a)–(f), respectively, correspond to the vertical row of points at the right of Fig. 3(d) from bottom to top [panel (a) shows the ground state], panels (g), (h) to the left pair of points. Note that variable ϕ is 2π periodic.

The spherical angles $\phi \in [0, 2\pi)$ and $\theta \in [0, \pi]$ determine the orientation of the classical quasi-spin vector $\vec{j} = (j_x, j_y, j_z)$. Note that angle θ is measured here from the south to the north pole, thus a fully de-excited state of atoms ($j_z = -j$) corresponds to $\theta = 0$ while a maximally excited state of atoms ($j_z = +j$) is associated with $\theta = \pi$. It can be shown that the pair of variables ϕ and $j_z = -j \cos \theta$, respectively, represents canonically conjugate coordinate and momentum associated with the collective states of the atomic subsystem. Similarly, quantities $x \in (-\infty, +\infty)$ and $p \in (-\infty, +\infty)$ in Eq. (7) are suitable coordinate and momentum of the field subsystem. Let us point out that while the atomic phase space for each N is finite (it is a ball with radius j), the field phase space covers the whole plane, expressing the fact that the number of bosons is unlimited. Note that an alternative route to the classical limit of the Dicke model was taken in Refs. [13,14].

The classical Hamiltonian resulting from application of Eqs. (6) and (7) in (1) reads as

$$H_{\text{cl}} = \omega \frac{p^2 + x^2}{2} + \omega_0 j_z + \lambda \sqrt{\frac{2}{N} (j^2 - j_z^2)} \left[(1 + \delta)x \cos \phi - (1 - \delta)p \sin \phi \right] \quad (8)$$

(see also Ref. [22]). Since the classical limit coincides with $j, N \rightarrow \infty$, the above expression needs an appropriate scaling. It is achieved by introducing size-independent quantities $H_{\text{cl}}/2j$ and $j_z/2j$ together with $(x, p)/\sqrt{2j}$. Their application in Eq. (8) leads to an expression for scaled energy containing an effective coupling strength $\lambda_{\text{eff}} \equiv \lambda \sqrt{2j/N}$, which increases with j and reaches the bare λ for the maximal $j = N/2$.

Since the parameter δ drives the system away from the integrable Tavis–Cummings limit, it is relevant to measure the degree of chaos present at various stages of the transition to the Dicke limit. We note that chaos in the basic and extended Dicke model was studied also in Refs. [13,14,38–40]. Classical chaos in a general Hamiltonian (8) can be quantified by a so-called regular fraction f_{reg} . It is defined as the volume of the phase space domain filled with regular orbits relative to the total phase space volume available at given energy E :

$$f_{\text{reg}}(E) = \frac{\int d\phi dj_z dx dp \delta(E - H_{\text{cl}}) \chi_{\text{reg}}}{\int d\phi dj_z dx dp \delta(E - H_{\text{cl}})}. \quad (9)$$

Here, $\chi_{\text{reg}}(\phi, j_z, x, p)$ stands for a characteristic function defining the regular part of the phase space, i.e., the domain where classical dynamics is regular in the sense of vanishing Lyapunov exponents

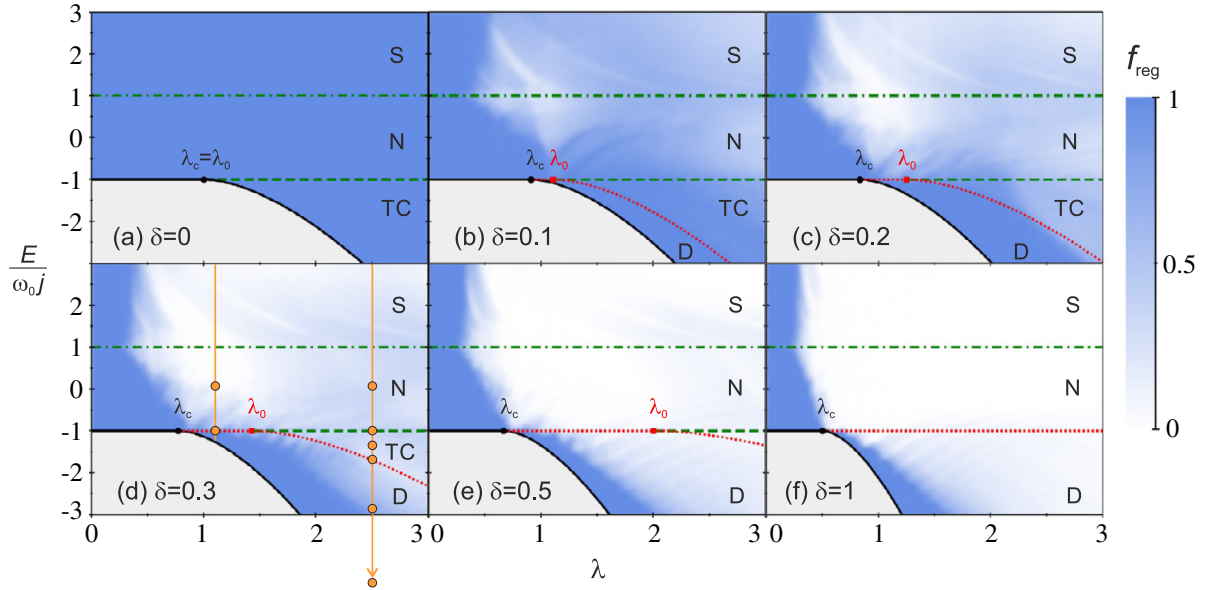


Fig. 3. (Color online) The $\lambda \times E$ maps of the single- j model with $\omega = \omega_0 = 1$ for six values of parameter δ . Tones of blue indicate the classical regular fraction (9). The curves correspond to the ground state energy E_0 (full line) and the critical esQPT energies E_{c1} (dotted), E_{c2} (dashed), and E_{c3} (dash-dotted) from Eqs. (29)–(31). Acronyms D (Dicke), TC (Tavis–Cummings), N (normal) and S (saturated) indicate different “quantum phases” of the model (Section 3.2). Dots in panel (d) mark places where wave functions in Fig. 2 are taken.

($\chi_{\text{reg}} = 1$ in the regular part and $\chi_{\text{reg}} = 0$ in the chaotic part). The way how the regular fraction is obtained from numerical simulation of classical dynamics is described in Ref. [41].

The evolution of the classical regular fraction for Hamiltonian (8) with δ increasing from 0 to 1 is shown in Fig. 3. Each panel displays a map of f_{reg} for a given δ in the plane $\lambda \times E$. The value of f_{reg} is encoded into the tones of blue: the full color indicates perfectly regular areas ($f_{\text{reg}} = 1$) and white completely chaotic ones ($f_{\text{reg}} = 0$). Not surprisingly, we observe that the degree of chaos exhibits an overall increase with δ . However, even in the Dicke limit $\delta = 1$ the model is not entirely chaotic. The most chaotic domain in all $\delta > 0$ panels is that with parameter λ above the superradiant transition and energy E exceeding a certain value above the ground-state E_0 . Besides the main trends in the dependence of f_{reg} we also observe some surprising fine structures—for instance the “ribs” in panels (d)–(f).

2.2. Classical and quantum solutions with fixed M for $\delta = 0$

Finding eigensolutions of Hamiltonian (1) is much simpler in the $\delta = 0$ limit [8]. In that case, the additional conserved quantity (3) splits the Hilbert space $\mathcal{H}_A^{j,l} \otimes \mathcal{H}_F$ from Eq. (4) into a sum of dynamically invariant subspaces $\mathcal{H}_M^{j,l}$. These are spanned by states $|m\rangle_A |n\rangle_F$ satisfying constraint $n + m = M - j$ and therefore have dimension $d(j, M) = \min\{2j, M\} + 1$. As seen in Fig. 1(a), the full $\delta = 0$ spectrum is comprised of a number of mutually non-interacting (crossing each other) spectra with different values of M . Each of these fixed- M spectra is obtained by truncation-free diagonalization in a finite dimension. Using the unperturbed basis $|i\rangle \equiv |m = -j + i\rangle_A |n = M - i\rangle_F$ enumerated by $i = 0, \dots, \min\{2j, M\}$, we express the $\delta = 0$ Hamiltonian in a single M -subspace in the following tridiagonal form:

$$\langle i|H|i'\rangle = \underbrace{[\omega(M - i) + \omega_0(i - j)]}_{E_i(0)} \delta_{ii'} + \lambda \underbrace{\sqrt{\frac{(i+1)(2j-i)(M-i)}{N}}}_{H'_{ii'}} [\delta_{i(i'-1)} + \delta_{(i-1)i'}]. \quad (10)$$

Examples of single- M spectra obtained from this Hamiltonian are given in Fig. 4.

The simplest spectrum shown in Fig. 4(a) corresponds to the *tuned* case with $\omega = \omega_0$. The eigenvalues of the tuned Hamiltonian (10) read as $E_i = E(0) + \lambda E'_i$, where $E(0) = \omega(M - j)$ and

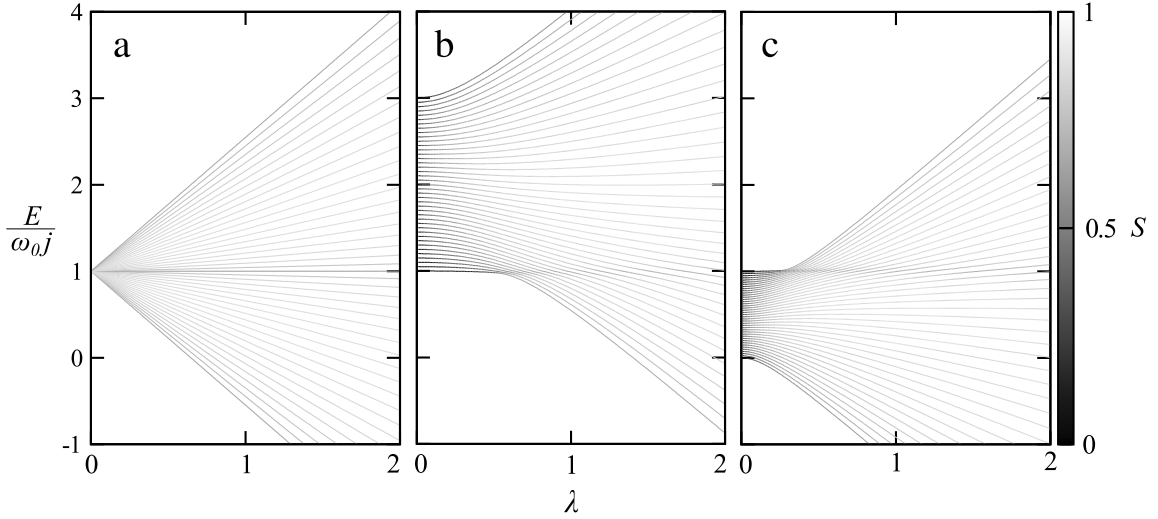


Fig. 4. The $j = N/2$ spectrum (for $N = 40$) in the $M = 2j$ subspace for the $\delta = 0$ model with $\omega = \omega_0 = 1$ (panel a), $\omega = 2, \omega_0 = 1$ (panel b) and $\omega = 0.5, \omega_0 = 1$ (panel c). The wave-function entropies \mathcal{S} of individual eigenstates in the unperturbed basis $|m\rangle_A|n\rangle_F$ are encoded in the varying shade of the corresponding lines.

E'_i are eigenvalues of $H'_{i'}$. Since the latter come in pairs with opposite signs (for odd dimensions there is an additional unpaired eigenvalue $E'_i = 0$), the spectrum linearly expands with increasing λ around $E(0)$. The full spectrum in Fig. 1(a) results just from a pile up of spectra similar to that from Fig. 4(a) with all values of M . Moreover, as the eigenvectors of matrix (10) with $\omega = \omega_0$ coincide with those of $H'_{i'}$, they do not depend on λ . This is also verified in Fig. 4(a), where the wave-function entropy $\mathcal{S}(\lambda)$ of individual eigenstates in the unperturbed basis is encoded in the shade of the respective line. The constancy of $\mathcal{S}(\lambda)$ for each state confirms the absence of its structural evolution. The wave-function entropy for a general state (5) with respect to the basis $|m\rangle_A|n\rangle_F$ is defined by the expression

$$\mathcal{S}(\psi) = -\frac{1}{\ln(2j+1)} \sum_{m,n} |\alpha_{mn}|^2 \ln |\alpha_{mn}|^2 \quad (11)$$

(cf. Ref. [42]), so it measures the degree of delocalization of the given state in the fixed basis. The minimal value $\mathcal{S} = 0$ is assigned to any of the basis states (no delocalization), while the maximum $\mathcal{S} = \ln d(j, M) / \ln(2j+1)$ is taken by a uniformly distributed superposition of all basis states (maximal delocalization). In Section 4 we will show that Eq. (11) quantifies the atom–field entanglement contained in the given state for $\delta = 0$.

The spectrum of a *detuned* Hamiltonian with $\omega \neq \omega_0$ is less trivial. Examples of level dynamics in a single- M subspace and the corresponding wave-function entropies for $\omega > \omega_0$ and $\omega < \omega_0$ are shown in panels (b) and (c) of Fig. 4. We see that the eigenvalues are no more straight lines and that the eigenvectors change with λ . The peculiar shapes of these spectra will be explained in Section 3.2, here we only point out that the tuned situation is restored in an approximate sense for very large λ , when the last term in the detuned Hamiltonian $H = \omega(n + J_z) - \lambda H_{\text{int}} / \sqrt{N} - (\omega - \omega_0) J_z$ becomes negligible. Therefore, investigating properties of the model for large coupling strengths, one can make an assumption that $\omega \approx \omega_0$.

Let us finally return to the classical analysis, now focused specifically on the $\delta = 0$ system. The conservation of quantity M from Eq. (3) introduces particular correlations between the degrees of freedom associated with atomic and field subsystems. As a consequence, the system with $f = 2$ degrees of freedom is for any fixed value of M reduced to a system with just a single effective degree of freedom. To make this explicit, we employ a transformation

$$\begin{pmatrix} x \\ p \\ \phi \\ j_z \end{pmatrix} \mapsto \begin{pmatrix} x' = x \cos \phi - p \sin \phi \\ p' = p \cos \phi + x \sin \phi \\ \phi' = \phi + j_z + (p^2 + x^2)/2 \\ M' = j_z + (p^2 + x^2)/2 \end{pmatrix}, \quad (12)$$

where $M' = M - j$ is conserved. It can be checked that this transformation is canonical, so (x', p') and (ϕ', M') are new pairs of conjugate coordinates and momenta. The (x', p') variables for each M' satisfy a constraint $(x'^2 + p'^2)/2 \in [\max\{0, M' - j\}, M' + j]$, so they form a disc (for $M' \leq j$) or an annulus (for $M' > j$). The classical Tavis–Cummings ($\delta = 0$) Hamiltonian in terms of the new variables becomes

$$H_{\text{cl}}^{\text{TC}} = (\omega - \omega_0) \frac{p'^2 + x'^2}{2} + \omega_0 M' + \lambda x' \sqrt{\frac{2}{N} \left[j^2 - \left(M' - \frac{p'^2 + x'^2}{2} \right)^2 \right]}, \quad (13)$$

which for a constant M' depends only on (x', p') , so has effectively $f = 1$ degree of freedom. This not only guarantees the full integrability of the $\delta = 0$ model, but also results in some emergent critical phenomena which will be discussed below.

3. Phases and phase transitions

3.1. Thermal phase transition

The extended Dicke Hamiltonian (1) has a complex phase structure [21,22,43]. In this section, we analyze thermal phase transition of the full model with atomic Hilbert space (2) and the number of degrees of freedom $f = N + 1$. Following the standard approach described in Ref. [9], we use the Glauber coherent states $|\alpha\rangle \propto e^{\alpha b^\dagger} |0\rangle$, where $\alpha \equiv (\alpha' + i\alpha'') \in \mathbb{C}$ is an eigenvalue of the b operator and $|0\rangle$ denotes the field vacuum. An average number of bosons $\langle n \rangle_\alpha = \langle \alpha | b^\dagger b | \alpha \rangle = |\alpha|^2$ in the state $|\alpha\rangle$ represents an indicator of the transition from normal to superradiant phase: $\langle n \rangle_\alpha = 0$ in the normal phase and $\langle n \rangle_\alpha \sim \mathcal{O}(N)$ in the superradiant phase. On the way to the thermodynamic limit $N \rightarrow \infty$, it is convenient to perform the scaling transformation $\alpha \mapsto \bar{\alpha} = \alpha/\sqrt{N}$, so that the scaled coherent-state variable $\bar{\alpha} \equiv \bar{\alpha}' + i\bar{\alpha}''$ becomes a suitable complex order parameter of the superradiant phase transition.

We start by introducing two special values of the atom–field coupling strength:

$$\lambda_c = \frac{\sqrt{\omega\omega_0}}{1 + \delta}, \quad \lambda_0 = \frac{\sqrt{\omega\omega_0}}{1 - \delta}. \quad (14)$$

While the first one will be shown to represent a critical strength for the occurrence of the superradiant phase, the second value will turn out to be a strength at which a specific form of the superradiant phase occurs for $\delta \in (0, 1)$. To get an equilibrium field configuration at a given temperature T (measured in energy units), we minimize in variable $\bar{\alpha}$ a scaled free energy $F_{\bar{\alpha}}(T)/N = -T \ln Z_{\bar{\alpha}}(T)/N$, where $Z_{\bar{\alpha}}(T) = \langle \bar{\alpha} | \text{Tr}_A e^{-H/T} | \bar{\alpha} \rangle$ is the partition function, calculated for a given $\bar{\alpha}$ from a partial trace of the Hamiltonian exponential over the full atomic Hilbert space (2). For Hamiltonian (1) this procedure yields

$$Z_{\bar{\alpha}}(T) = e^{-\frac{\omega|\bar{\alpha}|^2}{T}} \text{Tr}^N \exp \left\{ -\frac{1}{T} \begin{pmatrix} \frac{1}{2}\omega_0 & \lambda [(1 + \delta)\bar{\alpha}' + i(1 - \delta)\bar{\alpha}''] \\ \lambda [(1 + \delta)\bar{\alpha}' - i(1 - \delta)\bar{\alpha}''] & \frac{1}{2}\omega_0 \end{pmatrix} \right\}. \quad (15)$$

The two eigenvalues of the matrix in the exponential are

$$\pm \sqrt{\left(\frac{\omega_0}{2}\right)^2 + \lambda^2 [(1 + \delta)^2 \bar{\alpha}'^2 + (1 - \delta)^2 \bar{\alpha}''^2]} \equiv \pm e_{\bar{\alpha}}, \quad (16)$$

which leads to a simple expression of the scaled free energy:

$$\frac{1}{N} F_{\bar{\alpha}}(T) = \omega |\bar{\alpha}|^2 - T \ln \left(2 \cosh \frac{e_{\bar{\alpha}}}{T} \right). \quad (17)$$

Stationary points of $F_{\bar{\alpha}}(T)/N$ can be obtained from a simple analysis. The first derivative in variable $\bar{\alpha}'$ or $\bar{\alpha}''$, respectively, vanishes at the points satisfying the first or second line of the following array:

$$\bar{\alpha}' = 0 \quad \text{or} \quad 2\omega e_{\bar{\alpha}} = \lambda^2(1 - \delta)^2 \tanh \frac{e_{\bar{\alpha}}}{T}, \quad (18)$$

$$\bar{\alpha}'' = 0 \quad \text{or} \quad 2\omega e_{\bar{\alpha}} = \lambda^2(1 + \delta)^2 \tanh \frac{e_{\bar{\alpha}}}{T}. \quad (19)$$

The point $\bar{\alpha} = 0$ is always a trivial solution of both lines, but additional solutions appear for $\lambda > \lambda_c$. This coupling strength represents a critical point where the normal phase $\bar{\alpha} = 0$ becomes unstable at the lowest temperatures and a new, superradiant equilibrium is created at some non-zero values of $\bar{\alpha}$. The critical temperature for the superradiant transition, i.e., the upper temperature limit for the existence of the $\bar{\alpha} \neq 0$ solution in the region $\lambda > \lambda_c$, is

$$T_c = \frac{\omega_0}{2} \operatorname{artanh}^{-1} \frac{\lambda_c^2}{\lambda^2}. \quad (20)$$

For $T > T_c$, the stable equilibrium of the system is again only the normal solution $\bar{\alpha} = 0$.

For $\delta = 0$ (the Tavis–Cummings limit), both right-side conditions in Eqs. (18) and (19) become identical and yield a solution $|\bar{\alpha}| = \text{const}$ that grows from zero with increasing difference $\lambda - \lambda_c$. Therefore, the superradiant minimum of the free energy forms a circle around $\bar{\alpha} = 0$. For $\delta > 0$, however, a simultaneous solution of both right-side conditions in (18) and (19) is no more possible. The superradiant equilibrium is then represented by a pair of points on the real axis, $(\bar{\alpha}', \bar{\alpha}'') = (\pm\bar{\alpha}'_0, 0)$, where $\bar{\alpha}'_0 > 0$ solves the right-side equation in (18). If $\delta < 1$ and $\lambda > \lambda_0$, a pair of saddle points appears for low temperatures on the imaginary axis, $(\bar{\alpha}', \bar{\alpha}'') = (0, \pm\bar{\alpha}''_0)$, where $\bar{\alpha}''_0 \geq \bar{\alpha}'_0$ solves the right-side equation in (19). These unstable solutions exist for temperatures below

$$T_0 = \frac{\omega_0}{2} \operatorname{artanh}^{-1} \frac{\lambda_0^2}{\lambda^2}. \quad (21)$$

A possibility of thermodynamic quasi-equilibrium states associated with the saddle points of free energy (17) was recently discussed in Ref. [43].

A thermal phase diagram in the $\lambda \times T$ plane for $\delta = 0.3$ is shown in Fig. 5 along with samples of the free energy landscapes in various phases and at $T = T_c$. The critical temperature T_c from Eq. (20) determines the phase transition between the superradiant and normal (acronym N) phases of the model. The superradiant phase exists in two forms: the Tavis–Cummings phase (acronym TC) with the saddles in the free energy landscape and the Dicke phase (acronym D) without the saddles. While the TC phase is the only type of superradiant phase in the Tavis–Cummings limit (where $\lambda_0 \rightarrow \lambda_c$ and $T_0 \rightarrow T_c$), the D phase is exclusive in the Dicke limit (in which $\lambda_0 \rightarrow \infty$). For intermediate δ both phases coexist, being separated by temperature T_0 from Eq. (21). Let us stress that the TC \rightarrow D transition (in contrast to D \rightarrow N) is not a phase transition in the standard sense since it does not affect the global minimum of the free energy.

3.2. Ground-state and excited-state quantum phase transitions

We return now to the analysis of the extended Dicke model with the restriction to a single- j collective subspace of atomic states. The number of relevant degrees of freedom of the single- j model is $f = 2$, independently of the size parameter N , which implies that the infinite-size limit, $N \rightarrow \infty$, coincides with the classical limit [19,26]. Both ground-state and excited-state quantum phase transitions can be predicted from the classical version of the model, namely from the behavior of stationary points of the classical Hamiltonian (8). In particular, the ESQPTs result from singularities (non-analyticities) in the semiclassical density of states

$$\varrho_{\text{cl}}(E) = \frac{\partial}{\partial E} \frac{1}{(2\pi)^2} \int d\phi dj_z dx dp \Theta(E - H_{\text{cl}}), \quad (22)$$

where $\Theta(x)$ is the step function ($\Theta = 0$ for $x < 0$ and $\Theta = 1$ for $x \geq 0$), that appear at the points satisfying $\nabla H_{\text{cl}} = 0$ (with ∇ standing for the gradient in the phase space).

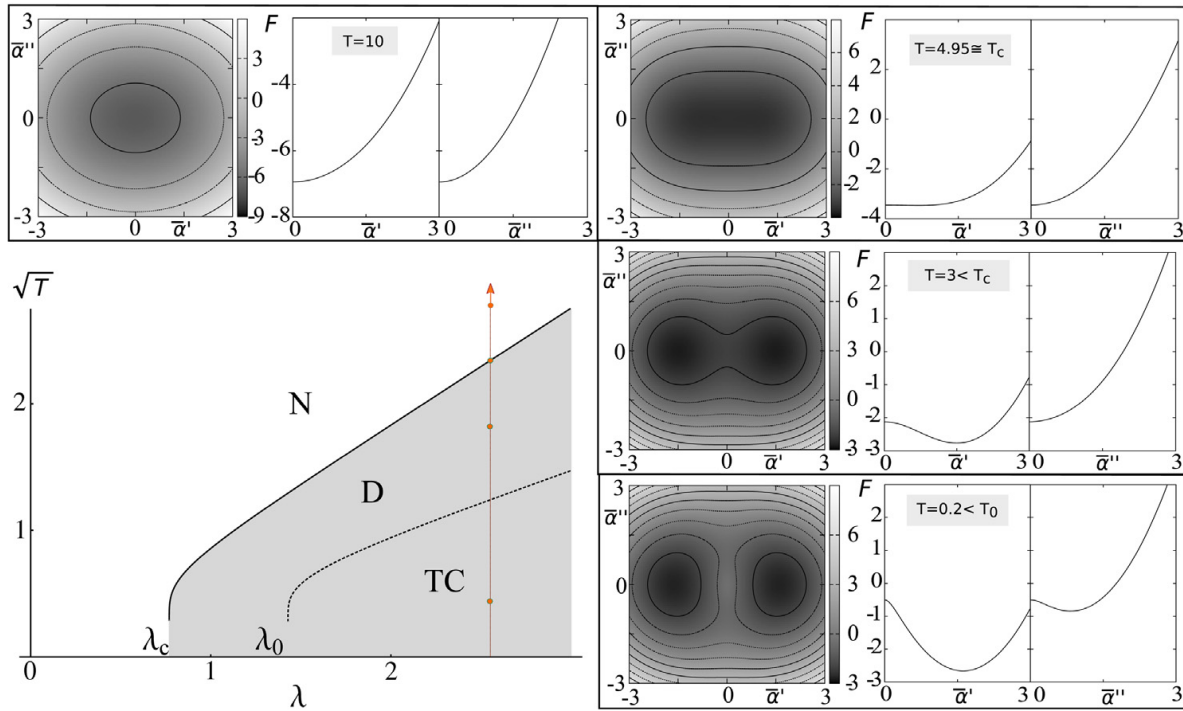


Fig. 5. Thermal phase diagram of the all- j model ($\omega = \omega_0 = 1, \delta = 0.3$) and sample landscapes of the scaled free energy at the $\lambda = 2.5$ cut of the phase diagram (vertical line). The full curve in the phase diagram marks the critical temperature T_c for the transition to the normal (N) phase, while the dotted curve indicates the temperature T_0 separating the TC and D superradiant phases (with or without saddles of free energy). The free energy landscapes in the complex- α plane are, for selected temperatures, visualized by contour-shade plots (darker areas indicate lower values) and by the cuts along real and imaginary axes.

It has been shown [28] that the ESQPTs caused by non-degenerate stationary points – those which are locally quadratic as their Hessian matrix of second derivatives has only non-zero eigenvalues – can be classified by a pair of numbers (f, r) , where a so-called index of the stationary point r is a number of negative eigenvalues of the Hessian matrix. In particular, for $f = 2$, the first derivative of the level density in a vicinity of a stationary-point energy E_c behaves as

$$\frac{\partial \rho_{cl}}{\partial E} \propto \begin{cases} (-)^{r/2} \Theta(E - E_c) & \text{for } r = 0, 2, 4 \\ (-)^{(r+1)/2} \ln |E - E_c| & \text{for } r = 1, 3 \end{cases} \quad (23)$$

hence exhibits either a jump (for r even) or a logarithmic divergence (for r odd) at the critical energy E_c .

In the present case, the evaluation of the level density according to Eq. (22) can be simplified with the aid of the volume-preserving substitution

$$\begin{pmatrix} x \\ p \end{pmatrix} \mapsto \begin{pmatrix} \xi = x + \frac{(1 + \delta)\lambda}{\omega} \sqrt{\frac{2}{N}} (j^2 - j_z^2) \cos \phi \\ \eta = p - \frac{(1 - \delta)\lambda}{\omega} \sqrt{\frac{2}{N}} (j^2 - j_z^2) \sin \phi \end{pmatrix}, \quad (24)$$

which transforms the classical Hamiltonian (8) to the form

$$H'_{cl} = \omega \frac{\eta^2 + \xi^2}{2} + \underbrace{\omega_0 j_z - \frac{\lambda^2}{\omega} \frac{j^2 - j_z^2}{N}}_{h_{cl}(\phi, j_z)} (1 + 2\delta \cos 2\phi + \delta^2) \quad (25)$$

with fully separated variables of the field and atomic subsystems. Although the mapping (24) does not represent a canonical transformation (so ξ, η is not a new coordinate–momentum pair—otherwise

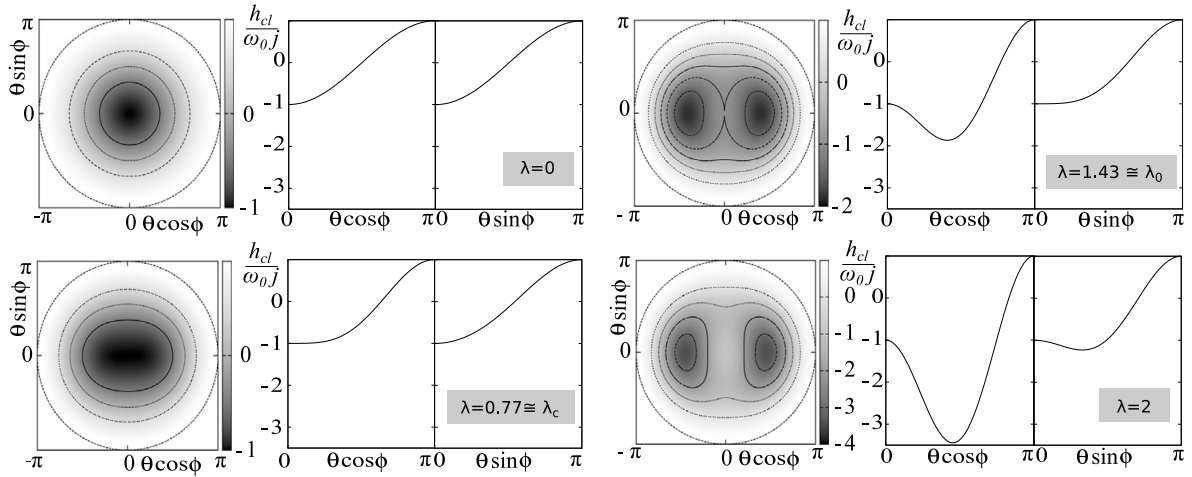


Fig. 6. The function h_{cl} from Eq. (25) in the phase space of the atomic subsystem defined by spherical angles θ and ϕ for $\omega = \omega_0 = 1$ and $\delta = 0.3$. Various panels correspond to the indicated values of the coupling strength λ . Each contour-shade polar plot (with $\phi \equiv$ angle and $\theta \equiv$ radius) is accompanied by the corresponding horizontal and vertical cuts.

the model would be separable and thus fully integrable for any δ), it simplifies the analysis of the level density. In particular, the integration in Eq. (22) over variables ξ, η , on which the transformed Hamiltonian depends quadratically, can be performed explicitly (cf. Ref. [26], where an analogous calculation is performed for a Hamiltonian with a quadratic kinetic term). The result is a simplified expression

$$\rho_{cl}(E) = \frac{1}{2\pi\omega} \int d\phi dj_z \Theta(E - h_{cl}), \quad (26)$$

in which the integration, involving function $h_{cl}(\phi, j_z)$ defined in Eq. (25), goes only over the 2-dimensional collective phase space of the atomic subsystem—a ball with radius j . Eq. (26) is proportional to an area of the ball region where h_{cl} takes values less than (or equal to) the chosen energy E , hence it can be visualized as flooding of a landscape with profile h_{cl} on a globe. The h_{cl} function for selected values of λ and δ is depicted in Fig. 6.

It is clear from the expression (25) that the stationary points of H_{cl} in all four variables correspond to $\xi, \eta = 0$ and ϕ, j_z determined as stationary points of the function h_{cl} . Since the quadratic minimum in variables ξ, η has a null index, any stationary point of H_{cl} has an index r equal to that of the corresponding stationary point of h_{cl} . For the determination of ESQPTS it is therefore sufficient to find and classify stationary points of the function h_{cl} on a ball. Non-degenerate stationary points of h_{cl} with index $r = 0, 1$, and 2 cause, respectively, an upward jump, logarithmic divergence and a downward jump of $\partial\rho_{cl}/\partial E$.

Taking into account that the effective coupling parameter λ_{eff} in the scaled classical Hamiltonian is reduced with respect to actual λ by a factor $\sqrt{2j/N}$, see the text below Eq. (8), we obtain from Eq. (14) the following j -dependent values of the critical couplings:

$$\lambda_c(j) = \sqrt{\frac{N}{2j}} \frac{\sqrt{\omega\omega_0}}{1+\delta}, \quad \lambda_0(j) = \sqrt{\frac{N}{2j}} \frac{\sqrt{\omega\omega_0}}{1-\delta}. \quad (27)$$

These will play the roles of λ_c and λ_0 in individual subspaces of states with fixed values of j . Note that in the highest subspace with $j = N/2$ both expressions in Eq. (27) yield the bare values of critical couplings. A straightforward analysis leads to the following conclusions:

(i) Stationary points with $r = 0$ represent the global minimum of both h_{cl} and H_{cl} functions, demarcating the ground state of the $N \rightarrow \infty$ system. The minimum appears at $j_z = -j$ (ϕ arbitrary) for $\lambda < \lambda_c(j)$, and at $j_z = -j\lambda_c(j)^2/\lambda^2$, $\phi = 0$ and π (a pair of degenerate minima) for $\lambda \geq \lambda_c(j)$. The

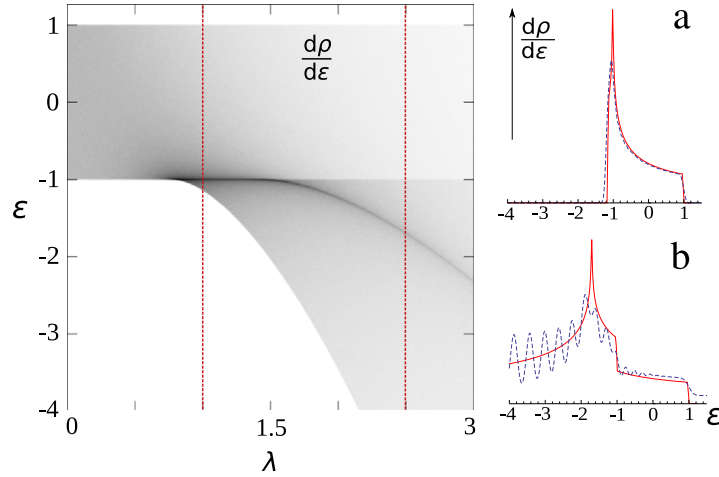


Fig. 7. Energy derivative of the semiclassical level density, $\partial \varrho_{\text{cl}}/\partial E$, for the single- j model with $\omega = \omega_0 = 1$ and $\delta = 0.3$ as a function of λ and $\varepsilon \equiv E/(\omega_0 j)$. The shade diagram in the left panel was obtained from Eq. (26); darker areas represent larger values and vice versa. Panels (a) and (b) show cuts (full curves) at (a) $\lambda = 1$ and (b) $\lambda = 2.5$ in comparison with finite-size results (dashed curves) based on numerical diagonalization of the Hamiltonian for $N = 40$ and Gaussian smoothening of the spectrum ($\sigma = 0.04$ and 0.07 for $\lambda = 1$ and 2.5 , respectively). Scales in panels (a),(b) are arbitrary and not the same.

ground-state energy is given by the formula

$$E_0(j) = \begin{cases} -\omega_0 j & \text{for } \lambda \in [0, \lambda_c(j)), \\ -\frac{1}{2} \omega_0 j \left[\frac{\lambda_c(j)^2}{\lambda^2} + \frac{\lambda^2}{\lambda_c(j)^2} \right] & \text{for } \lambda \in [\lambda_c(j), \infty), \end{cases} \quad (28)$$

which exhibits a second-order QPT from normal to superradiant ground-state phase at the critical coupling $\lambda_c(j)$, where $d^2 E_0/d\lambda^2$ has a discontinuity.

(ii) Stationary points with $r = 1$ represent saddles of h_{cl} . They are located at $j_z = -j$ (ϕ arbitrary) for $\lambda_c(j) \leq \lambda < \lambda_0(j)$, and at $j_z = -j\lambda_0(j)^2/\lambda^2$, $\phi = \pi/2$ and $3\pi/2$ for $\lambda \geq \lambda_0(j)$. These stationary points correspond to an ESQPT (a logarithmic divergence of $\partial \varrho_{\text{cl}}/\partial E$) at the critical energy

$$E_{c1}(j) = \begin{cases} -\omega_0 j & \text{for } \lambda \in [\lambda_c(j), \lambda_0(j)), \\ -\frac{1}{2} \omega_0 j \left[\frac{\lambda_0(j)^2}{\lambda^2} + \frac{\lambda^2}{\lambda_0(j)^2} \right] & \text{for } \lambda \in [\lambda_0(j), \infty). \end{cases} \quad (29)$$

For $\delta \rightarrow 1$ we have $\lambda_0(j) \rightarrow \infty$ and Eq. (29) is reduced to its first line.

(iii) Stationary points with $r = 2$ are maxima of h_{cl} at $j_z = -j$ (ϕ arbitrary) for $\lambda \geq \lambda_0(j)$ and at $j_z = +j$ (ϕ arbitrary) for $\lambda \geq 0$. Related ESQPTs (downward jumps of $\partial \varrho_{\text{cl}}/\partial E$) appear at critical energies

$$E_{c2}(j) = -\omega_0 j \quad \text{for } \lambda \in [\lambda_0(j), \infty), \quad (30)$$

$$E_{c3}(j) = +\omega_0 j \quad \text{for } \lambda \in [0, \infty). \quad (31)$$

The second maximum of h_{cl} at energy (31) is the global one, so for $E \geq E_{c3}$ the formula (26) yields a constant (saturated) value of the level density equal to $\varrho_{\text{cl}} = 2j/\omega$.

All ESQPT critical borderlines E_{c1} , E_{c2} and E_{c3} from Eqs. (29)–(31) for various values of δ are demarcated in Fig. 3. Their existence is numerically verified in Fig. 7, which depicts the $\lambda \times E$ dependence of $\partial \varrho_{\text{cl}}/\partial E$ for $j = N/2$ somewhere in between the Dicke and Tavis–Cummings limits. The shade plot was obtained through the phase-space integration in Eq. (26) and a comparison with results obtained by a numerical diagonalization is shown in the two panels on the right. We stress that due to the $f = 2$ character of our model, the ESQPT singularities occur in the *first derivative* of the level density with respect to energy. However, the conservation of quantity (3) in the $\delta = 0$ limit and the corresponding reduction of the number of effective degrees of freedom to $f = 1$ (see Section 2.2) leads to a possibility to generate an ESQPT singularity in the *level density itself*.

Such an effect can really be identified within a particular *single* M -subspace of the full model. The lowest-energy state of any of such subspaces for $N \rightarrow \infty$ coincides with the global minimum of classical Hamiltonian (13) within the available (for a given M) domain of the phase space. It turns out that the most interesting M -subspace is the one with $M = 2j$. This particular subset of states exhibits for $\omega > \omega_0$ a second-order ground-state QPT at the coupling strength λ equal to a critical value

$$\lambda'_c(j) = \sqrt{\frac{N}{2j} \frac{\omega - \omega_0}{2}}. \quad (32)$$

At this coupling, the main minimum of function (13) moves from $(x', p') = (0, 0)$ away to $x' < 0$ while $(0, 0)$ becomes an inflection point. The inflection point is present for $\lambda \in (\lambda'_c(j), \infty)$ and generates an ESQPT (a logarithmic divergence of the level density in the $M = 2j$ subspace) at energy E_{c3} from Eq. (31). Note that for $\omega < \omega_0$ the ESQPT appears for $\lambda > |\lambda'_c(j)|$ at the upper energy of the unperturbed spectrum.

This effect, addressed already in Ref. [19], is demonstrated in Fig. 8. It displays a shade plot of the semiclassical density of levels with $M = 2j$ (obtained by the $f = 1$ phase-space integration) and the underlying forms of the Hamiltonian (13). A finite-size sample of the predicted singularity in the level density was seen in panel (b) of Fig. 4. A more detailed analysis of Eq. (13) shows that the present type of criticality is absent in the $M \neq 2j$ subspaces. This can be intuitively understood from the evaluation of matrix elements $H'_{ii'}$ of the interaction Hamiltonian with $\delta = 0$ in the unperturbed basis, see Eq. (10). The interaction matrix elements quantify the mixing induced by H_{int} in the unperturbed eigenbasis of H_{free} . Neglecting the trivial state with $M = 0$ which does not mix at all, the matrix elements $H'_{ii'}$ are particularly small in the $M = 1$ subspace (dimension 2) and for the $i = 2j$ state of the $M = 2j$ subspace (dimension $2j + 1$). Only the latter state can develop a singularity in the $j, N \rightarrow \infty$ limit. It is the state $|m = +j\rangle_A |n = 0\rangle_F$, which for $\omega > \omega_0$ represents the lowest state of the $M = 2j$ subspace, while for $\omega < \omega_0$ it is the highest state; cf. panels (b) and (c) of Fig. 4. Although the $M \neq 2j$ subspaces show no quantum critical effects, it is interesting to realize that a pile up of all M -subspaces produces the downward jump of $\partial \varrho_{\text{cl}} / \partial E$ (with ϱ_{cl} standing for the total semiclassical level density), as observed in the $E = E_{c3}$ ESQPT of the $\delta = 0$ system.

3.3. Quantum phases

The critical borderlines E_{c1} , E_{c2} and E_{c3} in the $\lambda \times E$ plane separate spectral domains that we consider to constitute different “quantum phases” of the model (in analogy to thermodynamic phases). They are denoted by acronyms D (Dicke), TC (Tavis–Cummings), N (normal) and s (saturated), see Fig. 3. Both phases D and TC, which coexist for δ in between 0 and 1, contain quantum states of a superradiant nature because their energy is lowered with respect to the minimal non-radiant value $E = -\omega_0 j$. In the limits of δ , the model shows only one type of the superradiant phase: TC for the Tavis–Cummings limit $\delta = 0$ and D for the Dicke limit $\delta = 1$. In contrast, both phases N and s contain states that resemble excitations in the fully non-radiant regime at $\lambda = 0$. The s phase above E_{c3} yields a constant, saturated value of level density ϱ_{cl} .

While the definition of ESQPTs is obvious from the behavior of quantities like level density at the critical energies, the meaning of quantum phases in between the critical energies is not a priori clear. It should be looked for in the structure of the energy eigenstates in the corresponding energy domains. However, sample wave functions in Fig. 2 [where panels (a), (b), (d), (f) and (h) correspond to phases D, D, TC, N and N, respectively] indicate that individual eigenstates do not show sufficient clues for the identification of phases. We therefore resort to a more efficient visualization tool allowing us a bulk inspection of the eigenstate properties, namely to the method of so-called *Peres lattices* [44]. It was proven useful in various models (see Ref. [45] and references therein) including the Dicke model [22,38]. A general Peres lattice shows expectation values $\langle P \rangle_i = \langle \psi_i | P | \psi_i \rangle$ of a selected observable P in individual energy eigenstates $|\psi_i\rangle$ (enumerated by integer i) arranged into lattices with energy E_i on one of the axes. Examples of Peres lattices for observables (a) $J_z = n^* - j$ and (b) $n = b^\dagger b$ are shown in the respective panels of Fig. 9. Their comparison with the map of chaos in Fig. 3(d) shows

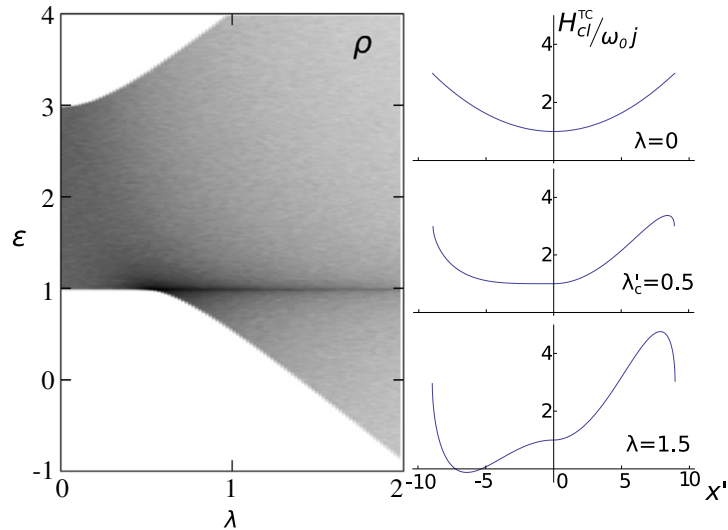


Fig. 8. Semiclassical level density in the $M = 2j$ subspace of the $j = N/2$ Tavis–Cummings model ($\delta = 0$) with $\omega = 2$, $\omega_0 = 1$ as a function of λ and $\varepsilon \equiv E/\omega_0j$ (shade plot on the left, with dark areas indicating larger values and vice versa) and three dependences of the corresponding Hamiltonian function (13) on x' for $p' = 0$ (on the right). An ε QPT due to an inflection point of the classical Hamiltonian above the QPT critical point (32) results in a logarithmic divergence of the semiclassical level density (the dark band in the shade plot), cf. Fig. 4(b).

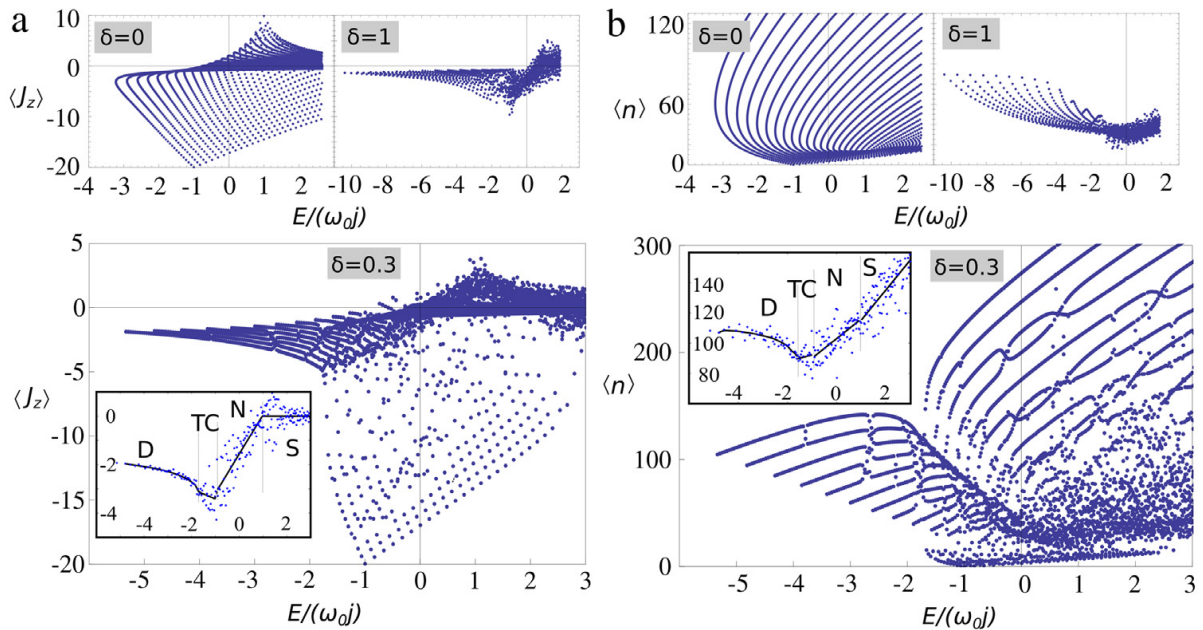


Fig. 9. Peres lattices of quantum expectation values of observables J_z (panel a) and n (panel b) in individual eigenstates of the $j = N/2$ Hamiltonian (1) for $N = 40$, $\omega = \omega_0 = 1$, $\lambda = 2.5$. The upper panels depict lattices for the limiting values of $\delta = 0$ and 1, whereas the lower panels correspond to $\delta = 0.3$. The insets of the $\delta = 0.3$ panels show smoothed dependences of both observables on energy (averages over 20 neighboring eigenstates and their piecewise fits in various quantum phases).

– in agreement with the original conjecture [44] – an overall correlation of orderly arranged lattice domains with more regular regions of classical dynamics and vice versa.

The $\delta = 0.3$ Peres lattices in the main panels of Fig. 9 cross all four quantum phases of the model. There exist apparent similarities between parts of both $\delta = 0.3$ lattices located in the TC and D phases, respectively, and the corresponding Tavis–Cummings and Dicke lattices displayed in the $\delta = 0$ and 1 upper panels. However, a more specific distinction of quantum phases results from an averaging of both lattices over the neighboring eigenstates, as shown in the insets of both lower panels of Fig. 9. Points in these *smoothed lattices* represent averages $\langle J_z \rangle_i$ and $\langle n \rangle_i$ of the respective expectation values $\langle J_z \rangle_i$ and $\langle n \rangle_i$ over 20 neighboring eigenstates. Smoothed dependences of the averaged quantities on

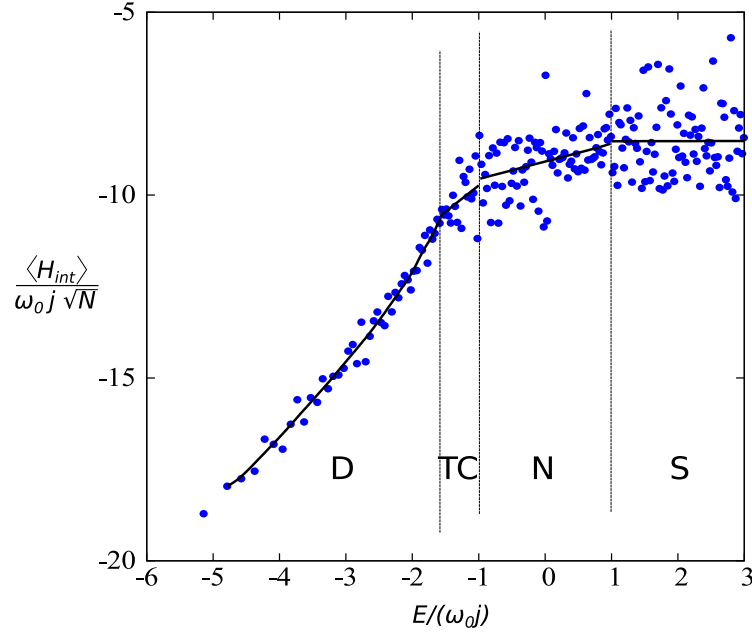


Fig. 10. Average slopes of the bunches of neighboring 20 levels for the $j = N/2$ Hamiltonian (1) with $N = 40$, $\omega = \omega_0 = 1$ and $\delta = 0.3$ at $\lambda = 2.5$. Quantum phases D, TC, N and S are distinguished by different smoothed energy dependences of the average slopes—see the piecewise fits indicated by full black lines.

energy are given by lines, resulting from piecewise fits within the four quantum phases. We observe that various quantum phases are recognized by different characters of the energy dependences, namely: (i) the phase D by slowly descending dependences of both $\langle J_z \rangle_i$ and $\langle n \rangle_i$ averages, (ii) the phase TC by roughly constant dependences, (iii) the phase N by linearly increasing dependences, and (iv) the phase S by saturated $\langle J_z \rangle_i \approx 0$ and linearly increasing $\langle n \rangle_i$.

Peres lattices for both quantities J_z and n are connected with the lattice of the interaction Hamiltonian H_{int} through the energy conservation. Using the Hellmann–Feynman formula, $dE_i/d\lambda = \langle dH/d\lambda \rangle_i$, we derive the following relation for the slope of individual energy levels

$$\frac{dE_i}{d\lambda} = \frac{\langle H_{\text{int}} \rangle_i}{\sqrt{N}} = \frac{E_i - \omega_0 \langle J_z \rangle_i - \omega \langle n \rangle_i}{\lambda}. \quad (33)$$

The slopes averaged over bunches of neighboring 20 levels, as in the insets of Fig. 9, are presented in Fig. 10 for the same values of control parameters. Piecewise fits of the energy dependences in individual quantum phases are again indicated by lines. We see that any of the D, TC, N and S quantum phases is characterized by a specific, roughly invariant energy dependence of the averaged level slope $dE_i/d\lambda$ within the corresponding energy domain. Abrupt changes of the character of these dependences coincide with critical ESQPT energies. This is in accord with a general relation between the density and flow signatures of ESQPTs, namely with the fact that a typical ESQPT generates the same type of non-analyticity in the energy dependences of both quantities ρ_{c1} and $dE_i/d\lambda$ [26,28]. Indeed, the discontinuities of $\partial(dE_i/d\lambda)/\partial E$ at the critical energies E_{c2} and E_{c3} , as observed in Fig. 10, are consistent with the analogous behavior of the $\partial\rho_{c1}/\partial E$ (Fig. 7). On the other hand, the anticipated point of a singular growth of the level slope (logarithmic divergence of its energy derivative) at E_{c1} is smoothed out in the finite spectrum for a moderate system's size.

4. Atom–field and atom–atom entanglement

4.1. Measures of bipartite entanglement

We turn to the study of quantum entanglement properties of individual eigenstate of the model Hamiltonian and their links to the ESQPTs. Our analysis includes two types of bipartite entanglement:

(a) that between the bosonic field and the set of all atoms (atom–field entanglement), and (b) that between any pair of individual atoms (atom–atom entanglement). The entanglement of type (a) is an important ingredient of superradiance since the interaction term of the Hamiltonian (1) carries a direct coupling between the atomic and field subsystems. In contrast, the entanglement of type (b) appears only due to an indirect coupling of individual atoms via the bosonic field, so it may be expected to be just a “higher-order” effect. We start with a brief description of the measures used to quantify both types of entanglement.

In the following, the atom–field and atom–atom entanglement will be evaluated in individual eigenstates $|\psi_i\rangle \in \mathcal{H}_A^{j,l} \otimes \mathcal{H}_F$ of Hamiltonian (1). Some examples of the eigenstate wave functions were shown in Fig. 2. Since the wave-function arguments ϕ and x , respectively, correspond directly to the atomic and field coordinates, a compound state $|\psi\rangle$ is factorized with respect to the atom–field partitioning of the system if it has a product wave function $\psi(\phi, x) = \psi'_A(\phi)\psi''_F(x)$, where ψ'_A and ψ''_F are arbitrary atomic and field wave functions. The method to quantify a departure of a given pure state $|\psi\rangle$ from exact factorization, i.e., an amount of atom–field entanglement involved in $|\psi\rangle$, makes use of the *von Neumann entropy* corresponding to the reduced density operators ρ_A and ρ_F of the atomic and field subsystem, respectively [46]. These operators are obtained by partial tracing of the total density operator $\rho = |\psi\rangle\langle\psi|$ over the irrelevant part of the total Hilbert space, that is $\rho_A = \text{Tr}_F \rho$ (trace goes over \mathcal{H}_F) for the atomic subsystem and $\rho_F = \text{Tr}_A \rho$ (trace goes over $\mathcal{H}_A^{j,l}$) for the field subsystem. Von Neumann entropy of the pure compound state ρ is by definition zero, but entropies of both reduced density operators ρ_A and ρ_F satisfy: $S_A = S_F \geq 0$. The case $S_A = S_F = 0$ implies a separable compound state, while the case $S_A = S_F > 0$ indicates that the reduction of ρ to a single subsystem leads to a loss of information on mutual entanglement between subsystems. A maximally entangled state yields $S_A = S_F = \ln(2j+1)$, where $2j+1$ is a dimension of $\mathcal{H}_A^{j,l}$, the smaller of both subspaces. We therefore define a normalized atom–field entanglement entropy in a compound state $|\psi\rangle$ as

$$S(\psi) = -\frac{\text{Tr}[\rho_A \ln \rho_A]}{\ln(2j+1)} = -\frac{\text{Tr}[\rho_F \ln \rho_F]}{\ln(2j+1)}. \quad (34)$$

It changes between $S = 0$ for separable states and $S = 1$ for maximally entangled states.

Quantifying the atom–atom entanglement, i.e., quantum correlations between a randomly chosen pair $\{k, l\}$ of atoms, is a more complex problem. The use of the above entropic approach is disabled by the fact that for any state $|\psi\rangle$ of the whole atom–field system, an arbitrary pair of atoms generically occurs in a *mixed* quantum state. It is known that mutual entanglement of a pair of objects in a mixed compound state cannot be recognized by a non-zero entropy of the reduced density operators [47]. Indeed, a mixed compound state of the pair generates mixed reduced states of the objects even in absence of entanglement. In such cases, the evaluation of an entropy-based measure of entanglement (so-called entanglement of formation) has to be performed with respect to all possible decompositions of the compound density operator into statistical mixtures of pure states [48], which is from the computational viewpoint a difficult task [49].

A way to bypass this obstacle for two-qubit systems was proposed in Refs. [50,51] in terms of a quantity called *concurrence*. The idea was applied and further elaborated [29–31,52,53] for multi-qubit systems in fully symmetric states, like our ensemble of N two-level atoms with $j = N/2$. The atom–atom entanglement in this case is characterized by a scaled concurrence

$$C(\psi) = (N-1) \max \left\{ \sqrt{\lambda_1} - \sqrt{\lambda_2} - \sqrt{\lambda_3} - \sqrt{\lambda_4}, 0 \right\}, \quad (35)$$

where $\lambda_1 \geq \lambda_2 \geq \lambda_3 \geq \lambda_4$ are eigenvalues (real and non-negative) of a non-Hermitian matrix $\rho_A^{kl} \tilde{\rho}_A^{kl}$, with ρ_A^{kl} denoting a reduced density matrix of the pair of atoms $\{k, l\}$ and $\tilde{\rho}_A^{kl} \equiv (\sigma_y^k \otimes \sigma_y^l) \rho_A^{kl*} (\sigma_y^k \otimes \sigma_y^l)$ the corresponding “spin-flipped” (conjugate under the time reversal) state (with \otimes denoting the tensor product of operators for the selected atoms and ρ_A^{kl*} a complex conjugated density matrix in the σ_z^k, σ_z^l eigenbasis). The argument ψ in the definition (35) again reminds the compound state $|\psi\rangle$ in which the concurrence is calculated. It has to be stressed that the full symmetry of $|\psi\rangle$ under the exchange of atoms, which is guaranteed in the $j = N/2$ subspace, ensures that the

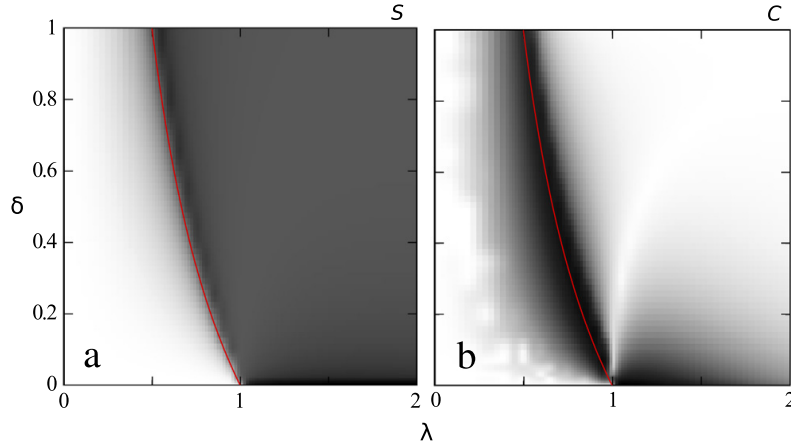


Fig. 11. (Color online) Entanglement properties of the ground state of the $j = N/2$ model in the plane of control parameters λ and δ (for $\omega = \omega_0 = 1$, $N = 40$). The red curve indicates the QPT critical coupling λ_c . Left: atom–field entanglement measured by the entropy (34). Right: atom–atom entanglement measured by the concurrence (35). The darker areas indicated larger entanglement.

reduced density matrix ρ_A^{kl} , as well as $\tilde{\rho}_A^{kl}$ and C , are the same for *any* pair of atoms, hence do not in fact depend on k, l .

Matrix elements of the reduced two-atom density matrix ρ_A^{kl} for any symmetric state of an N -qubit system can be expressed through expectation values $\langle J_z \rangle$, $\langle J_z^2 \rangle$ and $\langle J_+ \rangle$ of collective quasi-spin operators in a given state—see formulas (4) and (11) in Ref. [52]. This makes it possible to perform a straightforward numerical computation of C in the $j = N/2$ subspace of our model. Moreover, as shown in Ref. [53], the scaled concurrence in this subspace is related to the so-called Kitagawa–Ueda spin-squeezing parameter ξ^2 though the relation $C = \max\{1 - \xi^2, 0\}$, so it varies between $C = 0$ for separable states and $C = 1$ for the states that exhibit the maximal entanglement allowed for a given N . An entropy corresponding to the entanglement of formation of a single atomic pair reads as [51]

$$s(\psi) = - \sum_{\sigma=\pm} a_{\sigma} \ln a_{\sigma}, \quad a_{\pm} = \frac{1}{2} \left[1 \pm \sqrt{1 - \frac{C(\psi)^2}{(N-1)^2}} \right]. \quad (36)$$

For $C = 0$ we have $s = 0$, while for $C = 1$ we obtain $s \approx \ln 2 / (N - 1)^2 + \ln(N - 1) / 2(N - 1)^2$, which decreases from $s = \ln 2$ for $N = 2$ to zero in the classical limit $N \rightarrow \infty$. With $N \gg 1$, the maximal entropy behaves as $s \sim \ln N / N^2$. Note that the $N \gg 1$ maximal atom–field entanglement entropy *per atom* decreases as $S/N \sim \ln N / N$, see Eq. (34), so it exceeds the atom–atom entanglement entropy about N times. These scaling properties are verified theoretically and by large- N numerical calculations [32].

The atom–field and atom–atom entanglement properties have been studied for the ground state of the Dicke model [32,33,36]. As in other models of similar nature, see e.g. Refs. [29,30,34,35], the second-order QPT was shown to induce a singularity in both entanglement measures (34) and (35). Fig. 11 verifies this conclusion in our extended model with variable parameter δ . We observe that both S and C measures exhibit an increase at about the critical coupling λ_c from Eq. (27). For $\delta > 0$, the atom–atom entanglement drops back to nearly zero values with $\lambda > \lambda_c$. The atom–field entanglement saturates at a value $S \approx \ln 2 / \ln(N + 1)$ for $\lambda \gg \lambda_c$, which is due to an irreducible atom–field coupling in the lowest positive parity state in the strong coupling limit [32]. In the $\delta \approx 0$ region, close to the integrable Tavis–Cummings limit, both entanglement measures show roughly a step-like increase at λ_c . This is due to a specific mechanism, in which the ground state at each λ is formed via unavoided crossings of levels with different values of the conserved quantum number M , see Fig. 1(a). We will analyze the integrable case in more detail below.

4.2. Atom–field entanglement: the $\delta = 0$ case

In the following, we present results of a numerical study of the atom–field entanglement in individual eigenstates of Hamiltonian (1) with $j = N/2$. We start by analyzing the integrable

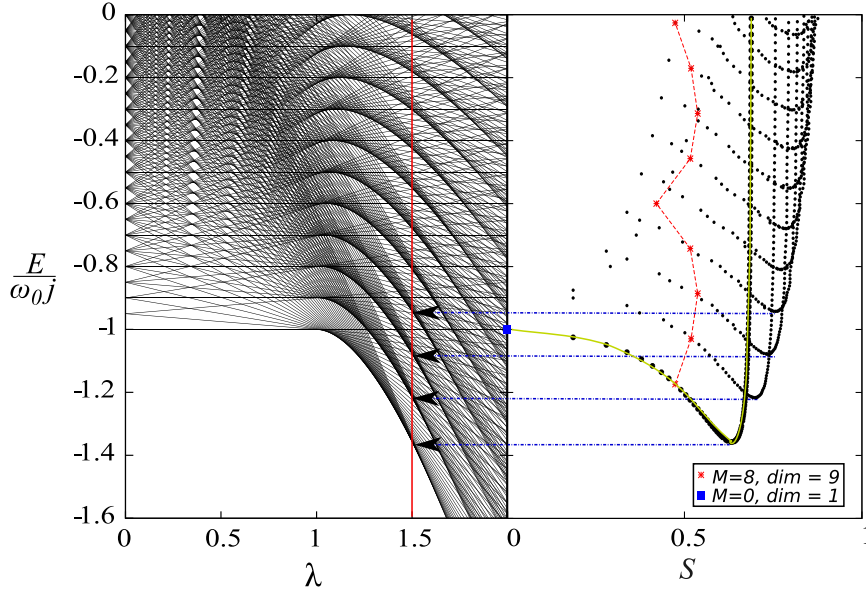


Fig. 12. (Color online) The full energy spectrum of the $\delta = 0$ model with $\omega = \omega_0 = 1$ for $j = N/2$ and $N = 40$ (left panel), and the atom–field entanglement entropies S in individual eigenstates corresponding to $\lambda = 1.5$ cut of the spectrum (right panel). The lowest V-shaped chain of points (connected by the green curve) in the entropic spectrum corresponds to the lowest states from various M -subspaces, the second chain to the second states, etc. The points corresponding to two selected M -subspaces ($M = 0$ and 8) are highlighted.

Tavis–Cummings limit $\delta = 0$. This simple setting will allow us to obtain some insight into the entanglement properties from quasi-analytic solutions, which will serve as a useful reference for the less trivial $\delta > 0$ case. We know that for $\delta = 0$ the Hilbert space splits into the subspaces \mathcal{H}_M with fixed values of quantum number M , see Eq. (4). The reduced density matrix of the atomic subsystem within each \mathcal{H}_M reads as

$$\begin{aligned} \rho_A &= \sum_{n=0}^M \sum_{m, m'=-j}^{\min\{M-j, j\}} \alpha_{mn_M(m)} \alpha_{m'n_M(m')}^* |m\rangle_A \langle n|n_M(m)\rangle_F \langle n_M(m')|n\rangle_F \langle m'|_A \\ &= \sum_{m=-j}^{\min\{M-j, j\}} |\alpha_{mn_M(m)}|^2 |m\rangle_A \langle m|_A, \end{aligned} \quad (37)$$

where $n_M(m) = M - j - m$ is a number of bosons associated with quasi-spin projection m for a given value of M . This expression implies that for $\delta = 0$ the entanglement entropy (34) of any eigenstate is equal to the *wave-function entropy* (11) corresponding to its expansion in the non-interacting basis.

Let us focus first on the *tuned* case $\omega = \omega_0$. The wave-function entropies for the $M = 2j$ spectrum of a tuned $\delta = 0$ Hamiltonian were shown in Fig. 4(a). We notice that the entropy of individual eigenstates does not change with λ and that it has an apparent symmetry with respect to the vertical reflection of the spectrum around the centroid energy $E(0)$. The former feature was explained by constancy of eigenstates of the simple Hamiltonian (10), the latter follows from a recursive relation for the eigenstate components which yields the same distributions $|\alpha_{mn}|^2$, hence the same entropies, for the pair of levels with opposite slopes.

The full spectrum of the Tavis–Cummings model is obtained by combining the spectra for all values of M . This is for $\omega = \omega_0$ seen in Fig. 12. It shows the energy spectrum as a function of λ (in the left panel) and the atom–field entanglement entropy of individual eigenstates for one particular value of the coupling strength (the right panel). The QPT critical coupling λ_c coincides with the point where the energy of the $M = 0$ ground state is crossed by the lower state from the $M = 1$ space. A further increase of λ above λ_c leads to a sequence of consecutive level crossings in which the lowest states from subspaces with increasing M become instantaneous ground states of the system. A similar mechanism applies also in the spectrum of excited states, where we observe a sequence of separated caustic structures formed by states with increasing ordinal numbers within each M -subspace (the

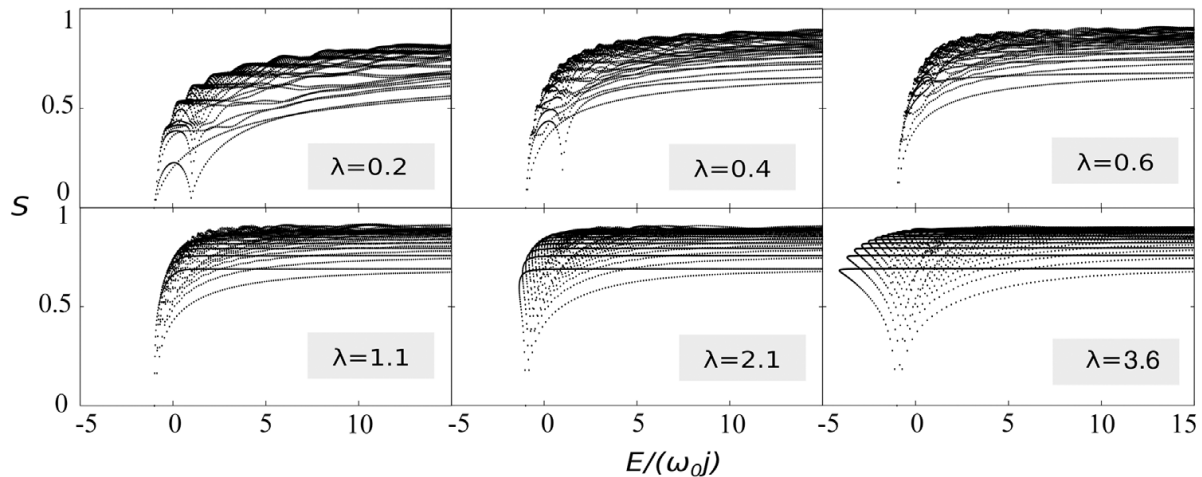


Fig. 13. The atom–field entanglement entropy of individual eigenstates of the $\delta = 0$ model with $j = N/2$ and $N = 40$ in the detuned case ($\omega = 2$, $\omega_0 = 1$) for several values of the coupling strength λ .

n th caustic structure in the vertical direction represents an envelope of lines corresponding to the n th states from individual M -subspaces).

The entropic spectrum on the right of Fig. 12 arises in a similar way. It is composed of several mutually shifted V-shaped chains of points, each of them containing a collection of states from different M -subspaces. For example, the lowest V-chain of points is formed by the lowest-energy states from all M -subspaces, the second lowest chain by second lowest-energy states and so on. To indicate a contribution of a single M -subspace to the entropic spectrum, we highlighted the points corresponding to two values of M . For $M > 0$, the contribution has a seagull-like form (see the $M = 8$ example in the figure), whose reflection symmetry around $E(0)$ results from the above-discussed properties of Eq. (10). The instantaneous ground state at the given $\lambda = 1.5$, which is well above the critical point λ_c , has a high value of M and therefore carries a considerable amount atom–field entanglement (as in general expected in superradiance). On the other hand, the trivial one-dimensional subspace with $M = 0$ formed by the state $|m = -j\rangle_A |n = 0\rangle_F$, which was the ground state of the $\delta = 0$ Hamiltonian at $\lambda < \lambda_c$ and becomes an excited state with energy $E = E_{c2} = -\omega_0 j$ for $\lambda > \lambda_c$, has apparently zero atom–field entanglement. We will see below that some remnants of this state remain present in entropic spectra also in the non-integrable $\delta > 0$ regime.

Let us consider now the *detuned* case $\omega \neq \omega_0$. The atom–field entropic spectra of a Hamiltonian with $\delta = 0$ and $\omega = 2\omega_0$ are displayed in Fig. 13 for increasing values of the coupling strength λ (the critical coupling is $\lambda_c = \sqrt{2}$). We know (see Section 2.2) that in the strong coupling limit, $\lambda \gg \lambda_c$, the detuned situation becomes very similar to the tuned one. This is obvious from a comparison of the $\lambda = 3.6$ entropic spectrum in Fig. 13 with that in Fig. 12. On the other hand, for small coupling strengths, $\lambda \lesssim \lambda_c$, the detuning $\Delta\omega$ plays an important role. A detuned system shows generally lower values of the atom–field entanglement than the tuned one, which can be attributed to a smaller perturbation efficiency of the interaction Hamiltonian due to larger energy gaps between the unperturbed (factorized) states, see Eq. (10).

It is clear that the factorized state $|m = -j\rangle_A |n = 0\rangle_F$ with $M = 0$ at critical energy $E_{c2} = -\omega_0 j$ is an invariant eigenstate of any $\delta = 0$ Hamiltonian, irrespective of ω , ω_0 and λ . So the $S = 0$ point at the place of the unperturbed ground state is present in all entropic spectra of Fig. 13. However, for an $\omega \neq \omega_0$ system, a local decrease (converging to $S = 0$ with $j, N \rightarrow \infty$) of the atom–field entanglement is present also at the highest critical energy $E_{c3} = +\omega_0 j$. This is due to quantum critical properties of the $M = 2j$ subspace discussed in Section 3.2. We consider here the $\omega > \omega_0$ case (see Fig. 4(b)), but the same phenomenon takes place also in the reversed detuning hierarchy $\omega < \omega_0$ (Fig. 4(c)). For $\lambda < \lambda'_c$, where λ'_c is the critical coupling (32), the lowest state of the $M = 2j$ subspace at energy E_{c3} keeps the factorized form $|m = +j\rangle_A |n = 0\rangle_F$ (mind the sign difference in m from the other factorized state, which means that now a maximal possible, for a given j , number of atoms is in the upper level). Distinct lowering of the atom–field entanglement entropy at $E = E_{c3}$ is observed in

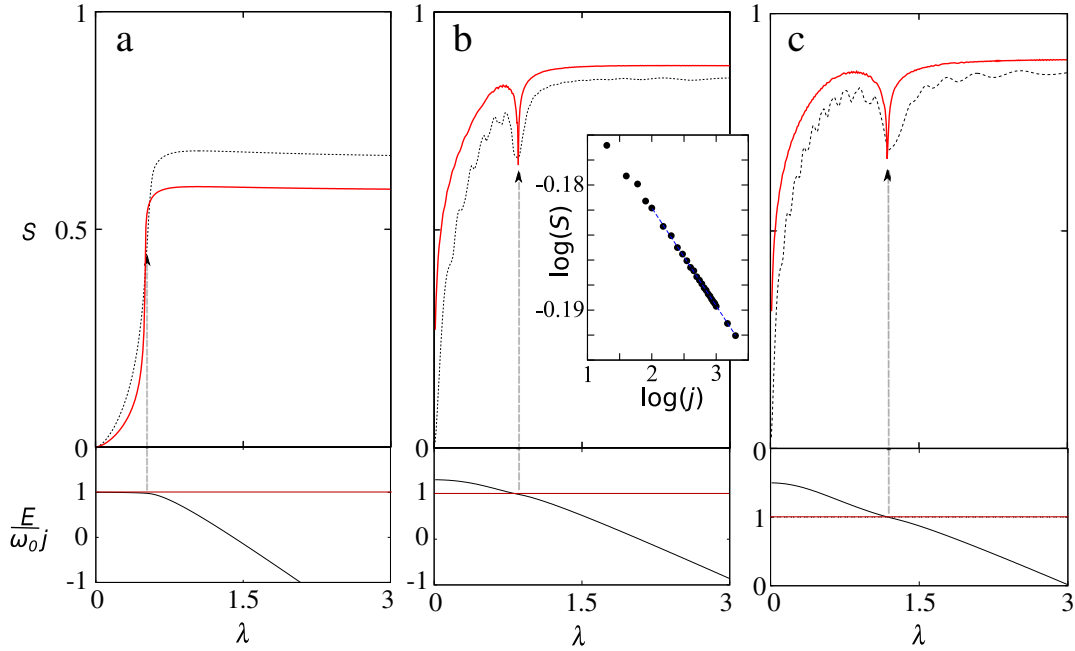


Fig. 14. The atom–field entanglement entropy for three states from the $M = 2j$ subspace of the $\delta = 0$ detuned ($\omega = 2$, $\omega_0 = 1$) model with $j = N/2$: the ground state (panel a) and excited states which at $\lambda = 0$ have 15% (panel b) and 24% (panel c) of the maximal excitation energy. The dashed curves are for $N = 40$, the full ones for $N = 1000$. The energy of the corresponding level (for $N = 40$) is shown at the bottom of each panel. The log–log plot in panel (b) inset shows the minimum value of S in the dip as a function of j for the level at 15% of the spectrum (for this level, the dependence is roughly $S_{\min} \propto 1/j^{0.008}$).

the $\lambda = 0.2$ and 0.4 panels of Fig. 13 (in which $\lambda'_c = 0.5$). This QPT-related effect becomes sharper with increasing j and N , and in the $j, N \rightarrow \infty$ limit it results in a similar $S = 0$ cusp as that at energy E_{c2} . For $\omega < \omega_0$, the above factorized state, causing the same effect, is the highest state of the $M = 2j$ subspace at $\lambda = 0$.

An analogous lowering of the atom–field entanglement entropy at the upper critical energy E_{c3} appears also for the coupling strengths *above* the QPT critical value λ'_c . The effect in this domain is caused by the $f = 1$ type of ESQPT in the $M = 2j$ subspace. Indeed, when excited states within this subspace cross the critical energy, they get temporarily localized in the coordinate region around the point $x' = 0$, i.e., at the position of the factorized state. This is due to “dwelling” of the $E = E_{c3}$ classical trajectory and a semiclassical wave function at an inflection point of the classical Hamiltonian (13). An analogous phenomenon was observed also in other quasi $f = 1$ models, see e.g. Ref. [54]. The lowering of the eigenstate entropy in the $E \approx E_{c3}$ domain was visible already in panels (b) and (c) of Fig. 4, but it is not apparent in Fig. 13. To see the effect in the pile up of all- M spectra, one would have to go to higher j, N values, when the localization becomes stronger and the entropy decreases to its lower limit $S = 0$.

The ESQPT-based localization effect is nevertheless well documented in Fig. 14, which depicts the evolution of the atom–field entanglement for three selected levels (ground state and two excited states) from the $M = 2j = N$ subspace for $N = 40$ and 1000 . We see that the passage of the selected excited states through the ESQPT energy E_{c3} is correlated with a local decrease of the entanglement entropy [sharp dips in the dependences in panels (b) and (c)]. As demonstrated by the curves for two values of N , the drop of entropy becomes sharper and deeper with increasing size of the system. The decrease of S at the lowest point of the dip with $j = N/2$ for one of the excited states is shown in the inset of Fig. 14(b). The depicted log–log plot indicates a very slow power-law decrease according to $S_{\min} \propto 1/N^a$. The exponent a is rather small and depends on the selected level (e.g., for the displayed level at 15% of the spectrum we obtain $a = 0.008$, while for the level at 20% we would have $a = 0.01$). Note that the entanglement entropy for excited states for large λ saturates at a value close to $S \approx \ln(0.482 d_{\max}) / \ln d_{\max}$, where $d_{\max} \equiv d(j, 2j) = 2j + 1$ is the dimension of the $M = 2j$ subspace. This expression follows from the use of the random matrix theory for estimating an average wave-function entropy for d_{\max} orthonormal states in the limit of strong mixing [42]. Note also that

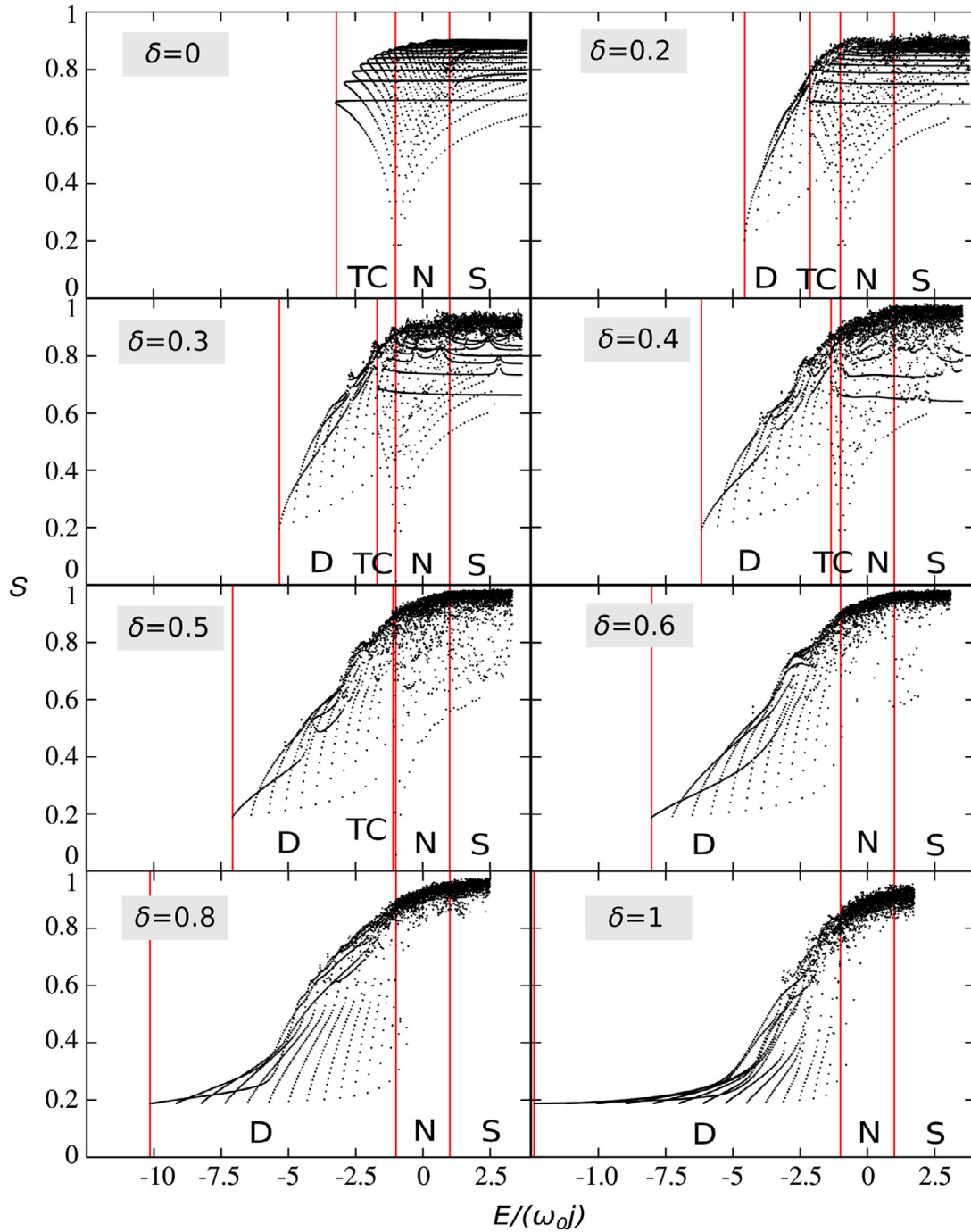


Fig. 15. Evolution of the $j = N/2$ entropic spectra of the atom–field entanglement with increasing parameter $\delta \in [0, 1]$ at $\lambda = 2.5$, $\omega = \omega_0$, $N = 40$. The ESQPT energies are indicated by vertical lines. The spectrum contains 5000 well converged eigenstates.

the critical coupling λ'_c of the ground-state QPT coincides with the sharpest increase of the ground-state entanglement entropy (Fig. 14(a)).

4.3. Atom–field entanglement: the $\delta > 0$ case

Now we are ready to turn our attention to the non-integrable $\delta > 0$ model. Fig. 15 shows the evolution of the entropic spectrum with parameter $\delta \in [0, 1]$ for $\omega = \omega_0$ and $\lambda = 2.5$, well above the critical coupling λ_c for any δ . The vertical lines demarcate the ESQPT energies, the zones between them corresponding to the D, TC, N and S quantum phases. One can see that the departure from integrability

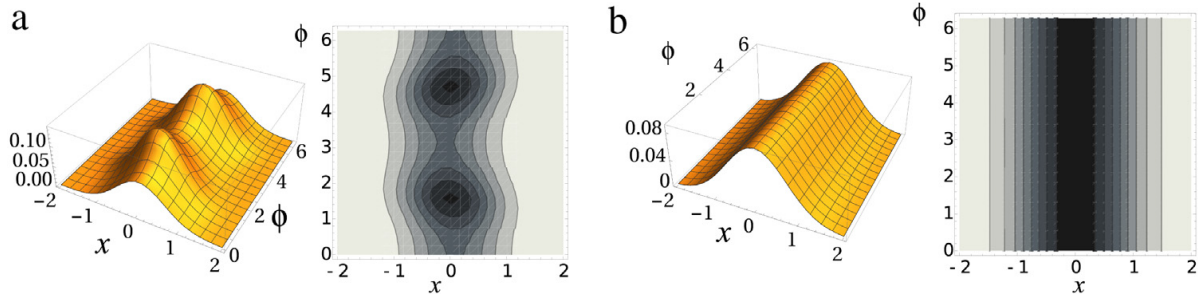


Fig. 16. (Color online) A detailed view of wave functions for (a) the eigenstate closest to the transition between the tc and n phases at $\lambda = 2.5$, $\delta = 0.3$ (cf. Fig. 2(e)) and (b) the factorized $E = E_{c2}$ eigenstate for $\delta = 0$. The other parameters are the same as in Fig. 15.

(an increase of δ) gradually destroys regular patterns in the entropic spectra, in analogy with Peres lattices. Orderly patterns in the entropic spectrum occur in the domains of regular dynamics, while disorderly scattered points indicate chaotic domains. Note that the accumulation of points in a narrow band close to (slightly below) the maximal entropy $S \approx 1$ for high energies is a consequence of ergodicity of chaotic dynamics [45]: a common eigenstate in the chaotic part of the spectrum contains virtually all atom–field configurations, whose dominant part is strongly entangled. On the other hand, the regular low-energy part of the entropic spectrum tends to a minimal value $S \approx \ln 2 / \ln(2j + 1)$, corresponding to states with a good parity quantum number [32].

An interesting aspect of the entropic spectra in Fig. 15 is the evolution of the atom–field entanglement in transition between the superradiant and normal phases at the critical energy $E = -\omega_0 j$. For $\delta > 0$, this energy corresponds to E_{c1} for $\lambda \in (\lambda_c, \lambda_0)$ and to E_{c2} for $\lambda \in (\lambda_0, \infty)$. We know that in the $\delta = 0$ limit, there always exists the fully factorized trivial eigenstate with $M = 0$ located right at this energy and a group of weakly entangled eigenstates with low values of M located nearby (see Figs. 12 and 13). To what extent do these structures survive an increase of parameter δ ? The answer can be read out from Fig. 15. We see that the eigenstates with lowered entropy and even a single state with $S \approx 0$ are preserved in the entropic spectra as far as the tc phase is present for the chosen value of the coupling strength λ . This is so if $\lambda > \lambda_0$, hence $\delta < 1 - \sqrt{N\omega\omega_0/2j\lambda^2}$, see Eq. (27). If $\lambda \in [\lambda_c, \lambda_0]$, that is for δ large enough to avoid the existence of the tc phase for a given λ , the decrease of entropy no longer takes place. These observations allow us to say that the occurrence of states with lowered atom–field entanglement entropy is a signature of the ESQPT between the n and tc phases, but not of that between the n and d phases.

The wave function corresponding to the $E \approx E_{c2}$ eigenstate with the lowest entanglement entropy for $\delta = 0.3$ can be seen in Fig. 2(e). Its detail is depicted in panel (a) of Fig. 16, in comparison with the fully factorized state with $M = 0$ shown in panel (b). Although the fine structures of the $\delta > 0$ wave function apparently prevent its full factorization (in contrast to the $\delta = 0$ case), a distant view shows a great deal of similarity to the $M = 0$ state.

Following our findings for $\delta = 0$, one might expect an analogous decrease of the atom–field entanglement entropy also at the critical energy E_{c3} (in transition between the s and n phases) in a detuned ($\omega \neq \omega_0$) system with $\delta > 0$. A numerical evidence of this phenomenon is however hindered by the above-presented (cf. the inset in Fig. 14(b)) slowness of the decrease of the entanglement entropy dip to zero. To see an effect in the $\delta > 0$ system, one would have to perform a truncated-space diagonalization of the Hamiltonian for a very large j , N values, which is computationally demanding.

4.4. Atom–atom entanglement

We turn now to a brief numerical analysis of the atom–atom entanglement, which is limited to the symmetric $j = N/2$ subspace of the atomic Hilbert space. As in the previous case, we focus at first on the integrable Tavis–Cummings model. The scaled concurrence (35) for individual eigenstates (the concurrence spectrum) of the tuned Hamiltonian with $\delta = 0$ and $\lambda > \lambda_c$ is plotted in Fig. 17. The highlighted points denote states belonging to selected M -subspaces. Like in the entropic spectrum (Fig. 12), the states corresponding the same M -subspace form a pattern which is always symmetric

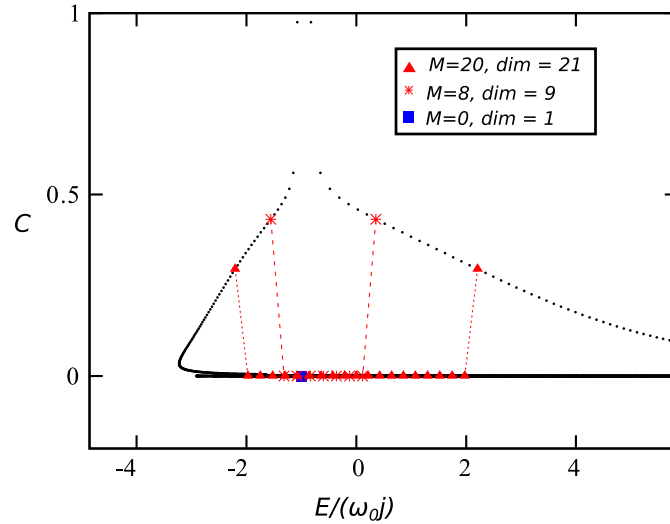


Fig. 17. (Color online) The scaled concurrence for the $\delta = 0$ model with $\omega = \omega_0 = 1$, $\lambda = 2.5$, $j = N/2$, $N = 40$. The contribution of selected M -subspaces (the U-shaped chains of points) is highlighted.

with respect to the reflection around the central energy $E(0)$. Trivially, the $M = 0$ state $|m = -j\rangle_A |n = 0\rangle_F$ has zero concurrence as the atomic state with minimal quasi-spin projection is fully factorized (all atoms in the lower level). So this state shows no entanglement in either atom–field or atom–atom sense. In contrast, some states with low values of M , which all have only weak (increasing with M) atom–field entanglement, show relatively large (decreasing with M) atom–atom entanglement.

Consider as an example a doublet of states with $M = 1$. The scaled concurrence for these states is $C = (N - 1)/N$, which changes between $C = 1/2$ for $N = 2$ and the maximal value $C = 1$ for $N \rightarrow \infty$ (see the upper pair of points in Fig. 17). As follows from Eq. (10), the $M = 1$ eigenstates are expressed by the superpositions $\propto |m = -j\rangle_A |n = 1\rangle_F \pm |m = -j + 1\rangle_A |n = 0\rangle_F$, whose first term is fully factorized in the atomic subspace (as in the $M = 0$ case) while the second term is maximally entangled (a symmetric state with one atom in the upper level and the rest of atoms in the lower level). It turns out that for increasing $M > 1$, only the states with the largest positive and negative slopes within the given M -subspace yield a non-vanishing atom–atom entanglement. These states form the “antennae” of the U-shaped dependences of C in each M -subspace. The scaled concurrence of these states decreases with M , forming together the left and right chains of $C > 0$ points in Fig. 17. The rest of the $\delta = 0$ eigenstates has $C = 0$.

Fig. 18 shows an evolution of the concurrence spectrum with increasing δ for a fixed $\lambda > \lambda_c$. Apparently, an overall trend of the atom–atom entanglement in individual eigenstates is a decrease with increasing δ . We stress that the concurrence of an absolute majority of states for any δ is zero (the spectrum contains 5000 states) and both the number of states with $C > 0$ and the values of C in these states further decrease with δ . The only states in which the atom–atom entanglement remains significant even for a relatively large values of δ appear in a narrow energy interval around the ESQPT critical energy E_{c2} demarcating the transition between the τ c and τ n phases. These states partly coincide with those in which we previously observed a reduced atom–field entanglement, see Fig. 15. For δ large enough to avoid the existence of the τ c phase, the atom–atom entanglement of all states vanishes.

The states around the critical energy E_{c2} with anomalous atom–field and atom–atom entanglement properties form only a small subset of all states, their appearance is nevertheless surprising. To make this clear, let us look at these states from a slightly different perspective. So far we have fixed a sufficiently large value of λ and changed δ , but now let us do it the other way round. If δ is fixed at a finite value and λ increases from 0 above λ_c and λ_0 , the states with anomalous entanglement first (not later than at λ_c) disappear from the spectrum, but above the critical coupling (somewhere in the $\lambda \sim \lambda_0$ region) some of them reappear again! In fact, a systematic analysis of the spectrum discloses *approximate revivals* of a number of weak-coupling ($\lambda \lesssim \lambda_c$) eigenstates (not only those

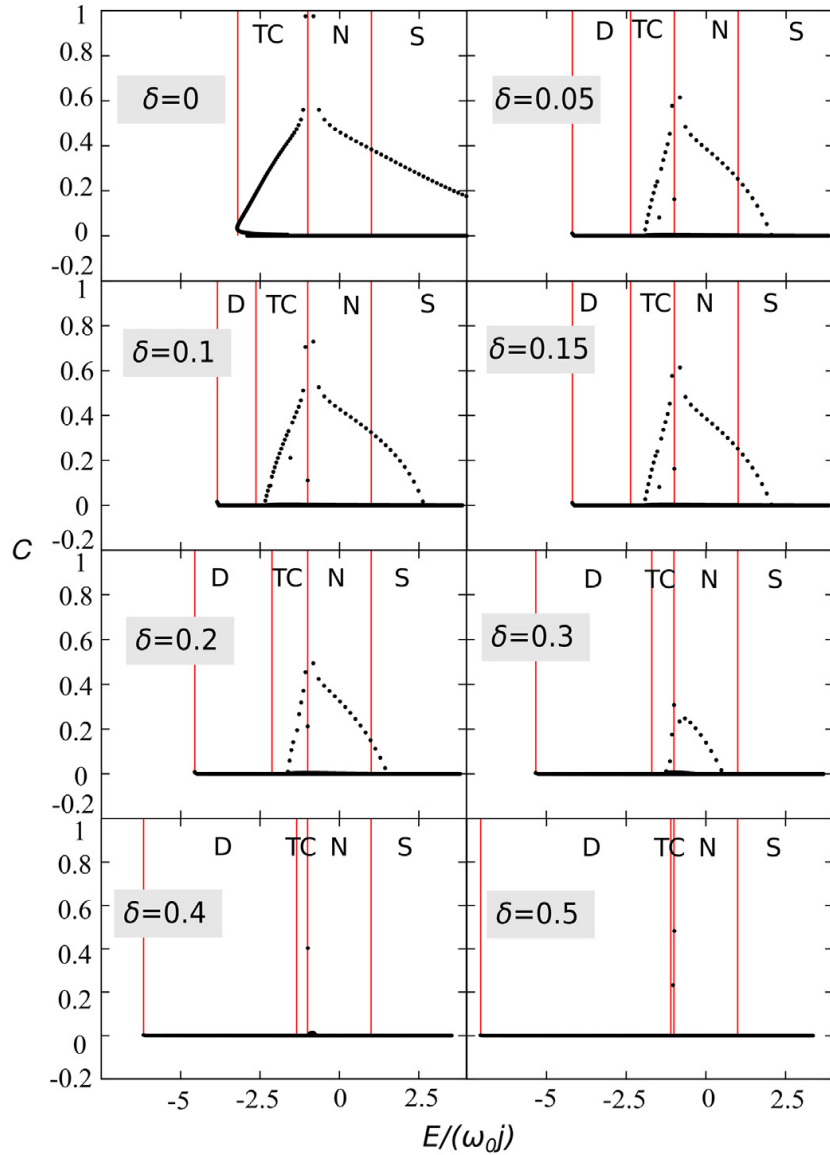


Fig. 18. An evolution of the atom–atom entanglement with increasing value of parameter δ for $\lambda = 2.5, \omega = \omega_0 = 1, j = N/2, N = 40$. The concurrence spectra contain 5000 well converged states.

with anomalous entanglement) in the strong-coupling ($\lambda \gtrsim \lambda_0$) regime. This is illustrated in Fig. 19 where we again show spectra of the tuned model with $j = N/2$ for two values of δ . The fullness (shade of gray) of each level encodes the number of principal components

$$v_i = \frac{1}{\sum_{i'} |\langle \psi_{i'}(0_+) | \psi_i(\lambda) \rangle|^4} \tag{38}$$

of the corresponding Hamiltonian eigenstate $|\psi_i(\lambda)\rangle$ in the basis of Hamiltonian eigenstates $|\psi_{i'}(0_+)\rangle$ taken at $\lambda = 0 + d\lambda \equiv 0_+$ infinitesimally displaced from the degeneracy point $\lambda = 0$ (this basis is therefore different from the $|m\rangle_A |n\rangle_B$ basis used above in the evaluation of the wave-function entropy). The number of principal components varies from $v_i = 1$ for a perfectly localized state (identical with one of the $\lambda = 0_+$ eigenstates) to $v_i \rightarrow \dim \mathcal{H} = \infty$ for totally delocalized states. The revival of several $\lambda = 0_+$ eigenstates is seen in Fig. 19 as reappearance of certain dark lines in the spectrum for large λ in the tc and n phases. The mechanism underlying this phenomenon is unknown.

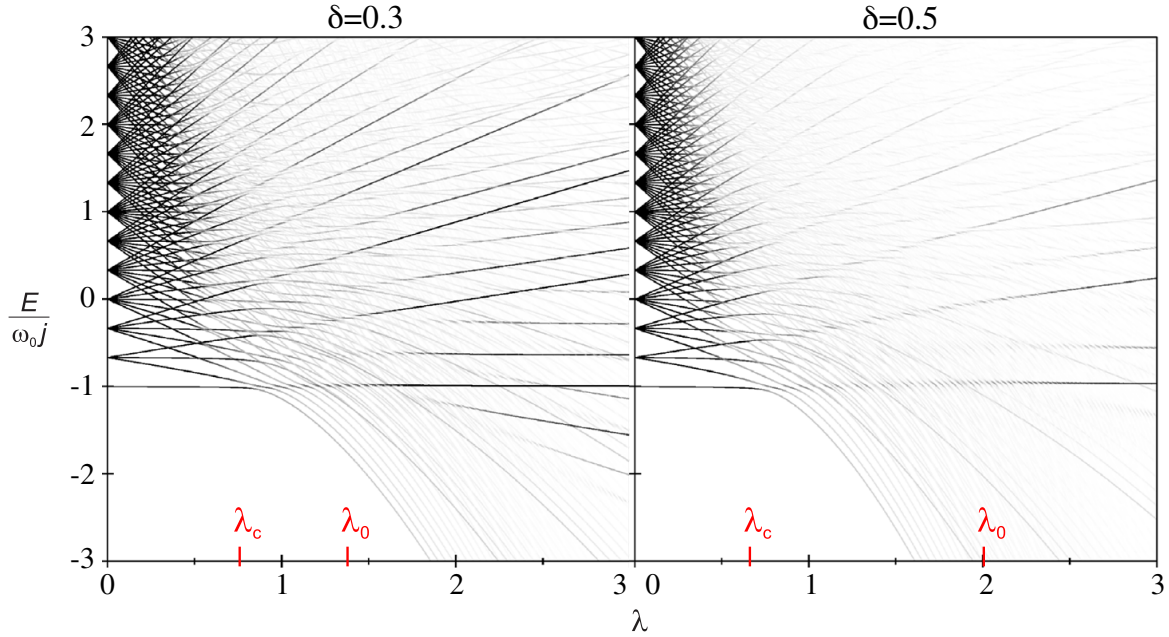


Fig. 19. Spectra of even-parity states of the tuned $j = N/2$ model with $N = 12$ for two values of δ . The number of principal components of an actual eigenstate in the unperturbed basis is encoded in the shades of gray of the respective line (black means perfect localization, $\nu_i = 1$, white complete delocalization, $\nu_i \rightarrow \infty$). Revival of some $\lambda < \lambda_c$ eigenstates at $\lambda \sim \lambda_0$ is seen in both spectra.

5. Conclusions

We have analyzed properties of a generalized Dicke model of single-mode superradiance allowing for a continuous (governed by parameter δ) crossover between integrable Tavis–Cummings and partly chaotic Dicke limits. We have considered three versions of the model, differing by constraints on the Hilbert space $\mathcal{H} = \mathcal{H}_A \otimes \mathcal{H}_F$. In particular: (i) the all- j model with the entire atomic space \mathcal{H}_A and $f = N + 1$ classical degrees of freedom, (ii) a single- j model with a single quasispin subspace $\mathcal{H}_A^{j,1} \subset \mathcal{H}_A$ and $f = 2$, and (iii) a single- j , M model taken for $\delta = 0$ in a subspace $\mathcal{H}_M \subset \mathcal{H}_A^{j,1} \otimes \mathcal{H}_F$; in this case $f = 1$.

Our first aim was to determine all types of thermal and quantum phase transitions and to characterize various phases of the atom–field system for intermediate values of δ . We have shown that the thermal phase diagram of the all- j model exhibits a coexistence of the TC and D types of superradiant phase (with and without saddles in the free energy landscape), which contract to a single type TC or D in the limits $\delta = 0$ or 1, respectively. The quantum phase diagram of a single- j model contains the superradiant QPT and three types of ESQPTs, characterized by singularities (jumps and a logarithmic divergence) in the first derivative of the semiclassical level density as a function of energy. The quantum phase diagram of a critical single- j , M model with $M = 2j$ shows for $\omega > \omega_0$ another second-order QPT and for $\omega \neq \omega_0$ also another ESQPT. The latter is characterized by a singularity (logarithmic divergence) directly in the level density in the $M = 2j$ subspace.

We have associated four spectral domains in between the ESQPT critical borderlines of the single- j model with the TC, D, N and S quantum phases of the model. These phases are characterized by different shapes of a smoothed energy dependence of some expectation values, which show abrupt changes at the ESQPT energies. A natural choice of the phase-defining quantity is the interaction Hamiltonian, whose expectation value $\langle H_{\text{int}} \rangle_i$ determines the slope $dE_i/d\lambda$ of the given level. According to the density–flow relation of the ESQPT signatures [28], a smoothed level slope should exhibit the same type of non-analyticity as the semiclassical level density.

Our second aim was to analyze atom–field and atom–atom entanglement properties of the model in a wide excited domain. This was first done in the integrable single- j , M model, which allowed for a qualitative explanation of results, and then numerically in the single- j model with $j = N/2$. We have found that an absolute majority of eigenstates in the spectrum for any choice of model parameters has

large atom–field entanglement but vanishing atom–atom entanglement. Exceptional in this sense for $\delta = 0$ are the eigenstates with low values of M , which yield a weak atom–field entanglement and simultaneously an increased atom–atom entanglement. We showed that remnants of these states exist relatively far in the non-integrable regime with $\delta > 0$. This concerns in particular the state with $M = 0$ located at the ESQPT energy E_{c2} , which has zero atom–field entanglement. Another state with reduced atom–field entanglement entropy, originating in the critical $M = 2j$ subspace, appears at the ESQPT energy E_{c3} for $\omega \neq \omega_0$.

Although the above-discussed states with anomalous entanglement properties have been located near the ESQPT critical borderlines, we do not regard this connection as systematic. The ESQPT singularity in the spectrum has strong consequences on the structure of eigenvectors – hence possibly also on their entanglement properties – in the $f = 1$ case, as indeed observed in the $M = 2j$ subspace of the present model. However, for $f > 1$ it does not seem likely that the entanglement plays a substantial role in a generic ESQPT since transitions between quantum phases affect (as we have seen) the trends of eigenstate variations rather than the eigenstates themselves. Nevertheless, it should be stressed that robust, systematic studies of entanglement in excited states are still rather scarce. We hope that results of our analysis will initiate similar studies in other relevant systems.

Acknowledgments

We acknowledge discussions with T. Brandes, N. Lambert, J. Hirsch and M.A. Bastarrachea-Magnani, and support of the Czech Science Foundation, project no. P203-13-07117S.

References

- [1] R.H. Dicke, *Phys. Rev.* 93 (1954) 99.
- [2] M. Gross, S. Haroche, *Phys. Rep.* 93 (1982) 301.
- [3] M.G. Benedict (Ed.), *Super-Radiance: Multiatomic Coherent Emission*, Taylor & Francis, New York, 1996.
- [4] T. Brandes, *Phys. Rep.* 408 (2005) 315.
- [5] J.D. Bekenstein, M. Schiffer, *Phys. Rev. D* 58 (1998) 064014.
- [6] N. Auerbach, V. Zelevinsky, *Rev. Prog. Phys.* 74 (2011) 106301.
- [7] E.T. Jaynes, F.W. Cummings, *Proc. IEEE* 51 (1963) 89.
- [8] M. Tavis, F.W. Cummings, *Phys. Rev.* 170 (1968) 379; 188 (1969) 692.
- [9] Y.K. Wang, F.T. Hioe, *Phys. Rev. A* 7 (1973) 831.
- [10] K. Hepp, E.H. Lieb, *Phys. Rev. A* 8 (1973) 2517.
- [11] K. Hepp, E.H. Lieb, *Ann. Phys. (NY)* 76 (1973) 360.
- [12] K. Rzażewski, K. Wodkiewicz, W. Zakowicz, *Phys. Rev. Lett.* 35 (1975) 432.
- [13] C. Emary, T. Brandes, *Phys. Rev. Lett.* 90 (2003) 044101.
- [14] C. Emary, T. Brandes, *Phys. Rev. E* 67 (2003) 066203.
- [15] J. Vidal, S. Dusuel, *Europhys. Lett.* 74 (2006) 817.
- [16] F. Dimer, B. Estienne, A.S. Parkins, H.J. Carmichael, *Phys. Rev. A* 75 (2007) 013804.
- [17] K. Baumann, C. Guerlin, F. Brennecke, T. Esslinger, *Nature* 464 (2010) 1301.
- [18] K. Baumann, R. Mottl, F. Brennecke, T. Esslinger, *Phys. Rev. Lett.* 107 (2011) 140402.
- [19] P. Pérez-Fernández, P. Cejnar, J.M. Arias, J. Dukelsky, J.E. García-Ramos, A. Relaño, *Phys. Rev. A* 83 (2011) 033802.
- [20] P. Pérez-Fernández, A. Relaño, J.M. Arias, P. Cejnar, J. Dukelsky, J.E. García-Ramos, *Phys. Rev. E* 83 (2011) 046208.
- [21] T. Brandes, *Phys. Rev. E* 88 (2013) 032133.
- [22] M.A. Bastarrachea-Magnani, S. Lerma-Hernández, J.G. Hirsch, *Phys. Rev. A* 89 (2014) 032101; 032102.
- [23] P. Cejnar, M. Macek, S. Heinze, J. Jolie, J. Dobeš, *J. Phys. A* 39 (2006) L515.
- [24] M.A. Caprio, P. Cejnar, F. Iachello, *Ann. Phys. (NY)* 323 (2008) 1106.
- [25] P. Cejnar, P. Stránský, *Phys. Rev. E* 78 (2008) 031130.
- [26] P. Stránský, M. Macek, P. Cejnar, *Ann. Phys.* 345 (2014) 73.
- [27] P. Stránský, M. Macek, A. Leviatan, P. Cejnar, *Ann. Phys.* 356 (2015) 57.
- [28] P. Stránský, P. Cejnar, *Phys. Lett. A* 380 (2016) 2637.
- [29] A. Osterloh, L. Amico, G. Falci, R. Fazio, *Nature* 416 (2002) 608.
- [30] J. Vidal, G. Palacsis, R. Mosseri, *Phys. Rev. A* 69 (2004) 022107.
- [31] J. Vidal, R. Mosseri, J. Dukelsky, *Phys. Rev. A* 69 (2004) 054101.
- [32] N. Lambert, C. Emary, T. Brandes, *Phys. Rev. Lett.* 92 (2004) 073602.
- [33] N. Lambert, C. Emary, T. Brandes, *Phys. Rev. A* 71 (2005) 053804.
- [34] T. Barthel, S. Dusuel, J. Vidal, *Phys. Rev. Lett.* 97 (2006) 220402.
- [35] J. Vidal, S. Dusuel, T. Barthel, *J. Stat. Mech.* 2007 (2007) P01015.
- [36] L. Bakemeier, A. Alvermann, H. Fehske, *Phys. Rev. A* 85 (2012) 043821.
- [37] L. Bakemeier, A. Alvermann, H. Fehske, *Phys. Rev. A* 88 (2013) 043835.
- [38] M.A. Bastarrachea-Magnani, B. López-del-Carpio, S. Lerma-Hernández, J.G. Hirsch, *Phys. Scr. A* 90 (2015) 068015.

- [39] M.A. Bastarrachea-Magnani, B. López-del-Carpio, J. Chávez-Carlos, S. Lerma-Hernández, J.G. Hirsch, *Phys. Rev. E* 93 (2016) 022215.
- [40] J. Chávez-Carlos, M.A. Bastarrachea-Magnani, S. Lerma-Hernández, J.G. Hirsch, *Phys. Rev. E* 94 (2016) 022209.
- [41] P. Cejnar, P. Stránský, *AIP Conf. Proc.* 1575 (2014) 23.
- [42] P. Cejnar, J. Jolie, *Phys. Rev. E* 58 (1998) 387.
- [43] M.A. Bastarrachea-Magnani, S. Lerma-Hernández, J.G. Hirsch, *J. Stat. Mech.* 2016 (2016) 093105.
- [44] A. Peres, *Phys. Rev. Lett.* 53 (1984) 1711.
- [45] P. Stránský, P. Hruška, P. Cejnar, *Phys. Rev. E* 79 (2009) 066201.
- [46] V. Vedral, *Rev. Modern Phys.* 74 (2002) 197.
- [47] A. Peres, *Phys. Rev. Lett.* 77 (1996) 1413.
- [48] C.H. Bennett, D. DiVincenzo, J. Smolin, W.K. Wootters, *Phys. Rev. A* 53 (1996) 3824.
- [49] Y. Huang, *New J. Phys.* 16 (2014) 033027.
- [50] S. Hill, W.K. Wootters, *Phys. Rev. Lett.* 78 (1997) 5022.
- [51] W.K. Wootters, *Phys. Rev. Lett.* 80 (1998) 2245.
- [52] X. Wang, K. Mølmer, *Eur. Phys. J. D* 18 (2002) 385.
- [53] X. Wang, B.C. Sanders, *Phys. Rev. A* 68 (2003) 012101.
- [54] S. Heinze, P. Cejnar, J. Jolie, M. Macek, *Phys. Rev. C* 73 (2006) 014306.

Reprint: Monodromy in Dicke superradiance

G.1 Main Achievements

- Focus-focus type of monodromy is identified in the integrable $\delta = 0$ version of the EDM.
- The decay of monodromy is observed using Peres lattices when smoothly breaking integrability by $\delta > 0$.
- The Classical trajectories passing through the monodromy point form an analog of the Dicke superradiance in a closed system.

Monodromy in Dicke superradiance

Michal Kloc, Pavel Stránský and Pavel Cejnar

Institute of Particle and Nuclear Physics, Faculty of Mathematics and Physics,
Charles University, V Holešovičkách 2, 18000 Prague, Czech Republic

E-mail: kloc@ipnp.troja.mff.cuni.cz

Received 23 February 2017, revised 18 May 2017

Accepted for publication 20 June 2017

Published 6 July 2017



CrossMark

Abstract

We study the focus–focus type of monodromy in an integrable version of the Dicke model. Classical orbits forming a pinched torus represent analogues of the dynamic superradiance under conditions of a closed system. Quantum signatures of monodromy appear in lattices of expectation values of various quantities in the Hamiltonian eigenstates and are related to an excited-state quantum phase transition. We demonstrate the breakdown of these structures with an increasing strength of non-integrable perturbation.

Keywords: monodromy, superradiance, extended Dicke model

(Some figures may appear in colour only in the online journal)

1. Introduction

Points of unstable equilibrium of integrable Hamiltonian systems create an obstacle to their fully analytical description [1, 2]. For instance, the single trajectory of a mathematical pendulum that crosses the stationary point of its upper vertical orientation separates two different types of motions in the phase space which are not analytically connectable. Similar, though more sophisticated singular trajectories are present also in integrable systems with a larger number of degrees of freedom f .

A clear example is a spherical pendulum (swings restricted to a spherical surface) with $f = 2$ [1]. This system is integrable as the component M of angular momentum along the vertical axis is an additional integral of motion besides energy E . After the transformation to action-angle variables, the bundle of $M = 0$ orbits crossing the stationary point on the north pole of the pendulum sphere with energy E equal precisely to the potential energy at that point forms a singular, so-called pinched torus, whose one elementary circle is contracted to a single point. If approaching the stationary point from two independent directions, the associate momenta linearly contract to zero—we speak about the focus–focus type of singularity [2–4].

The presence of a focus–focus singularity prevents introduction of global action-angle variables valid in the whole $f = 2$ phase space [1–5]. These variables can be defined on a local

level, but in a vicinity of the pinched torus they have some non-trivial topological features. These become apparent if all tori are imaged in the energy–momentum map (M, E) and if a two-dimensional basis of elementary cycles characterized by angles (ϕ_1, ϕ_2) is introduced on each torus. Consider a closed curve encircling the point corresponding to the pinched torus in the energy-momentum map. A loop along this curve takes us back to the same place, i.e. to the initial torus, but the basis of elementary cycles is altered—linearly transformed by a 2×2 matrix, which is fixed by the number of focus–focus singularities on the pinched torus inside the loop [1, 4]. This situation, when ‘once around’ does not mean the full return, is captured by the name monodromy [5].

Monodromy has also specifically quantum signatures [6, 7]. These can be derived from the application of the semiclassical quantization procedure to integrable systems with singular tori. It turns out that the joint spectrum (a lattice of energy versus momentum eigenvalues corresponding to individual Hamiltonian eigenstates) has a defect at the point associated with the pinched torus. Making a closed loop around this point, one observes a distortion of the lattice elementary cell such that the cell after the loop does not coincide with its initial form. The matrix describing the cell transformation is directly related to the classical monodromy matrix deduced from the elementary cycles on tori [7].

Effects of quantum monodromy have been identified experimentally in highly excited spectra of some molecules, like H_2O and CO_2 [8, 9]. More examples and an extensive list of references can be found in [10–13]. A link has been established between monodromy and so-called excited-state quantum phase transitions [14–16]. These are singularities in the density of energy eigenstates of arbitrary (integrable or non-integrable) systems with any (but preferably low) number of degrees of freedom generated by stationary points of the corresponding classical Hamiltonians [17, 18]. For non-degenerate stationary points, the form of the singularity with a given f can be deduced solely from the number of negative Hessian eigenvalues of the Hamiltonian at the stationary point [19].

In this article we investigate monodromy in an extended Dicke model of single-mode superradiance [20]. In particular, we show that the integrable version of the model in its classical limit contains a family of trajectories, which are analogous to the above-mentioned singular orbits of a spherical pendulum. We describe the defects that appear as a consequence of classical monodromy in quantum lattices of various observables evaluated in the Hamiltonian eigenstates and show a link to a specific excited-state quantum phase transition present in the model. In addition, we describe the fate of these singular structures after a gradual breakdown of the system’s integrability. Note that our work represents an extension of [21], where monodromy in the integrable Dicke model was first studied.

The plan of the paper is as follows: the model is described in section 2 and its integrable version in section 3. Properties related to classical and quantum monodromy are analyzed in section 4. Breakdown of monodromy under a non-integrable perturbation is studied in section 5. Brief conclusions are given in section 6.

2. Extended Dicke model

In 1954, Robert Dicke predicted an enhancement of spontaneous radiation from atomic or molecular samples caused by a coherent interaction of radiators with the radiation field [20]. This so-called superradiance can occur if the wavelength of the field is much longer than a typical distance between radiators in the sample. The phenomenon has two basic incarnations [22, 23]. (i) The *dynamic superradiance* [20], i.e. a strongly non-exponential, pulse-like decay of the excited sample governed by collective behavior of radiators [22–25]. This can happen in

the form of light emission into free space as well as in a cavity setup with only some discrete field modes present [26]. (ii) The *equilibrium superradiance* [27–29], i.e. the appearance of thermal and quantum phases characterized by a non-zero macroscopic density of radiation in the cavity [22, 23]. Closely related effects have been discussed in nuclear physics [30], solid-state physics [31] and other areas.

Various aspects of superradiance have been tested in laboratory. The dynamic superradiance as the free-space emission was observed in numerous setups since 1970s (see [24] and references therein). On the other hand, the observation of the equilibrium superradiance faced a problem of preparing a tunable system with strong atom-field coupling. A breakthrough was based on the theoretical proposal of [32], which led to recent experimental realizations of the superradiant phase transition using superfluid Bose gases in an optical cavity [33–35] and cavity-assisted Raman transitions [36]. These achievements triggered new theoretical efforts aiming at deeper understanding of the superradiance phenomena.

To illustrate the essence of superradiance, Dicke devised a simple model formulated in terms of a single-mode bosonic field interacting with a chain of two-level atoms, enumerated by $i = 1, \dots, N$ [20]. While the field quanta are created and annihilated by operators \hat{b}^\dagger and \hat{b} , the atoms are described by collective quasispin operators ($\hat{J}_- = \hat{J}_1 - i\hat{J}_2, \hat{J}_0 = \hat{J}_3, \hat{J}_+ = \hat{J}_1 + i\hat{J}_2$) composed as sums of Pauli matrices acting in the 2-dimensional Hilbert spaces of individual atoms: $\hat{J} = \sum_{i=1}^N \hat{\sigma}^{(i)}/2$. We use a slightly extended version of the Dicke Hamiltonian [37–40], which can be written in the following form:

$$\hat{H} = \omega \hat{b}^\dagger \hat{b} + \omega_0 \hat{J}_3 + \frac{\lambda}{\sqrt{N}} \left(\hat{b}^\dagger \hat{J}_- + \hat{b} \hat{J}_+ + \delta \hat{b}^\dagger \hat{J}_+ + \delta \hat{b} \hat{J}_- \right). \quad (1)$$

Here, ω represents a single-boson energy, ω_0 an energy difference between the levels of one atom, and λ an overall strength parameter of the atom-field interaction. We can assume $\lambda > 0$ as the $\lambda \mapsto -\lambda$ conversion is connected with a unitary transformation ($\hat{J}_1, \hat{J}_2, \hat{J}_3$) \mapsto ($-\hat{J}_1, -\hat{J}_2, \hat{J}_3$). The additional parameter $\delta \in [0, 1]$ is explained below.

Hamiltonian (1) can be used as a toy version of the cavity QED. (Note that the model neglects the term containing the square of the electromagnetic vector potential; for a recent discussion of its role see e.g. [41].) In a normal situation, the interaction is written as $\hat{H}_{\text{int}} \propto \hat{\mathbf{E}} \cdot \hat{\mathbf{D}} \propto (\hat{b}^\dagger + \hat{b})\hat{J}_1$, where $\hat{\mathbf{E}}$ is the electric intensity and $\hat{\mathbf{D}}$ the atomic dipole-moment matrix element, so $\delta = 1$. However, for $\lambda \ll \omega, \omega_0$, the terms $\hat{b}^\dagger \hat{J}_+$ and $\hat{b} \hat{J}_-$ give only small contributions to matrix elements and can be neglected [42, 43], so we can set $\delta = 0$. In this approximation, the model becomes integrable as it conserves the quantity

$$\underbrace{\hat{M}}_M = \underbrace{\hat{b}^\dagger \hat{b}}_n + \underbrace{\hat{J}_3 + j}_{n^*}, \quad (2)$$

which is the sum of the number of field bosons n and the number of atomic excitation quanta $n^* = m + j \leq N^* \equiv 2j$ (symbols under the braces in the above formula stand for eigenvalues of the associated operators and m is an eigenvalue of \hat{J}_3). This conservation law follows from a U(1) symmetry of the $\delta = 0$ Hamiltonian under the gauge transformation $\hat{b}^\dagger \mapsto e^{i\alpha} \hat{b}^\dagger, \hat{J} \mapsto \mathbf{R}(\alpha)\hat{J}$, where $\mathbf{R}(\alpha)$ is the rotation matrix by angle α around axis z . The $\delta \neq 0$ Hamiltonians do not conserve \hat{M} but only a parity $\hat{\Pi} = (-)^{\hat{M}}$ defining a residual discrete Z(2) symmetry of the system. Therefore, if the parameter δ is gradually increased, one goes from the integrable, hence entirely regular regime of dynamics at $\delta = 0$ (so-called Tavis–Cummings limit) to the non-integrable and partly chaotic regime at $\delta = 1$ (Dicke limit). Although the recent experimental realizations incorporated only the limiting regimes of the

model [33–36], intermediate values $\delta \in (0, 1)$ are in principle also achievable in the general experimental setup of [32], see [44].

An essential feature of Hamiltonian (1) resulting from the required coherence of the atom-field interaction is its strongly collective character, inscribed in the conservation of the squared quasispin \hat{J}^2 . This implies a crucial simplification of the analysis since it guarantees that the Hamiltonian acts independently in the subspaces with different \hat{J}^2 quantum numbers j . The number $N^* = 2j$, taking values from 0 or 1 (for N even or odd, respectively) to $N = 2j_{\max}$, can be considered as the number of *active* atoms as it measures the maximal excitation energy (in units of ω_0) that can be achieved within the whole atomic ensemble of size N ; the remaining $N - N^* = 2(j_{\max} - j)$ atoms form pairs mutually compensating their energies [45]. A $(2j + 1)$ -dimensional subspace with a given value j appears typically in many replicas differing by the permutation symmetry of its states with respect to the exchange of atoms. The sum of dimensions of all these subspaces exhausts the exponentially increasing dimension 2^N of the full Hilbert space of all atomic configurations. Only the subspace with the highest value $j = j_{\max}$, which contains fully symmetric atomic states, is unique.

The model has two degrees of freedom, $f = 2$: one is connected with the bosonic field, the other with the collective dynamics of atoms. The classical dynamics was studied by many authors using different techniques, see e.g. [21, 29, 38, 44, 46, 47]. The classical limit is achieved if $j \rightarrow \infty$, that is $N^* \rightarrow \infty$, which implies $j_{\max} \rightarrow \infty$ and $N \rightarrow \infty$. The result of the limiting process depends on the ratio

$$\gamma = \frac{j}{j_{\max}} = \frac{N^*}{N} \quad (3)$$

that can be fixed at a constant value $\gamma \in (0, 1]$. Identifying the model Planck constant \hbar with $(2j)^{-1} = (N^*)^{-1}$, one can obtain the classical description via the mapping

$$\frac{1}{\sqrt{N^*}} (\hat{b}, \hat{b}^\dagger) \mapsto \frac{1}{\sqrt{2}} (x + ip, x - ip), \quad (4)$$

$$\frac{1}{N^*} (\hat{J}_1, \hat{J}_2, \hat{J}_3) \mapsto \left(\sqrt{\frac{1}{4} - z^2} \cos \phi, \sqrt{\frac{1}{4} - z^2} \sin \phi, z \right), \quad (5)$$

where $x \in (-\infty, +\infty)$ and $p \in (-\infty, +\infty)$ are associated coordinate and momentum corresponding to the field degree of freedom, while $\phi \in [0, 2\pi)$ and $z \in [-\frac{1}{2}, +\frac{1}{2}]$ form the canonically conjugate coordinate-momentum pair for the atomic degree of freedom. The latter define coordinates (z the latitude projection and ϕ the longitude angle) on the Bloch sphere with radius $\frac{1}{2}$. The scaled Hamiltonian \hat{H}/N^* is then mapped to

$$\mathcal{H} = \omega \frac{x^2 + p^2}{2} + \omega_0 z + \underbrace{\sqrt{\gamma} \lambda}_{\lambda_\gamma} \sqrt{\frac{1}{2} - 2z^2} \left[(1 + \delta) x \cos \phi - (1 - \delta) p \sin \phi \right], \quad (6)$$

where $\lambda_\gamma \in (0, \lambda]$ is a rescaled interaction parameter, which is equal to λ for $\gamma = 1$. The scaled energy values corresponding to equation (6) are denoted as $\mathcal{E} = E/N^*$.

Equation (6) enables us to determine quantum critical properties of the atom-field system [37–40]. For λ_γ less than a certain critical value λ_c , the Hamiltonian has a single minimum at $x = p = 0$ and $z = -\frac{1}{2}$, implying zero numbers of both atom and field excitation quanta. At $\lambda_\gamma = \lambda_c$, the minimum starts moving to $x, p \neq 0$ and $z > -\frac{1}{2}$. This increases separate

excitation energies of atoms and field but lets the atom-field interaction reduce the overall ground state energy, which reads as follows:

$$\mathcal{E}_0 = \begin{cases} -\frac{\omega_0}{2} & \text{for } \lambda_\gamma < \lambda_c = \frac{\sqrt{\omega\omega_0}}{1+\delta}, \\ -\frac{\omega_0}{2} \frac{\lambda_\gamma^4 + \lambda_c^4}{2\lambda_\gamma^2 \lambda_c^2} & \text{for } \lambda_\gamma \geq \lambda_c. \end{cases} \quad (7)$$

For $\lambda_\gamma > \lambda_c$, the system at temperature T lower than a critical temperature $T_c = (\omega_0/2)\text{arctanh}^{-1}[\lambda_c/\lambda_\gamma]^2$ is in the superradiant phase [39, 40]. Moreover, the spectrum of the Hamiltonian eigenvalues with a given ratio γ splits into several non-thermal (quantum) phases separated by excited-state quantum phase transitions. The critical borderlines of quantum phases in the plane $\lambda_\gamma \times \mathcal{E}$ are characterized by distinct singularities in the first derivative of the semiclassical level density [37–40].

3. Classical analysis of the Tavis–Cummings limit

For $\delta = 0$, the classical Hamiltonian in equation (6) is integrable. The scaled integral of motion \hat{M}/N^* from equation (2) reads as

$$\mathcal{M} = \frac{x^2 + p^2 + 1}{2} + z. \quad (8)$$

Using the canonical transformation [40]

$$\begin{pmatrix} x \\ p \end{pmatrix} \mapsto \begin{pmatrix} x' \\ p' \end{pmatrix} = \begin{pmatrix} \cos \phi & -\sin \phi \\ \sin \phi & \cos \phi \end{pmatrix} \begin{pmatrix} x \\ p \end{pmatrix}, \quad (9)$$

$$\begin{pmatrix} z \\ \phi \end{pmatrix} \mapsto \begin{pmatrix} z' \\ \phi' \end{pmatrix} = \begin{pmatrix} \mathcal{M} - \frac{1}{2} \\ \phi + \mathcal{M} - \frac{1}{2} \end{pmatrix}, \quad (10)$$

the Tavis–Cummings Hamiltonian is converted to the form

$$\mathcal{H} = \omega_0 \mathcal{M} - \frac{\omega}{2} + \underbrace{(\omega - \omega_0)}_{\Delta\omega} \frac{x'^2 + p'^2 + 1}{2} + \lambda_\gamma x' \sqrt{\frac{1}{2} - 2 \left(\mathcal{M} - \frac{x'^2 + p'^2 + 1}{2} \right)^2}, \quad (11)$$

which does not depend on angle ϕ' . For any fixed value of the quantity \mathcal{M} , the formula (11) represents dynamics with $f = 1$ effective degree of freedom.

The classical dynamical equations for the transformed Hamiltonian (11) read as

$$\dot{x}' = \frac{\partial \mathcal{H}}{\partial p'} = +\Delta\omega p' + \lambda_\gamma \frac{2x'p'z_{\mathcal{M}}(r')}{\sqrt{\frac{1}{2} - 2z_{\mathcal{M}}^2(r')}}, \quad (12)$$

$$\dot{p}' = -\frac{\partial \mathcal{H}}{\partial x'} = -\Delta\omega x' - \lambda_\gamma \frac{\frac{1}{2} - 2z_{\mathcal{M}}^2(r') + 2x'^2 z_{\mathcal{M}}(r')}{\sqrt{\frac{1}{2} - 2z_{\mathcal{M}}^2(r')}}, \quad (13)$$

where dots stand for the time derivatives and $z_{\mathcal{M}}(r') = \mathcal{M} - (r'^2 + 1)/2$ with $r'^2 \equiv x'^2 + p'^2$ ($= r^2 \equiv x^2 + p^2$). A return back to the original phase space (x, p, ϕ, z) is possible via setting $z = z_{\mathcal{M}}(r')$, see equation (8), and performing an inverse of transformation (9), in which the angle ϕ is determined via an integration of the dynamical equation

$$\dot{\phi} = \dot{\phi}' = \frac{\partial \mathcal{H}}{\partial z'} = \omega_0 - \lambda_\gamma \frac{2x'z_{\mathcal{M}}(r')}{\sqrt{\frac{1}{2} - 2z_{\mathcal{M}}^2(r')}}. \quad (14)$$

Since the transformation (9) conserves radii, $r^2 = r'^2$, the integral of motion (8) enables one to easily determine for each point (x', p') the corresponding projection z on the atomic Bloch sphere. This implies a restriction on the available domain in the phase space in the form $r' \in [r'_{\min}, r'_{\max}]$, where

$$r'_{\min} = \begin{cases} 0 & \text{for } \mathcal{M} \leq 1, \\ \sqrt{2(\mathcal{M} - 1)} & \text{for } \mathcal{M} > 1, \end{cases} \quad r'_{\max} = \sqrt{2\mathcal{M}}. \quad (15)$$

The maximum radius r'_{\max} defines an outer circle of the available domain which corresponds to the maximum number of field bosons $n = M$ achieved when all atoms are in the lower state ($n^* = 0$, $z = -\frac{1}{2}$). Note that the transformation (9) is indeterminate at the outer circle as the angle ϕ is irrelevant in the south pole of the Bloch sphere.

The minimum radius r'_{\min} in equation (15) results from a minimum number of field bosons n needed to get a given value of M for a maximal atomic excitation $n^* = \text{Min}(M, N^*)$. For $M < N^*$ ($\mathcal{M} < 1$), the minimum number of bosons is zero and the corresponding point $(x', p') = (0, 0)$ is linked to the Bloch sphere latitude $z = \mathcal{M} - \frac{1}{2}$, which is less than $+\frac{1}{2}$. When $M = N^*$ ($\mathcal{M} = 1$), the $(0, 0)$ point gets associated exactly with the north pole $z = +\frac{1}{2}$. This particular configuration, which represents a state of maximally excited atoms and the field vacuum, will play an essential role in the following. Finally, if $M > N^*$ ($\mathcal{M} > 1$), the number of field bosons n cannot be less than $(M - N^*)$, so the minimal radius becomes larger than zero, defining an inner circle of the available (x', p') domain. The whole inner circle corresponds to the north pole of the Bloch sphere, where again the transformation (9) becomes undefined.

The contours $\mathcal{H} = \mathcal{E}$ of the Hamiltonian (11) in the available domain of the phase space are shown in figure 1 for a single interaction strength λ_γ and three values of the integral of motion: $\mathcal{M} < 1$, $\mathcal{M} = 1$, and $\mathcal{M} > 1$, see columns (a), (b), and (c) respectively. The upper row depicts the tuned case with $\Delta\omega = 0$, the lower row a detuned case with $\Delta\omega > 0$. Note that in this paper we assume the detuning hierarchy $\omega \geq \omega_0$, that is $\Delta\omega \geq 0$. Properties of the inverse hierarchy $\omega < \omega_0$ can be derived from the present ones by inverting the whole spectrum upside down, $\mathcal{H} \mapsto -\mathcal{H}$ (the ground state becomes the highest state and vice versa), and by applying a reflection transformation $(x', p') \mapsto -(x', p')$ in the phase space. This converts Hamiltonian (11) with $\Delta\omega < 0$ into the same form with $\Delta\omega > 0$, up to the constant term which changes its sign. So all the results discussed below are valid also for the inverse detuning hierarchy, except that the energies need to be suitably transformed.

The minimum of the transformed Hamiltonian function (11) determines the lowest energy eigenstate (in the $N^* \rightarrow \infty$ limit) in the selected M -subspace of the full Hilbert space (the ground state of the given subspace). Consider at first the $\mathcal{M} < 1$ and $\mathcal{M} > 1$ cases. These are both characterized by a gradual, smooth evolution of the minimum position and energy with the interaction strength. Indeed, it can be shown that as λ_γ increases from zero, the minimum moves along the line $p' = 0$, with x' decreasing below $-r'_{\min}$ (for $\Delta\omega \geq 0$) or increasing above $+r'_{\min}$ (for $\Delta\omega < 0$). The scaled energy descends from the initial value $\mathcal{E}'_0 = \omega_0(\mathcal{M} - \frac{1}{2}) + \Delta\omega r_{\min}^2/2$ taken at $\lambda_\gamma = 0$.

A more interesting scenario applies for $\mathcal{M} = 1$, that is $M = N^* = 2j$, when the evolution of the spectrum with λ_γ has a critical character [40, 48]. We note that the value $\mathcal{M} = 1$ demarcates the disc-to-annulus transition of the available phase-space domain and allows any partitioning of M between numbers $n, n^* \in \{0, \dots, N^*\}$. Let us first assume $\Delta\omega \geq 0$. In this

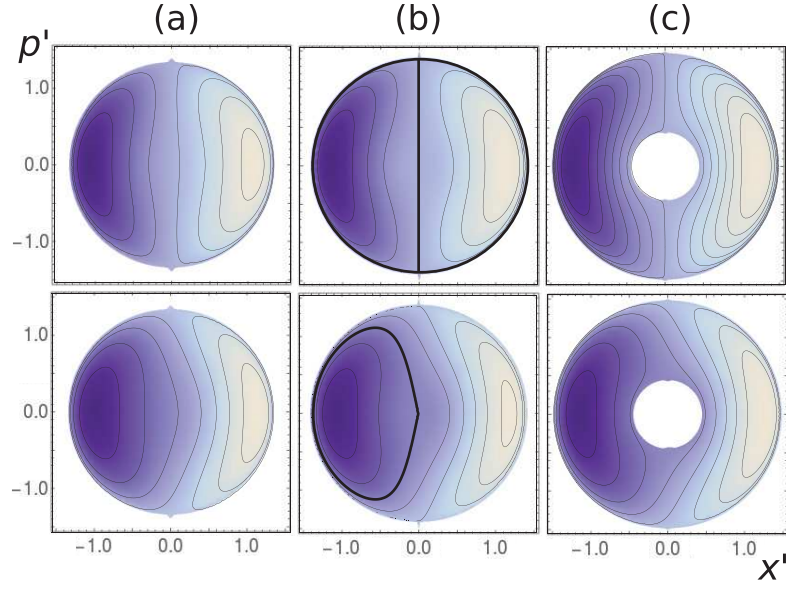


Figure 1. Contour plots of the Hamiltonian function (11) for $\lambda_\gamma = 2.5 > \lambda'_c$. Darker areas correspond to the lower values and vice versa. The upper row depicts the tuned case $\omega = \omega_0 = 1$, the lower row a detuned case $\omega = 2, \omega_0 = 1$, the columns correspond to (a) $M = 0.9$, (b) $M = 1$, and (c) $M = 1.1$. Critical contours passing the point $x' = p' = 0$ for $M = 1$ are marked by thick lines.

case, the minimum of the Hamiltonian (11) stays at $(x', p') = (0, 0)$ up to a certain critical value λ'_c of the interaction strength, but above this value it starts moving to $x' < 0$ along the $p' = 0$ line. The system undergoes a ground-state phase transition from a ‘non-radiant’ state corresponding to maximally excited atoms and no photon to a ‘radiant’ state with decreasing atomic and increasing field excitations. The lowest and highest energies \mathcal{E}'_0 and \mathcal{E}'_1 of the classical energy landscape are given by

$$\mathcal{E}'_0 = \begin{cases} \frac{\omega_0}{2} & \text{for } \lambda_\gamma \leq \lambda'_c = \frac{1}{2}|\Delta\omega|, \\ \frac{\omega_0}{2} + \Delta\omega s_- - 2\lambda_\gamma s_- \sqrt{1 - s_-} & \text{for } \lambda_\gamma > \lambda'_c, \end{cases} \quad (16)$$

$$\mathcal{E}'_1 = \frac{\omega_0}{2} + \Delta\omega s_+ + 2\lambda_\gamma s_+ \sqrt{1 - s_+},$$

$$s_\pm = \frac{2}{3} - \frac{2}{9} \frac{\lambda_c'^2}{\lambda_\gamma^2} \pm \frac{2}{9} \frac{\lambda_c'}{\lambda_\gamma} \sqrt{\frac{\lambda_c'^2}{\lambda_\gamma^2} + 3}. \quad (17)$$

The lowest energy \mathcal{E}'_0 shows a discontinuity of its second derivative at $\lambda_\gamma = \lambda'_c$, indicating a second-order ground-state quantum phase transition in the $M = N^*$ subspace. Let us stress that the critical strength λ'_c and minimum energy \mathcal{E}'_0 defined in equation (16) are different from λ_c and \mathcal{E}_0 related to the global minimum among all M -subspaces, see equation (7). In particular, for $\omega_0 \leq \omega < (3 + \sqrt{8})\omega_0$ we see that $\lambda'_c < \lambda_c$, so the present transition can take place deeply in the weak coupling regime, well before the superradiant phase transition of the whole system. In contrast, the highest energy \mathcal{E}'_1 in equation (17) grows smoothly with λ_γ . For $\Delta\omega < 0$, the spectrum is inverted, $\mathcal{E} \rightarrow -\mathcal{E}$, and shifted up by ω_0 , so the non-analytic evolution affects on the contrary the highest-energy state, while the ground state evolves smoothly.

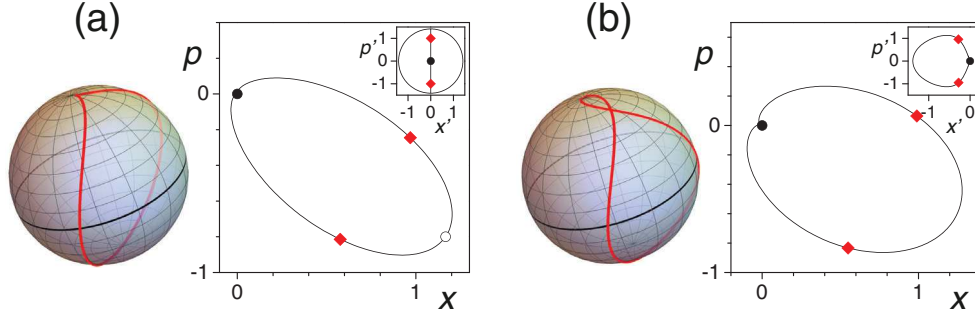


Figure 2. Classical orbits crossing the stationary point $(x', p') = (0, 0)$ of Hamiltonian (11) with $(\mathcal{M}, \mathcal{E}) = (1, \mathcal{E}'_c)$ in the (a) tuned and (b) detuned cases. The model parameters are as in figure 1. The orbits in (x', p') are depicted in the insets, the main panels show the associated motions on the atomic Bloch sphere (ϕ, z) and in the bosonic phase space (x, p) . Crossings of the north or south pole of the Bloch sphere are coordinated with passages through the full or open bullets in the bosonic space (the south pole is visited only in the tuned case), the equator transits correspond to the diamonds. Note that the asymptotic spiral motions around the north pole and $(x, p) = (0, 0)$ are under the resolution scale.

Regardless of the detuning hierarchy $\Delta\omega \geq 0$ or $\Delta\omega < 0$, the energy value

$$\mathcal{E}'_c = \frac{\omega_0}{2} \quad \text{for } \lambda_\gamma > \lambda'_c \quad (18)$$

demarcates a point of unstable equilibrium of the system—an inflection-like point of the energy landscape (11) present above the critical interaction strength λ'_c from equation (16). It implies an excited-state quantum phase transition in the $M = N^*$ subspace: at the critical energy (18) the semiclassical density of levels in this subspace shows a logarithmic divergence [40, 48]. This is an extreme form of spectral singularity resulting from the fact that the classical Hamiltonian (11) has just a single effective degree of freedom [19]. In contrast, the entire system with $f = 2$, governed by the Hamiltonian (6), exhibits at \mathcal{E}'_c a non-degenerate stationary point of \mathcal{H} with two positive and two negative Hessian eigenvalues, so the full energy spectrum of all- M levels shows a downward jump in the first derivative of the level density [19, 40]. Moreover, as we will see below, the point $(\mathcal{M}, \mathcal{E}) = (1, \mathcal{E}'_c)$ corresponds to a pinched torus of the focus–focus monodromy.

4. Classical and quantum monodromy

Figure 2 depicts two trajectories with $(\mathcal{M}, \mathcal{E}) = (1, \mathcal{E}'_c)$ in the original phase space (x, p, ϕ, z) , with the atomic variables represented on the Bloch sphere. Panels (a) and (b) show the tuned $\Delta\omega = 0$ and detuned $\Delta\omega > 0$ cases, respectively. If drawn in the transformed phase space (see the insets), both orbits coincide with the contours crossing the unstable stationary point $(x', p') = (0, 0)$, see the thick curves in figure 1(b). The motions along the curves in both atomic and bosonic parts of the phase space in figure 2 are correlated, so we mark the points on the (x, p) orbit that are on the (ϕ, z) orbit synchronized with the pole and equator crossings. We see that the detuned trajectory crosses only the north pole of the Bloch sphere, while the tuned one goes via both poles. Because the representation in terms of transformed variables (x', p') becomes invalid on the outer circle of the available domain, the whole outer segment of

the tuned trajectory in the inset of figure 2(a) is mapped to a single point in the original space (x, p) shown in the main image.

The north pole of the atomic Bloch sphere represents a special point of both $(\mathcal{M}, \mathcal{E}) = (1, \mathcal{E}'_c)$ orbits in figure 2 as its crossing requires *infinite time*. Time relations for these particular orbits can be most easily deduced in the tuned case, when $x' = 0$ (except the outer circle), so that equation (13) reduces to

$$\dot{p}' = -\sqrt{2} \lambda_\gamma \sqrt{\frac{1}{4} - z_{\mathcal{M}}^2(r')} = -\frac{\lambda_\gamma}{\sqrt{2}} \sqrt{p'^2(2 - p'^2)} \quad (19)$$

and equation (14) yields $\dot{\phi} = \omega_0$. We see that the momentum derivative vanishes for $p' = 0$ (the north pole, $z = +\frac{1}{2}$), but also for $p' = \pm\sqrt{2}$ (the south pole, $z = -\frac{1}{2}$). However, the latter ‘stationary’ points are false ones as they lie on the outer circle where the transformation (9) is indeterminate. It can be shown that the crossing of these points takes a finite time, in contrast to the real stationary point at $(x', p') = (0, 0)$. If $\boldsymbol{\rho} \equiv (\rho_1, \rho_2)$ denotes a projection of the (ϕ, z) point of the Bloch sphere onto the equator plane, the evolution close to the north pole is approximated by

$$\boldsymbol{\rho} \propto e^{\pm\lambda_\gamma t} (\cos \omega_0 t, \sin \omega_0 t), \quad (20)$$

where time t is counted so that $\boldsymbol{\rho} = (\rho_1, 0)$ at $t = 0$. Equation (20) defines a spiral winding in the inward or outward direction around the focus $\boldsymbol{\rho} = 0$. Note that a similar whirl appears also in the bosonic phase space around $(x, p) = (0, 0)$, but these structures are so tiny that they cannot be seen in figure 2. The detuned trajectory does not cross the south pole, so it avoids problems with the outer circle, but the time relations at the north pole are similar as in the tuned case.

The single critical trajectory shown in either panel (a) or (b) of figure 2 is not isolated. It belongs to the respective infinite bundle of orbits differing by angle $\phi_0 \in [0, 2\pi)$ at the initial point (e.g. at the equator of the Bloch sphere). The elementary cycles connected with varying ϕ shrink to a single point as the orbit approaches the north pole. We infer that the critical orbits in either $\Delta\omega > 0$ or $\Delta\omega = 0$ case form a pinched torus, so the system exhibits a focus–focus type of monodromy.

There is some similarity between the $(\mathcal{M}, \mathcal{E}) = (1, \mathcal{E}'_c)$ orbits in the present closed cavity system and the dynamic superradiance phenomenon in open systems [23, 26]. Indeed, the photon emission/absorption rate is given by

$$\dot{n} = N^* (x' \dot{x}' + p' \dot{p}'), \quad (21)$$

which in the tuned case can be directly evaluated from equation (19). The largest time derivative takes place at $p' = 1$, which corresponds to the equator of the atomic Bloch sphere ($z = 0$), and a similar conclusion, based on equations (12) and (13), is valid also in the detuned case. So the critical orbits describe a non-exponential decay of a fully excited atomic ensemble followed by complete re-absorption of emitted photons, a process which is infinitesimally slow when $(n, n^*) \approx (0, N^*)$, fast when $(n, n^*) \approx (N^*/2, N^*/2)$, and slow again when $(n, n^*) \approx (N^*, 0)$. This resembles the pulse-like decay process associated with dynamic superradiance, although equation (21) implies a strictly linear scaling of the irradiation peak with N^* , which is in contrast to the non-linear scaling valid for the free-space superradiance [24].

Let us investigate quantum signatures of monodromy. Figure 3 shows quantum energy-momentum maps [10–13], which are lattices of individual quantum energies E_k (where k stands for a principal quantum number simply enumerating energy eigenvalues) versus the

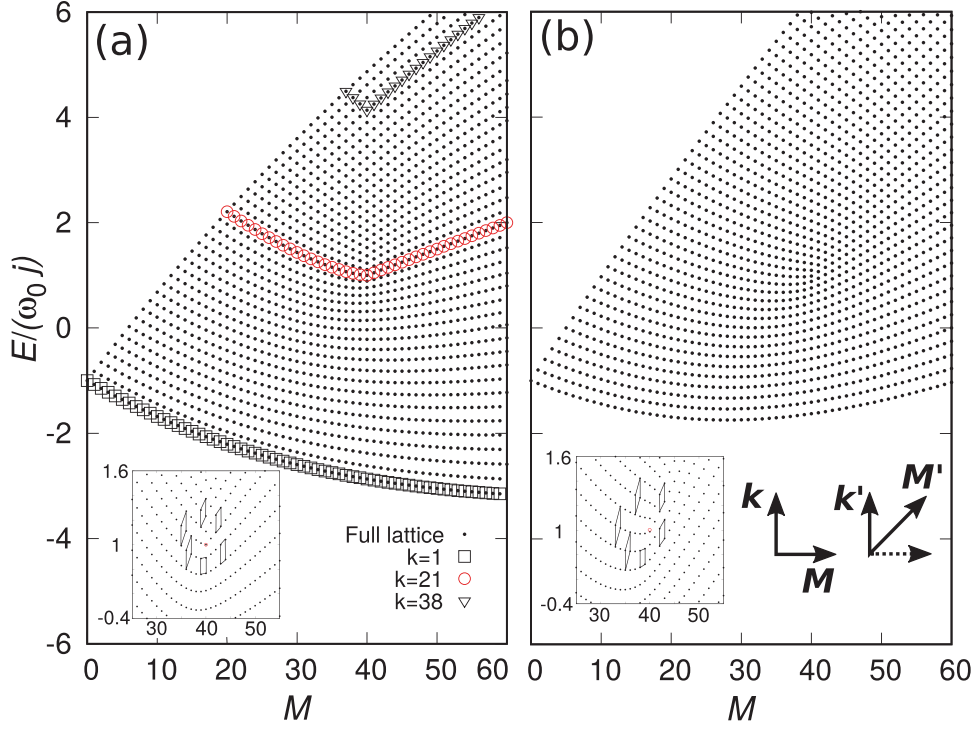


Figure 3. Quantum energy-momentum maps of the Hamiltonian (1) with $\lambda = 2.5$, $\delta = 0$ and $N = 2j = 40$. The $\omega = \omega_0 = 1$ and $\omega = 2, \omega_0 = 1$ lattices of eigenstates are in panels (a) and (b), respectively. The highlighted chains of points correspond to the eigenstates with the same principal quantum number k and variable M . The insets show a transformation of the elementary lattice cell after a closed loop around the monodromy point.

quantum number M . The lattices corresponding to tuned $\Delta\omega = 0$ and detuned $\Delta\omega > 0$ spectra are shown in panels (a) and (b), respectively. At each point (M, E_k) of the lattice we can construct an elementary cell, that is a rectangle defined by ‘horizontal’ and vertical basis vectors $\mathbf{M} \equiv (1, E_k(M + 1) - E_k(M))$ and $\mathbf{k} \equiv (0, E_{k+1}(M) - E_k(M))$. The lattice has a defect at the monodromy point $(M, E) = N^*(1, \mathcal{E}'_c) = (2j, \omega_0 j)$. Following a closed loop around this point, as shown in the insets of figure 3, the basis vectors undergo a transformation

$$\begin{pmatrix} M' \\ k' \end{pmatrix} = \underbrace{\begin{pmatrix} 1 & 1 \\ 0 & 1 \end{pmatrix}}_{\boldsymbol{\mu}^T} \begin{pmatrix} M \\ k \end{pmatrix}, \tag{22}$$

where $\boldsymbol{\mu}^T$ is a transpose of the classical monodromy matrix $\boldsymbol{\mu}$ describing the transformation of elementary cycles on tori after a loop around the pinched torus containing a single focus–focus singularity [7].

The lattice defect in the energy-momentum map can also be manifested by connecting the sequences of points $E_k(M)$ with fixed k and variable M . Three such sequences are highlighted in figure 3(a). While all sequences below the monodromy point show a smooth bend, suggesting a quadratic dependence of energy on M , those above the monodromy point exhibit a sharp break, consistent with a linear type of the dependence. This is in general related to different

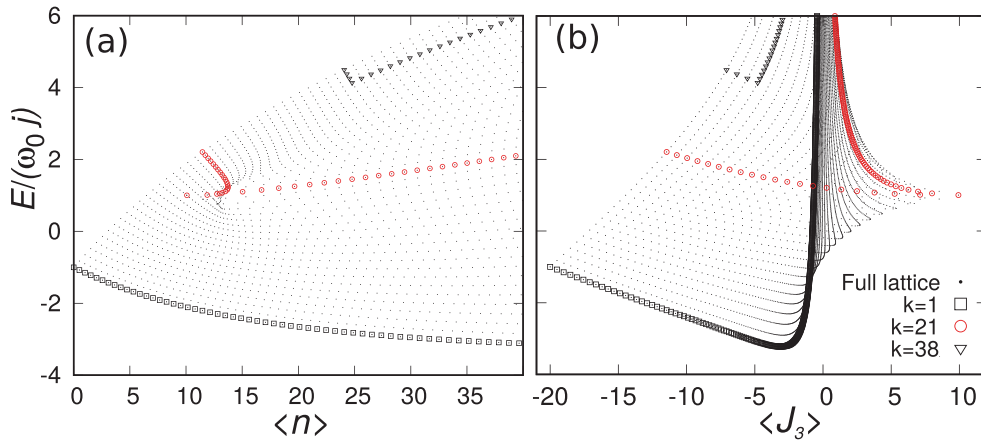


Figure 4. Peres lattices of observables $\hat{n} = \hat{b}^\dagger \hat{b}$ and \hat{J}_3 for Hamiltonian (1) with the same parameter values as in figure 3(a). The chains of points with the same principal quantum number are again highlighted.

nature of excitations (e.g. rotational and vibrational in molecular realizations of monodromy) below and above the critical energy [8–11]. We stress that in our system, the monodromy energy (18) coincides with the critical borderline for an excited-state quantum phase transition present in the $M = N^*$ subspace [40, 48]. This coincidence is analogous to the cases reported in [14–16] and can be anticipated as rather common also in other $f = 2$ integrable realizations of excited-state quantum phase transitions.

Quantum energy-momentum maps display joined spectra of two compatible integrals of motions. It means that both quantities are sharply determined in each eigenstate. However, one can also create eigenstate lattices with the abscissa capturing just an *expectation value* of an arbitrary—i.e. generally not conserved—quantum observable. Since this representation of a general spectrum, which is not restricted to integrable systems, was proposed by A. Peres [49], we call it a Peres lattice. It is useful in the visualization of quantum chaos in mixed systems, in which the lattice contains both ordered and disordered domains, see e.g. [38, 40, 50]. Two Peres lattices of the integrable Dicke model with $\Delta\omega = 0$ are depicted in figure 4. The first one, in panel (a), shows expectation values $\langle n \rangle_k$ of the number of field bosons in the eigenstates with energy E_k , the second lattice in panel (b) shows in the same manner the expectation values $\langle J_3 \rangle_k$ of the quasispin z -projection. Note that if the values $\langle n \rangle_k$ and $\langle J_3 \rangle_k$ at each point are summed, one would obtain precisely the lattice in figure 3(a) shifted by a constant j , see equation (2).

We observe that both lattices in figure 4 exhibit apparent singularities at the monodromy point. However, the topologies of these singularities differ considerably from each other and from that in the energy-momentum map. Taking this observation the other way round, we can conclude that appearance of various defects in arbitrary Peres lattices may serve as a useful heuristic indicator of monodromy in a general (otherwise unknown) quantum system.

An important task related to a possible experimental verification of quantum monodromy is to identify its signatures in the structure of eigenstates and in the time evolution. The key observation in the present system is that the $\lambda_\gamma > \lambda'_c$ eigenstates with $M = N^*$ in a vicinity of the monodromy energy $E = N^* \mathcal{E}'_c$ exhibit a very large overlap with the unperturbed ground state $(n, n^*) = (0, N^*)$. This localization becomes singular for $N^* \rightarrow \infty$ and follows from the diverging time spent by the classical trajectory in an infinitesimal vicinity of the

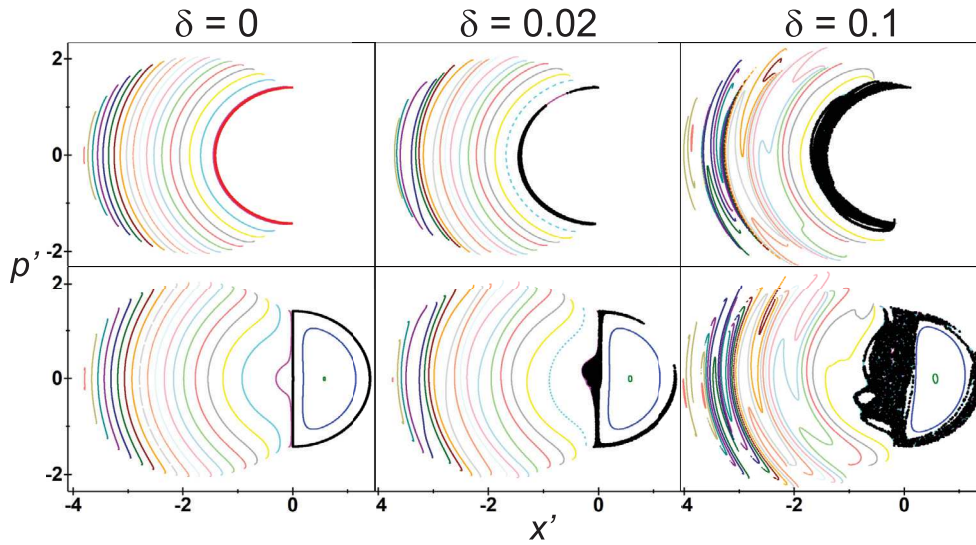


Figure 5. Poincaré sections showing passages of 21 classical orbits through the plane $\phi' = 0$ at energy $\mathcal{E} = \mathcal{E}'_c$ for Hamiltonian (6) with $\omega = \omega_0 = 1$ and $\lambda_\gamma = 2.5$. The three columns correspond to the indicated values of parameter δ . The upper row collects passages of orbits from negative to positive ϕ' values, the lower row passages in the opposite direction. Colors (online) distinguish individual orbits, black denotes the orbit with an average value $\langle \mathcal{M} \rangle$ very close to unity (the value $\mathcal{M} = 1$ corresponds to the pinched torus for $\delta = 0$).

$(x', p') = (0, 0)$ stationary point. An analogous behavior is observed also in other $f = 2$ systems with the focus–focus type of monodromy [15, 51] as well as in $f = 1$ systems with a local maximum of the Hamiltonian [52, 53]. In the present case, the localization results in a sharp local decrease of the atom–field entanglement entropy [40] and has specific consequences for the dynamics of relaxation processes following a quantum quench [48, 51]. In particular, a quench from the $\lambda < \lambda'_c$ ground state to the $\lambda_\gamma > \lambda'_c$ critical region results in a slow decay of the initial state (due to its large overlap with the eigenstates in the critical region) [51], while a quench from the $\lambda > \lambda'_c$ side leads, on contrary, to an immediate decay of the initial state and its weak re-occurrences [48]. A more detailed analysis of the quantum quench dynamics in the extended Dicke model is presently a subject of our study.

5. Decay of monodromy

Monodromy in its original form is restricted solely to integrable systems. However, an extension of this concept was proposed to softly chaotic systems, in which the singular torus survives the perturbation in the sense of the Kolmogorov–Arnold–Moser theorem [54]. The present model enables us to study the ‘fate’ of monodromy in the non-integrable regime explicitly, by setting a non-zero value of parameter δ in Hamiltonian (1).

Poincaré sections for a sample of classical trajectories having precisely the energy $\mathcal{E} = \mathcal{E}'_c$ of the monodromy point, and their evolution with increasing δ , are seen in figures 5 and 6. The dynamics was calculated from the general Hamiltonian (6) with the coordinates and momenta transformed according to equations (9) and (10). The figures show multiple passages of individual orbits through the plane $\phi' = 0$ in the phase space for the transformed Hamiltonian (11)

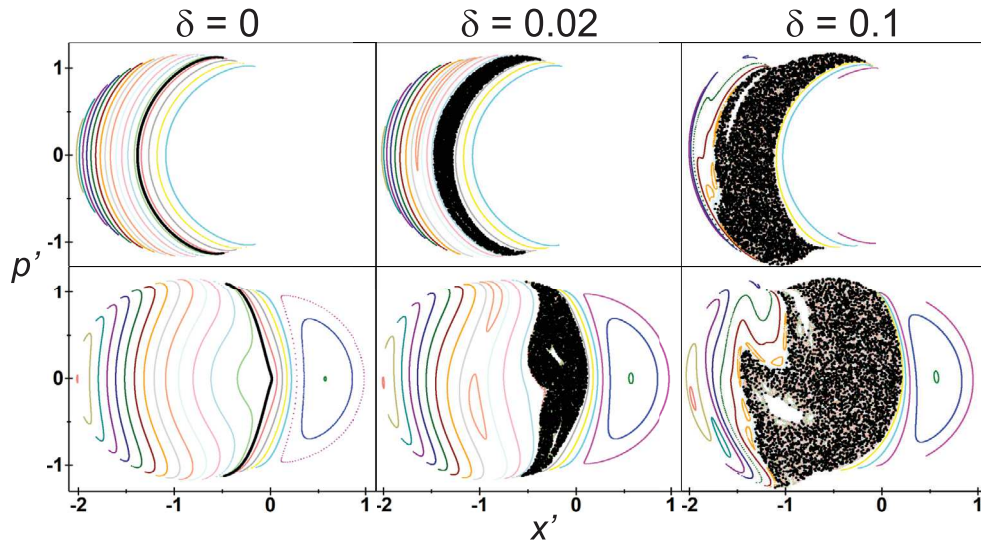


Figure 6. The same as in figure 5, but for $\omega = 2, \omega_0 = 1$.

with $\Delta\omega = 0$ (figure 5) or $\Delta\omega > 0$ (figure 6). The perturbation strength δ grows from the left column to the right. The upper and lower rows separate two different directions of the orbit passage through the plane of the section. If forward and backward segments of the same orbit were plotted in the same figure, they would form a closed curve, but the curves corresponding to different orbits would cross each other. This behavior (which is in contrast to common Hamiltonians with a quadratic dependence on momenta) is due to a non-trivial (often non-monotonous) evolution of angle ϕ , see equation (14).

The leftmost panels of figures 5 and 6, which correspond to the integrable regime, carry complementary information to previously discussed figure 1. The previous figure displayed different \mathcal{E} contours of the Hamiltonian (11) with fixed \mathcal{M} , while the present figures represent (x', p') solutions of equation (11) with fixed \mathcal{E} and different \mathcal{M} . In all these figures, we can identify the critical orbits with $(\mathcal{M}, \mathcal{E}) = (1, \mathcal{E}'_c)$ that belong to the pinched torus. As δ increases from zero (in the middle and right panels of figures 5 and 6), the quantity \mathcal{M} is no more conserved and the orbits can be characterized only by time averages $\langle \mathcal{M} \rangle$. Therefore, if focusing on the $\mathcal{E} = \mathcal{E}'_c$ orbits with $\langle \mathcal{M} \rangle \approx 1$ (passages of these orbits are plotted by the darkest, black shade), we pursue the evolution of the pinched torus and its close neighbors in the perturbed system.

It is clear from figures 5 and 6 that the $\langle \mathcal{M} \rangle \approx 1$ orbits become chaotic at the earliest stage of the system's perturbation. Already in the middle panels of both figures, that is at a very moderate value of δ , these orbits generate a distinct quasi-ergodic domain in the phase space (bounded cloud of random crossings). This domain further grows with increasing δ . Note that the observed instability of the pinched torus results from the unstable character of the $(x', p') = (0, 0)$ stationary point passed by its orbits.

What is the quantum counterpart of the above classical scenario? Metamorphoses of the quantum energy-momentum map of a tuned system with increasing perturbation strength are depicted in figure 7. In the upper-left panel we see the lattice corresponding to the $\delta = 0$ Hamiltonian; it is identical with the lattice in panel (a) of figure 3. The other three panels show what happens if δ is increased. In these cases, M on the horizontal axis represents only a quantum expectation value $\langle M \rangle$ in individual eigenstates. The first two non-zero values of δ in figure 7 were chosen the same as in the Poincaré section figures—at these perturbation strengths we observe initial stages of the lattice

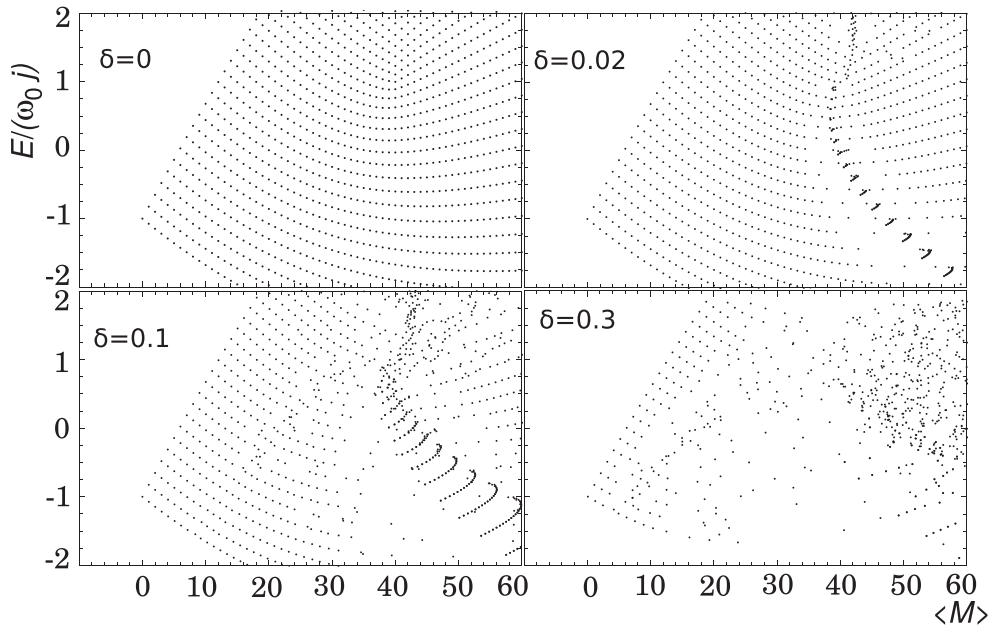


Figure 7. Breakdown of the quantum energy-momentum lattice from figure 3(a) with increasing perturbation δ .

destruction. The fourth value of δ in figure 7 is larger, and we already find a considerable part of the lattice being completely messed up. This agrees with the original use of Peres lattices for visualization of chaos in quantum systems [49].

As seen in figure 7, the point defect defining the quantum monodromy in the energy-momentum lattice is destroyed already with the weakest non-integrable perturbation of the Hamiltonian. It happens to be right at the center of a large break that splits the spectrum in the vertical direction. This is not an accident. The break starts developing along a line where the energy spacing $\Delta E = E_{k+1} - E_k$ between neighboring levels is minimal. As follows from basic perturbation theory, for these states the perturbation efficiency is particularly large due to small energy denominators in the corresponding expressions. The monodromy point naturally belongs to this line. Indeed, the simple semiclassical relation $\Delta E = 2\pi\hbar/\tau$, connecting the energy spacing ΔE in an $f = 1$ system with the period τ of classical motions at the corresponding energy, indicates that the $\tau \rightarrow \infty$ orbits on the pinched torus generate very dense, $\Delta E \rightarrow 0$, regions of quantum spectra. In these parts, any generic perturbation of the Hamiltonian results in a fast level repulsion. The same mechanism of chaos proliferation was observed also in other quantum systems [50]. So we may conclude that in a typical situation spectral defects of the present type do not survive too long in the non-integrable regime.

6. Conclusions

We studied monodromy of the focus–focus type in the integrable Tavis–Cummings limit of the Dicke model. We showed that the pinched torus in the phase space is formed by orbits with total energy E equal to the energy of a fully excited atomic ensemble and momentum M (the total number of atomic and field excitation quanta) equal to the number of excitable atoms. These orbits, which are partly similar to critical orbits of a spherical pendulum, represent an analog of the dynamic superradiance phenomenon under circumstances of a strictly closed

system. In particular, the initial state of maximally excited atoms and no field in the cavity becomes a very slowly decaying configuration (a point of unstable equilibrium in the infinite size limit), while the fast decay takes place on a halfway to the full atomic de-excitation. This resembles the superradiant peak known from the open Dicke systems, although the scaling with the number of atoms is only linear in the closed case.

On the quantum level, monodromy shows up as a point defect in the discrete energy-momentum map, and as a singularity in other Peres lattices. Quantum signatures of monodromy are closely related to an excited-state quantum phase transition in the critical M -subspace of Hamiltonian eigenstates, in particular to a sharp local increase (logarithmic divergence in the infinite-size limit) of the density of states within this subset. On the other hand, the total density of states in all M -subspaces exhibits only a discontinuity of its first derivative at the corresponding energy. We anticipate that this behavior is common to all $f = 2$ systems with the focus–focus singularity as their Hamiltonians close to the singularity can be cast in a locally quadratic, thus separable form with two positive and two negative Hessian eigenvalues (e.g. as a Hamiltonian with a quadratic kinetic term near a quadratic potential maximum). Dynamical consequences of these phenomena are subject of ongoing research.

We have shown that classical and quantum signatures of monodromy in our model disappear already with a very weak perturbation of the system. We anticipate that fragility is a rather common property of the present type of monodromy as the underlying classical stationary points are unstable (therefore inclined to chaotic dynamics) and imply infinite-period orbits (which are connected with dense, hence vulnerable parts of quantum spectra).

Acknowledgments

In memory of Tobias Brandes, whose gentle guidance and encouragement are painfully missed. This work was supported by the Czech Science Foundation under project no. P203-13-07117S.

References

- [1] Bates L M and Cushman R H 1997 *Global Aspects of Classical Integrable Systems* (Basel: Birkhäuser)
- [2] Pelayo Á and Vũ Ngọc S 2011 *Bull. Am. Math. Soc.* **48** 409
- [3] Zou M 1992 *J. Geom. Phys.* **10** 37
- [4] Zung N T 1997 *Differ. Geom. Appl.* **7** 123
- [5] Duistermaat J J 1980 *Commun. Pure Appl. Math.* **33** 687
- [6] Cushman R H and Duistermaat J J 1988 *Bull. Am. Math. Soc.* **19** 475
- [7] Vũ Ngọc S 1999 *Commun. Math. Phys.* **203** 465
- [8] Child M S 2007 *Adv. Chem. Phys.* **136** 39
- [9] Cushman R H, Dullin H R, Giacobbe A, Holm D D, Joyeux M, Lynch P, Sadovskii D A and Zhilinskiĭ B I 2004 *Phys. Rev. Lett.* **93** 024302
- [10] Efsthathiou K, Joyeux M and Sadovskii D A 2004 *Phys. Rev. A* **69** 032504
- [11] Sadovskii D A and Zhilinskiĭ B I 2010 *Mol. Phys.* **104** 2595
- [12] Zhilinskiĭ B I 2011 *The Complexity of Dynamical Systems: a Multi-Disciplinary Perspective* ed J Dubbeldam *et al* (Weinheim: Wiley-VCH) p 159
- [13] Dullin H R and Waalkens H 2016 arXiv:1612.00823 [math-ph]
- [14] Heinze S, Cejnar P, Jolie J and Macek M 2006 *Phys. Rev. C* **73** 014306
- [15] Macek M, Cejnar P, Jolie J and Heinze S 2006 *Phys. Rev. C* **73** 014307
- [16] Cejnar P, Macek M, Heinze S, Jolie J and Dobeš J 2006 *J. Phys. A: Math. Gen.* **39** L515
- [17] Larese D, Pérez-Bernal F and Iachello F 2013 *J. Mol. Struct.* **1051** 310
- [18] Caprio M A, Cejnar P and Iachello F 2008 *Ann. Phys.* **323** 1106

- [18] Stránský P, Macek M and Cejnar P 2014 *Ann. Phys.* **345** 73
- [19] Stránský P and Cejnar P 2016 *Phys. Lett. A* **380** 2637
- [20] Dicke R H 1954 *Phys. Rev.* **93** 99
- [21] Babelon O, Cantini L and Douçot B 2009 *J. Stat. Mech.* P07011
- [22] Brandes T 2005 *Phys. Rep.* **408** 315
- [23] Keeling J 2014 *Light-Matter Interactions and Quantum Optics* (Create Space Independent Publishing Platform)
- [24] Gross M and Haroche S 1982 *Phys. Rep.* **93** 301
- [25] Benedict M G (ed) 1996 *Super-radiance: Multiatomic Coherent Emission* (New York: Taylor and Francis)
- [26] Fuchs S, Ankerhold J, Blencowe M and Kubala B 2016 *J. Phys. B: At. Mol. Opt. Phys.* **49** 035501
- [27] Wang Y K and Hioe F T 1973 *Phys. Rev. A* **7** 831
- [28] Hepp K and Lieb E H 1973 *Phys. Rev. A* **8** 2517
- [29] Emary C and Brandes T 2003 *Phys. Rev. E* **67** 066203
- [30] Auerbach N and Zelevinsky Z 2011 *Rev. Prog. Phys.* **74** 106301
- [31] Cong K, Zhang Q, Wang Y, Noe G T, Belyanin A and Kono J 2016 *J. Opt. Soc. Am. B* **33** C80
- [32] Dimer F, Estienne B, Parkins A S and Carmichael H J 2007 *Phys. Rev. A* **75** 013804
- [33] Baumann K, Guerlin C, Brennecke F and Esslinger T 2010 *Nature* **464** 1301
- [34] Baumann K, Mottl R, Brennecke F and Esslinger T 2011 *Phys. Rev. Lett.* **107** 140402
- [35] Klinder J, Keßler H, Wolke M, Mathey L and Hemmerich A 2015 *Proc. Natl Acad. Sci.* **112** 3290
- [36] Baden M P, Kyle J A, Grimsmo A L, Parkins S and Barrett M D 2014 *Phys. Rev. Lett.* **113** 020408
- [37] Brandes T 2013 *Phys. Rev. E* **88** 032133
- [38] Bastarrachea-Magnani M A, Lerma-Hernández S and Hirsch J G 2014 *Phys. Rev. A* **89** 032101
- [38] Bastarrachea-Magnani M A, Lerma-Hernández S and Hirsch J G 2014 *Phys. Rev. A* **89** 032102
- [39] Bastarrachea-Magnani M A, Lerma-Hernández S and Hirsch J G 2016 *J. Stat. Mech.* 093105
- [40] Kloc M, Stránský P and Cejnar P 2017 *Ann. Phys.* **382** 85
- [41] Viehmann O, von Delft J and Marquardt F 2011 *Phys. Rev. Lett.* **107** 113602
- [42] Jaynes E T and Cummings F W 1963 *Proc. IEEE* **51** 89
- [43] Tavis M and Cummings F W 1968 *Phys. Rev.* **170** 379
- [44] Bhaseen M J, Mayoh J, Simons B D and Keeling J 2012 *Phys. Rev. A* **85** 013817
- [45] Cejnar P and Stránský P 2016 *Phys. Scr.* **91** 083006
- [46] de Aguiar M A M, Furuya K, Lewenkopf C H and Nemes M C 1992 *Ann. Phys.* **216** 291
- [47] Bakemeier L, Alvermann A and Fehske H 2013 *Phys. Rev. A* **88** 043835
- [48] Pérez-Fernández P, Cejnar P, Arias J M, Dukelsky J, García-Ramos J E and Relaño A 2011 *Phys. Rev. A* **83** 033802
- [49] Peres A 1984 *Phys. Rev. Lett.* **53** 1711
- [50] Stránský P, Hruška P and Cejnar P 2009 *Phys. Rev. E* **79** 046202
- [50] Stránský P, Hruška P and Cejnar P 2009 *Phys. Rev. E* **79** 066201
- [51] Santos L F and Pérez-Bernal F 2015 *Phys. Rev. A* **92** 050101
- [52] Cary J R and Rusu P 1992 *Phys. Rev. A* **45** 8501
- [53] Leyvraz F and Heiss W D 2005 *Phys. Rev. Lett.* **95** 050402
- [54] Broer H W, Cushman R H, Fassò F and Takens F 2007 *Ergod. Theory Dynam. Sys.* **27** 725

Reprint: Quantum quench dynamics in Dicke superradiance models

H.1 Main Achievements

- Two types of quench protocols (forward and backward) are applied in the EDM within $\delta = 0$ ($f = 1$) and $\delta \neq 0$ ($f = 2$) setting.
- In the forward quench protocols the initial unperturbed ground state is stabilized by the presence of an ESQPT in both $f = 1$ and $f = 2$ cases regardless of the ESQPT type.
- In the backward quench protocols the power-law modulation of the decay of the initial superradiant ground state is suppressed at medium time scales for $f = 1$ case and some ESQPTs in the $f = 2$ case.
- In non-integrable setting chaos can smear out the effect of the ESQPTs.
- The evolution of the observables follows the same qualitative pattern as the survival probability therefore it may be sensitive to the presence of the ESQPTs in a similar way.

Quantum quench dynamics in Dicke superradiance models

Michal Kloc,* Pavel Stránský, and Pavel Cejnar

*Institute of Particle and Nuclear Physics, Faculty of Mathematics and Physics,
Charles University, V Holešovičkách 2, Prague, 18000, Czech Republic*

(Dated: June 29, 2018)

We study the quantum quench dynamics in an extended version of the Dicke model where an additional parameter allows a smooth transition to the integrable Tavis-Cummings regime. We focus on the influence of various quantum phases and excited-state quantum phase transitions (ESQPTs) on the survival probability of the initial state. We show that, depending on the quench protocol, an ESQPT can either stabilize the initial state or, on the contrary, speed up its decay to the equilibrated regime. Quantum chaos smears out the manifestations of ESQPTs in quench dynamics, therefore significant effects can only be observed in integrable or weakly chaotic settings. Similar features are present also in the post-quench dynamics of some observables.

I. INTRODUCTION

The advent of quantum simulators opened routes to laboratory realizations of artificial quantum systems designed either to implement certain utilizable functions, or to demonstrate some fundamental principles [1, 2]. Examples include efforts to build an efficient quantum computer (see, e.g., Ref. [3]) or experiments with quantum phase transitions (see, e.g., Refs. [4–6]). An important mode of use of quantum simulators lies in probing the dynamics of quantum systems far from thermodynamical equilibrium [7, 8]. This is often achieved via a protocol called quantum quench, which in its sudden form consists in the following steps [9–11]: (a) take a system described by Hamiltonian \hat{H}_i and prepare it in an eigenstate $|\psi_i\rangle$, (b) suddenly switch the Hamiltonian to \hat{H}_f , and (c) with increasing time t , measure the probability $P(t)$ of finding the initial state $|\psi_i\rangle$ in the state evolved from it by \hat{H}_f . It is usually assumed that the initial and final Hamiltonians are members of the same family depending on an external parameter λ , so $\hat{H}_i \equiv \hat{H}(\lambda_i)$ and $\hat{H}_f \equiv \hat{H}(\lambda_f)$ with λ_i and λ_f denoting initial and final parameter values.

The evolution of the initial-state survival probability $P(t)$ is entirely encoded in the energy distribution of the initial state expressed in the final Hamiltonian eigenstates. At first, $P(t)$ drops with a rate related just to the final energy dispersion. However, at later stages of the evolution, rather complex dynamical regimes occur which gradually disclose more and more subtle details of the final energy distribution. Correlations between individual final energy levels and the corresponding occupation probabilities become apparent at these stages [12]. Although the medium- and long-time evolution is usually characterized by a very low average of the survival probability, sharp peaks of $P(t)$ are repeatedly observed, indicating sudden revivals of the initial state.

The quench dynamics in complex quantum systems currently represents a subject of intense theoretical and experimental research, see, e.g., Refs. [4, 6, 8–25]. An

important direction of this research is aimed at dynamical imprints of various forms of quantum criticality that emerge in the infinite-size limit of some systems. For example, the so-called Dynamical Quantum Phase Transition (DQPT) shows up as a non-analyticity observed directly in the survival probability as a function of time [6, 23]. Also relevant for the quench dynamics are the concepts of ground-state Quantum Phase Transition (QPT) [26, 27] and Excited-State Quantum Phase Transition (ESQPT) [28–32]. Since these are rooted in non-analytic properties of the system's stationary states (ground or excited states) taken as a function of the control parameter, their effect in quench dynamics is not seen as a sharp-time anomaly like in the DQPT case, but rather shows as a qualitative change of the quench dynamics with varying difference $\Delta\lambda = \lambda_f - \lambda_i$. The changes appear if the parameter shift connects different quantum phases of the system. In spite of numerous theoretical efforts to clarify the relations between (ES)QPTs and quench dynamics (see, e.g., Refs. [9–11, 13–15, 17, 20, 25] for QPTs and [16, 18, 21] for ESQPTs), the problem still remains open for further investigation.

In this paper, we address this problem, particularly that of the ESQPT influence, by analyzing the quench dynamics in a model generalizing the Dicke superradiance phenomenon in cavity QED systems [33–35]. The model contains a QPT [36] and several types of ESQPTs [16, 37–42]. Its ground-state critical behavior was demonstrated experimentally [5]. We show that the effect of ESQPTs on the quench dynamics strongly depends on the ESQPT type (in the sense of the classification described in Ref. [32]) and on the quench protocol (selection of the initial state and size of the parameter change). The effect is most pronounced in the integrable Tavis-Cummings regime [43], in which the dynamics becomes effectively determined by a single degree of freedom, but can be observed also in the full (non-integrable) regime.

The plan of the paper is as follows: In Section II, we introduce an extended version of Dicke model (Sec. II A), that will be employed in this work, and outline the general theoretical background on the quench dynamics (Sec. II B). In Section III, we describe numerical results on the quench dynamics gained within the model

* E-mail address: kloc@ipnp.troja.mff.cuni.cz

in its integrable (Sec. III A) and non-integrable regimes (Sec. III B). We focus on two types of quench protocols named forward and backward protocols. Section IV brings a brief summary.

II. THEORETICAL BACKGROUND

A. The extended Dicke model

The Dicke model [33] was formulated to describe an idealized interaction of an ensemble of N two-level atoms with one-mode electromagnetic field. The original intention was to demonstrate the dynamical superradiance phenomenon, i.e., coherent radiation induced by collective behavior of atoms in the regime of weak atom-field coupling. Later it turned out that in the strong coupling regime, the model exhibits another form of superradiance, namely a thermal phase transition [34, 35] and, in the zero-temperature limit, the corresponding QPT [36] to an equilibrium superradiant phase. A route to laboratory realizations of the cavity QED system with strong atom-field coupling was proposed in Ref. [44] and led to successful experiments with the superradiant QPT reported in Ref. [5].

We use here the so-called Extended Dicke Model [37, 38, 41, 45] with the Hamiltonian (we set $\hbar = 1$)

$$\hat{H} = \omega \hat{b}^\dagger \hat{b} + \omega_0 \hat{J}_z + \frac{\lambda}{\sqrt{N}} \left[\hat{b}^\dagger \hat{J}_- + \hat{b} \hat{J}_+ + \delta \left(\hat{b}^\dagger \hat{J}_+ + \hat{b} \hat{J}_- \right) \right]. \quad (1)$$

Here, \hat{b}^\dagger and \hat{b} stand for creation and annihilation operators of the bosonic field (photons) while \hat{J}_\pm and \hat{J}_z represent collective quasi-spin operators affecting the ensemble of atoms. These are written as $\hat{J}_\bullet = \sum_{k=1}^N \hat{\sigma}_\bullet^k / 2$ (with the symbol \bullet standing for $z, +, -$), where $\hat{\sigma}_\bullet^k$ is the Pauli matrix acting on the k th atom whose lower and upper states read as $\begin{pmatrix} 1 \\ 0 \end{pmatrix}$ and $\begin{pmatrix} 0 \\ 1 \end{pmatrix}$, respectively [so, for example, $\hat{\sigma}_+^k / 2 = (\hat{\sigma}_x^k + i\hat{\sigma}_y^k) / 2$ excites the k th atom from the lower to the upper state etc.]. The first two terms in Eq. (1) represent the free field (with a single boson energy ω) and the free atoms (with a single atom excitation energy ω_0), while the third term describes an atom-field interaction with an overall strength $\lambda \in [0, \infty)$ and an additional parameter $\delta \in [0, 1]$ which scales the so-called counter-rotating terms. The variation of δ induces a smooth crossover from the Tavis-Cummings regime [43] with $\delta = 0$ (full neglect of the counter-rotating terms) to the original Dicke regime [33] with $\delta = 1$.

Note that the use of collective quasi-spin operators in the interaction term is based on the assumption that the size of the atomic ensemble is much smaller than the wavelength of radiation, so that the interaction is uniform for all atoms. Since \hat{J}^2 commutes with the Hamiltonian (1), the dynamics does not mix subspaces with different quantum numbers j of \hat{J}^2 . We therefore select a single- j subspace, namely that with the maximal value $j = N/2$, which is fully symmetric with respect to

the exchange of atoms (subspaces with lower values of j appear in numerous replicas differing by the type of exchange symmetry) [46]. So all physical states $|\psi\rangle$ can be expressed as linear combinations of the basis states $|n\rangle|m\rangle$, where $n = 0, 1, 2, \dots$ is the number of bosons and $m = -j, -j+1, \dots, +j$ the quasi-spin z -projection.

The classical limit of Hamiltonian (1) can be realized in terms of two pairs of canonically conjugate coordinate and momentum variables, hence the model has in general two degrees of freedom: $f = 2$ [36, 38]. One of them is associated with the field states; the corresponding part of the phase space is a plane. The other represents the collective atomic states; their phase space is the Bloch sphere. Details can be found, e.g., in Refs. [41, 42]. The minimum of the classical energy landscape in the whole phase space, i.e., the lowest stationary point of the system, corresponds to the energy of the quantum ground state in the $N \rightarrow \infty$ limit. It can be written as

$$\frac{E_{\text{g.s.}}}{\omega_0 j} = \begin{cases} -1 & \text{for } \lambda \in [0, \lambda_c), \\ -\frac{1}{2} \left(\frac{\lambda_c^2}{\lambda^2} + \frac{\lambda^2}{\lambda_c^2} \right) & \text{for } \lambda \in [\lambda_c, \infty), \end{cases} \quad (2)$$

where the critical parameter value

$$\lambda_c = \frac{\sqrt{\omega\omega_0}}{1+\delta} \quad (3)$$

sets a second-order ground-state QPT, where $d^2 E_{\text{g.s.}} / d\lambda^2$ changes discontinuously.

Higher (unstable or quasi-stable) stationary points of the classical Hamiltonian demarcate the ESQPTs of the model. Detailed analyses can be found in Refs. [38, 41]. One of the ESQPT critical borderlines in the plane parameter $\lambda \times$ energy E can be written as

$$\frac{E_{c1}}{\omega_0 j} = \begin{cases} -1 & \text{for } \lambda \in [\lambda_c, \lambda_0), \\ -\frac{1}{2} \left(\frac{\lambda_0^2}{\lambda^2} + \frac{\lambda^2}{\lambda_0^2} \right) & \text{for } \lambda \in [\lambda_0, \infty), \end{cases} \quad (4)$$

$$\lambda_0 = \frac{\sqrt{\omega\omega_0}}{1-\delta}.$$

The energy (4) is associated with a saddle point of the energy landscape. Therefore, according to the classification described in Ref. [32], it corresponds to an ESQPT of type $(f, r) = (2, 1)$, where r is the rank of the non-degenerate stationary point (number of negative eigenvalues of the Hessian matrix). This leads to a logarithmic divergence of the first derivative $d\rho/dE$ of the smoothed level density $\rho(E)$ at $E = E_{c1}$ (that is a step-like but continuous behavior of ρ at this energy) [31, 32].

Two other ESQPTs appear at energies [38, 41]

$$\frac{E_{c2}}{\omega_0 j} = -1 \quad \text{for } \lambda \in [\lambda_0, \infty), \quad (5)$$

$$\frac{E_{c3}}{\omega_0 j} = +1 \quad \text{for } \lambda \in [0, \infty). \quad (6)$$

They are both of the type $(f, r) = (2, 2)$ and show as jumps of the first derivative $d\rho/dE$ of the smoothed level density (i.e., breaks of ρ) at E_{c1} and E_{c2} [31, 32].

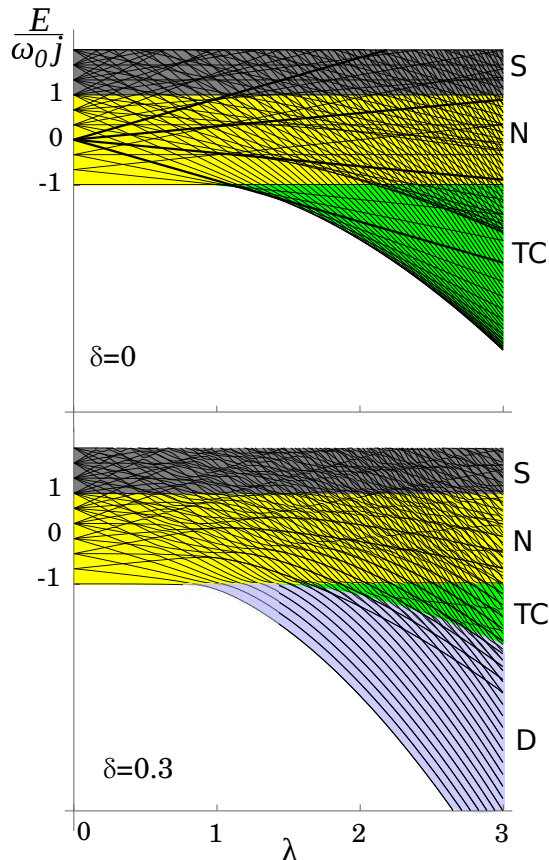


FIG. 1. (Color online) Level dynamics and quantum phase diagrams of the extended Dicke Hamiltonian (1) with $\delta = 0$ (upper panel) and $\delta = 0.3$ (lower panel), both for $\omega = \omega_0 = 1$. The ground-state QPTs are at $\lambda_c = 1$ for $\delta = 0$ and at $\lambda_c \approx 0.77$ for $\delta = 0.3$. Quantum phases D (Dicke), TC (Tavis-Cummings), N (Normal) and S (Saturated) are marked by colors. ESQPT borderlines coincide with the phase boundaries. Quantum spectra are drawn for $j = 3$. In the $\delta = 0$ panel, the $M = 3$ states are plotted by thicker lines to show that levels from different M -subspaces mutually cross.

The diagrams showing individual energy levels in the $\lambda \times E$ plane for a finite- N realization of the $\delta = 0$ and $\delta \neq 0$ models together with the $N \rightarrow \infty$ ESQPT borderlines (4), (5) and (6) are given in Fig. 1. The domains in between the ESQPT borderlines define quantum phases of the system. In Fig. 1 they are marked by different colors and abbreviated as D (Dicke), TC (Tavis-Cummings), N (Normal) and S (Saturated). The reasoning for this notation and a more detailed discussion can be found in Ref. [41]. Note that quantum phases cannot, in general, be distinguished by some order parameters (expectation values of suitably selected observables in individual eigenstates), but rather by different energy dependences (trends) of these expectation values smoothed over neighboring eigenstates [41, 46].

In the Tavis-Cummings $\delta = 0$ limit of the model [43], the treatment of phases can be qualitatively simplified.

In this case, the Hamiltonian (1) has an additional integral of motion

$$\hat{M} = \hat{b}^\dagger \hat{b} + \hat{J}_z + j \quad (7)$$

and the system is integrable [note that a general $\delta \neq 0$ Hamiltonian conserves only the parity $\hat{\Pi} = \exp(i\pi\hat{M})$]. The value of the conserved quantity can be written as $M = n + n^*$, where n is the number of bosons and $n^* = m + j$ the number of excited atoms. The total spectrum of quantum energy levels for the $\delta = 0$ system with any λ is comprised of mutually non-interacting sub-spectra with different values of $M = 0, 1, 2, \dots$ (see the upper panel of Fig. 1). Each of these spectra separately can be subject (in the $N \rightarrow \infty$ limit) to a semi-classical phase transitional analysis. To do so, it is convenient to use a canonical transformation that reduces the number of effective degrees of freedom of the $\delta = 0$ system to $f = 1$ [41, 42]. The transformed classical Hamiltonian depends only on one pair of new conjugate variables and on the conserved quantity M , thus allows one to identify stationary and quasi-stationary points for different values of M .

The results of the semi-classical analysis of the $\delta = 0$ model are the following [41, 42]: While the subspaces with $M \neq N$ show no critical effects, the one with $M = N$ has both a QPT and an ESQPT. Indeed, the energy of the lowest state in the $M = N$ subspace in the $N \rightarrow \infty$ limit for the $\omega > \omega_0$ hierarchy is given by

$$\frac{E_{l.s.}}{\omega_0 j} = \begin{cases} +1 & \lambda \leq \bar{\lambda}_c, \\ +1 - \frac{4}{\omega_0} g(\lambda) \left[\lambda \sqrt{1 - g(\lambda)} - \bar{\lambda}_c \right] & \lambda > \bar{\lambda}_c, \end{cases} \quad (8)$$

$$g(\lambda) = \frac{2}{3} - \frac{2}{9} \left(\frac{\bar{\lambda}_c}{\lambda} \right)^2 - \frac{2}{9} \frac{\bar{\lambda}_c}{\lambda} \sqrt{\left(\frac{\bar{\lambda}_c}{\lambda} \right)^2 + 3},$$

where the critical coupling

$$\bar{\lambda}_c = \frac{\omega - \omega_0}{2} \quad (9)$$

marks a discontinuity of $d^2 E_{l.s.}/d\lambda^2$, which can be interpreted as the second-order QPT in the $M = N$ subspace [16]. An associated ESQPT appears at the critical energy

$$\frac{E_{c4}}{\omega_0 j} = +1 \quad \text{for } \lambda \in [\bar{\lambda}_c, \infty), \quad (10)$$

where one observes divergence of the smoothed level density ρ in the $M = N$ subspace. Since the classical Hamiltonian is not analytic in this stationary point, the ESQPT classification according to Ref. [32] does not work here. Nevertheless, the observed signatures of the present ESQPT are quite similar to the case $(f, r) = (1, 1)$, which is most studied in literature, see, e.g., Refs. [18, 21, 28, 29, 47–50].

The level dynamics for two M -subspaces (including the critical one) of the $\delta = 0$ model are shown in Fig. 2. In the $M = N$ subspace we indicate two quantum phases separated by the ESQPT above $\bar{\lambda}_c$. The phase abbreviated by A (Atomic) is characterized by a growing average $\langle n^* \rangle$

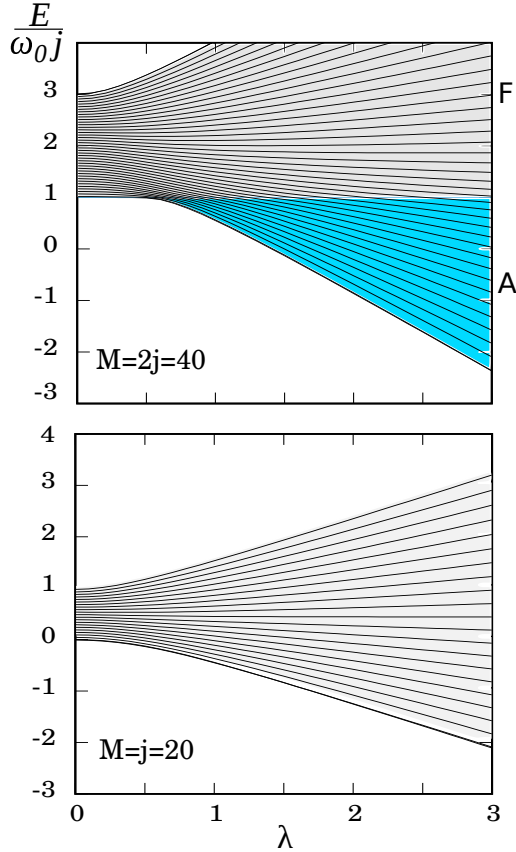


FIG. 2. (Color online) Energy spectra of two M -subspaces of the $\delta = 0$ model with $N = 2j = 40$ and $\omega_0 = \omega/2 = 1$. The upper panel shows a critical subspace $M = 2j$ with a QPT and ESQPT. Quantum phases are distinguished by colors and acronyms A (Atomic) and F (Field). The lower panel shows a non-critical subspace $M = j$.

of the number of atomic excitations in individual eigenstates with increasing energy. The average $\langle n^* \rangle$ reaches its maximum right at the ESQPT critical energy and then decreases [16], which allows us to denote the quantum phase above the ESQPT by the acronym F (Field). In this phase, the increase of energy is correlated with a growing average $\langle n \rangle$ of the number of bosons.

B. Quantum quench dynamics

Consider a quantum system with discrete energy spectrum described by a general Hamiltonian

$$\hat{H}(\lambda) = \hat{H}_0 + \lambda \hat{V} \quad (11)$$

depending linearly on a control parameter λ . As in the case of the extended Dicke model (1), the term H_0 represents a free Hamiltonian while V is an interaction. We assume $[\hat{H}_0, \hat{V}] \neq 0$ since otherwise everything would be trivial. Suppose that the system is initially prepared in the k th eigenstate $|\phi_k(\lambda_i)\rangle \equiv |\phi_{ik}\rangle \equiv |\psi_i\rangle$ with energy

$E_k(\lambda_i) \equiv E_{ik} \equiv E_i$ associated with the initial Hamiltonian $\hat{H}(\lambda_i) \equiv \hat{H}_i$, and that the control parameter is suddenly changed from λ_i to λ_f . The initial state is no more an eigenstate of the final Hamiltonian $\hat{H}(\lambda_f) \equiv \hat{H}_f$ and thus undergoes a non-trivial evolution with time t :

$$|\psi_f(t)\rangle = e^{-i\hat{H}_f t} |\psi_i\rangle, \quad (12)$$

where we assume $\hbar = 1$. The decay and recurrences of the initial state can be monitored by the survival amplitude $A(t) = \langle \psi_i | \psi_f(t) \rangle$ (here and below we assume that all states are normalized). Note that in the present setting, when the initial state is associated with a single eigenstate of the initial Hamiltonian, the survival probability $P(t) = |A(t)|^2$ is equal to the so-called Loschmidt echo or fidelity (the probability of the initial state recovery after the forward evolution by \hat{H}_f and a backward evolution by \hat{H}_i , or equivalently, the instantaneous overlap of states evolved simultaneously by \hat{H}_i and \hat{H}_f) [51–53]. However, this connection is broken for more general initial states.

Let us introduce the basis of the final Hamiltonian eigenvectors $|\phi_l(\lambda_f)\rangle \equiv |\phi_{fl}\rangle$ and the corresponding set of eigenvalues E_{fl} . The distribution of the initial state in the final Hamiltonian eigenstates is expressed by the strength function (also called the local density of states)

$$S(E) = \sum_l \frac{|\langle \psi_i | \phi_{fl} \rangle|^2}{|s_l|^2} \delta(E - E_{fl}). \quad (13)$$

It represents a probability distribution for energy after the shift $\lambda_i \rightarrow \lambda_f$, or shortly a distribution of final energy in the initial state. Besides the smoothed shape of the strength function, important information is contained also in its autocorrelation function:

$$\begin{aligned} C(E) &= \sum_l \sum_{l'} |s_l|^2 |s_{l'}|^2 \delta(E_{l'l} - E_{fl} - E) \\ &= \int dE' S(E') S(E' + E). \end{aligned} \quad (14)$$

A trivial calculation reveals that the survival probability

$$\begin{aligned} P(t) &= \left| \sum_l |s_l|^2 e^{-iE_{fl} t} \right|^2 \\ &= \underbrace{\sum_l |s_l|^4}_{\mathcal{N}^{-1}} + 2 \sum_l \sum_{l'(<l)} |s_l|^2 |s_{l'}|^2 \cos[(E_l - E_{l'})t] \end{aligned} \quad (15)$$

can be expressed via the Fourier transforms of both the strength function and its autocorrelation function:

$$P(t) = \left| \int dE S(E) e^{-iEt} \right|^2 = \int dE C(E) e^{+iEt}. \quad (16)$$

This turns out important for the interpretation of the quantum quench dynamics in various situations. Note that the quantity $\mathcal{N} = 1/\sum_l |s_l|^4$, called the participation ratio, expresses a principal number of components

of the strength function (13). It varies from $\mathcal{N} = 1$, for a perfectly localized strength function with only a single non-zero coefficient s_l , to $\mathcal{N} \rightarrow \infty$, for totally delocalized strength functions with components uniformly spread over an asymptotically increasing number of states.

The average and variance of the distribution (13) can be determined from the relation $\hat{H}_f = \hat{H}_i + \Delta\lambda \hat{V}$ (where $\Delta\lambda = \lambda_f - \lambda_i$), which follows from the linearity of Hamiltonian (11). The average is given by

$$\begin{aligned} \langle E_f \rangle_i &= \int dE S(E) E = \langle \psi_i | \hat{H}_f | \psi_i \rangle \\ &= E_i + \Delta\lambda \langle V \rangle_i, \end{aligned} \quad (17)$$

where $\langle V \rangle_i = \langle \psi_i | \hat{V} | \psi_i \rangle$, while the variance reads

$$\begin{aligned} \langle\langle E_f^2 \rangle\rangle_i &= \int dE S(E) (E - \langle E_f \rangle_i)^2 \\ &= \langle \psi_i | \hat{H}_f^2 | \psi_i \rangle - \langle \psi_i | \hat{H}_f | \psi_i \rangle^2 = (\Delta\lambda)^2 \langle\langle V^2 \rangle\rangle_i, \end{aligned} \quad (18)$$

where $\langle\langle V^2 \rangle\rangle_i = \langle \psi_i | \hat{V}^2 | \psi_i \rangle - \langle \psi_i | \hat{V} | \psi_i \rangle^2$. Due to the Hellmann-Feynman formula $\langle V \rangle_i = dE_i/d\lambda$, the relation (17) can be used to determine the final energy average, i.e., a centroid of the distribution (13), from the position and tangent of the selected energy level at the initial parameter value. This allows one to design specific quench protocols that probe selected parts of the spectrum of the final Hamiltonian, for example, different quantum phases of the system and various ESQPT critical domains [16]. However, according to Eq. (18), the final energy variance, i.e., squared width of the distribution (13), is proportional to the variance of V in the initial state and grows with the square of $\Delta\lambda$. This sets unavoidable limits to the probing procedure since the dispersion of the final energy distribution implies averaging of the response over a broader interval of the spectrum, hence reduces the resolution of the procedure.

The evolution of the survival probability on various time scales defines different regimes of the quench dynamics [12, 22, 24, 52, 53]. They are governed by physical mechanisms that naturally follow from an increasing energy resolution with which the strength function (13) is being reflected by the evolving system at the given instant of time. The regimes of quantum quench dynamics can be schematically described as follows:

(a) Ultra-short time regime, $t \ll t_s$, where

$$t_s = \frac{1}{\sqrt{\langle\langle E_f^2 \rangle\rangle_i}} \quad (19)$$

is the time derived from the final energy dispersion (18): At this time scale, the system can feel merely the width of the strength function and decays according to the simple quadratic formula $P(t) \approx 1 - (t/t_s)^2 + \dots$. This stage of evolution carries no information on the final Hamiltonian.

(b) Short- and medium-time regime, from $t \sim t_s$ up to times $t \ll t_H$ well before the Heisenberg scale set by Eq. (20) below: In this regime, the energy resolution becomes sufficient to distinguish an outline shape of the

strength function (13) as well as some of its correlation properties given by Eq. (14). Qualified estimates of the shape in various situations predict an initially exponential, Gaussian or sub-Gaussian decrease of the survival probability [12, 22]. The first dip of $P(t)$ (a ‘‘survival collapse’’) is sometimes followed by modulated oscillations with a power-law decrease of their amplitude (related for instance to low- and/or high-energy edges of the strength function) [19, 22].

(c) Long-time regime, around $t \sim t_H$: The Heisenberg time is computed according to

$$t_H = \frac{2\pi}{\sum_l \frac{1}{2} [|s_{l+1}|^2 + |s_l|^2] [E_{f(l+1)} - E_{fl}]} = \frac{2\pi}{\langle \Delta E_f \rangle_i}, \quad (20)$$

where $\langle \Delta E_f \rangle_i$ is an average spacing of the final energy levels in the initial state distribution. At this time scale, the system gradually resolves the discrete structure of the strength function, from smaller to larger level density domains. Power-law modulated oscillations can appear also at this stage, being connected with the behavior of the autocorrelation function for small energy differences [22, 54]. They may be followed by a so-called correlation hole—a long-lasting suppression of the survival probability below its asymptotic-time average, which reflects strong correlations of individual levels in chaotic systems [12, 24].

In Sec. III, we will encounter situations in which the strength function populates considerably only a certain subset of states of the final Hamiltonian. In these cases it is convenient to introduce a modified Heisenberg time t'_H that takes the partial fragmentation into account. It is computed in the same way as the standard Heisenberg time t_H in Eq. (20), but only with a reduced set of levels E_{fl} obtained by removing the states with the lowest values of $|s_l|^2$. In the numerical calculations below we select a threshold for the state removal given by 0.5% of the total strength. For partially fragmented states, t'_H gives a better prediction on where the discrete structure of the strength function starts to play a role in the quench dynamics. If the strength function is fully fragmented, t_H and t'_H tend to coincide.

(d) Ultra-long time regime, $t \gg t_H$: The infinite-time average and variance of the function $P(t)$ in Eq. (15) read

$$\overline{P(t)} = \mathcal{N}^{-1}, \quad (21)$$

$$\overline{P(t)^2} - \overline{P(t)}^2 = \mathcal{N}^{-2} - \sum_l |s_l|^8, \quad (22)$$

where bars represent time averaging of the respective quantities according to $\overline{g(t)} = \lim_{T \rightarrow \infty} \int_0^T g(t) dt / T$. So in the very long time perspective, the survival probability can be seen as fluctuations around the ‘‘saturation value’’ (21) with standard deviation given by the the square root of (22). Both these quantities decrease with the degree of fragmentation of the corresponding strength function (13). Note that for strongly delocalized states, the second term on the right-hand side of Eq. (22) gives a contribution $\sim \mathcal{N}^{-3}$, which is negligible relative to the first term,

while for localized states this term causes a considerable reduction of the variance.

Despite a usually low average (21), the ultra-long time regime unavoidably includes also sharp peaks of $P(t)$ reaching values even very close to unity. These partial revivals of the initial state demonstrate the well-known quantum recurrence theorem [55], which guarantees that for any initial state of a system with discrete spectrum and for an arbitrary degree of precision there exists a time at which the evolved state restores the initial one with this precision. As follows from Eq. (22), a higher frequency of recurrences is expected for less fragmented strength functions and vice versa.

A valuable insight into the survival probability evolution can be gained from the quasi-classical picture of quantum dynamics. Associating with the state $|\psi_f(t)\rangle$ at any stage of its evolution the Wigner phase-space distribution function $W(q, p, t)$, we can rewrite the survival probability as

$$P(t) = 2\pi \iint dq dp W(q, p, t)W(q, p, 0), \quad (23)$$

where q and p stand for f -dimensional vectors of mutually conjugate coordinates and momenta, respectively. Assume that $W(q, p, t)$ is classical-like (i.e., shows only negligible domains with negative values) or is transformed to such form by a convenient smoothing procedure $W(q, p, t) \rightarrow \bar{W}(q, p, t)$. Then the evolution can be approximated by means of the equations of motions derived from the classical Hamiltonian function $H_f(q, p)$ corresponding to \hat{H}_f .

The classical treatment of the smooth(ed) Wigner function $\bar{W}(q, p, t)$ and its evolution allows one to estimate possible signatures of classical stationary points in the survival probability $P(t)$, and therefore to partly anticipate an influence of QPTs and ESQPTs on the quench dynamics. Consider a stationary point (q_s, p_s) of the function H_f at energy $E_s = H_f(q_s, p_s)$. If E_s belongs to the support of a smoothed strength function $\bar{S}(E)$, some effects of the stationary point may be seen in $P(t)$ for $t \lesssim t_H$. The form of these effects is expected to depend on whether the stationary point (q_s, p_s) is located within the phase-space domain where the initial distribution $\bar{W}(q, p, 0)$ yields considerable contributions, or whether the stationary point is outside that domain. In the first case, the decay of the survival probability (23) gets slowed down at its initial stage, $t \lesssim t_s$, due to the slow classical dynamics around (q_s, p_s) . A clear demonstration of this behavior within the extended Dicke model will be presented in Secs. III A 1 and III B 1.

On the other hand, if the stationary point is located outside the domain with large values of $\bar{W}(q, p, 0)$, the short-time decay of $P(t)$ remains unaffected. Nevertheless, an indirect effect may be observed at some later stages of the $P(t)$ evolution, when the stationary point (q_s, p_s) prevents the return of a certain fraction of the $\bar{W}(q, p, t)$ distribution (that with energy close to E_s) back to the initial phase-space domain. Then we may expect

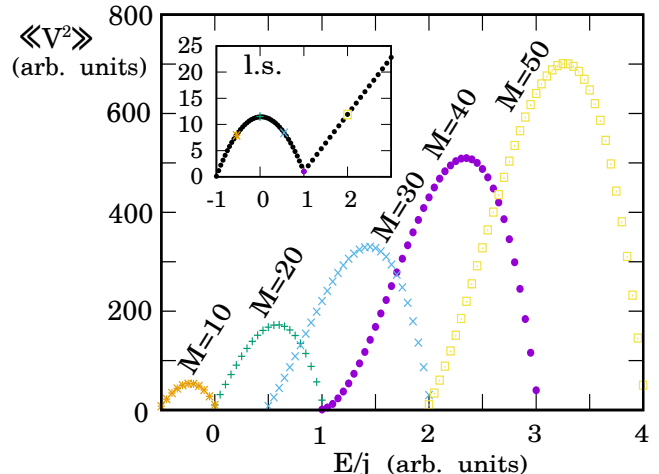


FIG. 3. (Color online) Dispersion $\langle\langle V^2 \rangle\rangle_i$ from Eq. (24) in the unperturbed eigenstates $|\psi_i\rangle = |n\rangle|m\rangle$ of the $\delta = 0$ model plotted against their energies. Parameters of the system are $\omega = 2, \omega_0 = 1, j = 20$. The inset shows $\langle\langle V^2 \rangle\rangle_i$ in the lowest states from all M -subspaces. The states involved in the main panel are marked in the inset by the respective symbols.

a partial reduction of the survival probability $P(t)$ for times comparable with the Heisenberg scale, $t \sim t_H$, which coincides with an average classical return time. Indications of such behavior will be indeed discussed in Secs. III A 2 and III B 2, but we stress here that the reduction size (the possibility to actually observe any effect) strongly depends on the degree of stability (chaos) of classical motions generated by $H_f(q, p)$ in the relevant phase-space domain.

III. NUMERICAL RESULTS

In this section, numerical results on the quantum quench dynamics in the extended Dicke model with Hamiltonian (1) will be analyzed. Subsection III A deals with the quenches in M -subspaces of the integrable $\delta = 0$ (Tavis-Cummings) regime where the dynamics is effectively reduced to one degree of freedom. Subsection III B is focused on the quenches in the full $\delta \neq 0$ model with two degrees of freedom.

A. Integrable $\delta = 0$ regime

1. Forward quench protocols, $f = 1$

The evolution of the survival probability strongly depends on the quench protocol, that is on the selection of the initial state and on the size of the parameter change. In the forward quench protocols (FQPs) we set initial states as various eigenstates of the unperturbed $\lambda_i = 0$ Hamiltonian and choose the final value $\lambda_f > 0$.

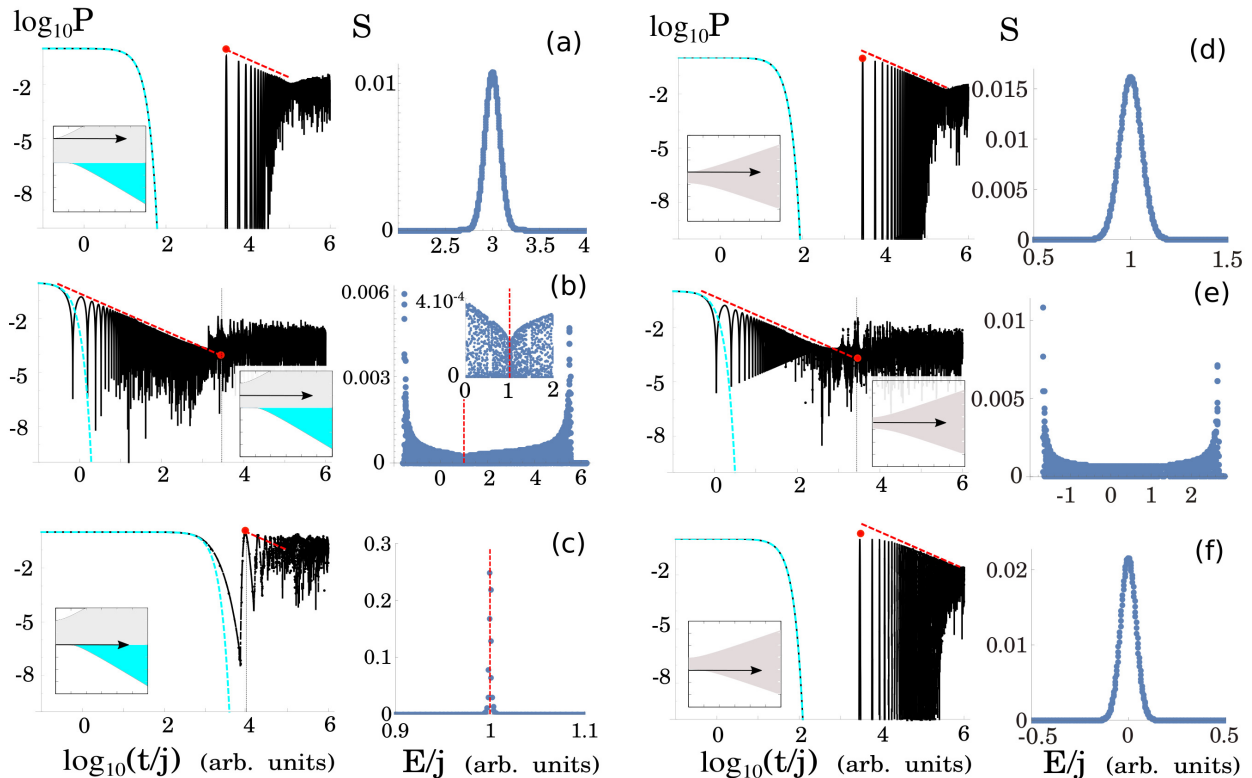


FIG. 4. (Color online) The survival probability and the strength function corresponding to the FQPs of the $\delta = 0$ model with $j = 2000$ in off-resonant setting $\omega = 2, \omega_0 = 1$. The critical $M = 2j$ subspace is shown in panels (a)–(c), a non-critical $M = j$ subspace in panels (d)–(f). In all the cases, $\lambda_i = 0$ and $\lambda_f = 2.5$ (the quench protocol is visualized by an arrow in the respective phase diagram). The real decay (black curves) is compared with the Gaussian decay (the light-blue dashed curves), the Heisenberg time t_H is marked with the red bullets, and the $1/t$ decay of oscillations is marked with the red dashed lines. In the strength function plots, the position of the ESQPT is indicated by vertical lines.

The decay rate at ultra-short and short times of such initial states can be estimated using Eqs. (18) and (19). In the detuned system $\omega \neq \omega_0$ (the initial eigenstates are non-degenerate, hence $|\psi_i\rangle = |n\rangle|m\rangle$), a simple formula for the dispersion of the interaction Hamiltonian term can be obtained:

$$\langle\langle V^2 \rangle\rangle_i = \frac{(1 + \delta^2)(j^2 - m^2 + j)(2n + 1) + (1 - \delta^2)m}{2j}. \quad (24)$$

In Fig. 3 we show $\langle\langle V^2 \rangle\rangle_i$ in multiple eigenstates belonging to several M -subspaces for $j = 20$. For all the subspaces we observe a similar dependence—the states closer to the edges of the spectrum have smaller dispersion than the ones in the middle and therefore their decay is slower. However, a closer look reveals an anomaly for the critical subspace $M = 2j = 40$. The inset of Fig. 3 depicts the dispersion of the lowest state from all subspaces with $M = 0, 1, 2, \dots$, plotted against their energies $E_{l,s}(M) = \omega(M - j) - (\omega - \omega_0)j$. The leftmost point corresponding to the global ground state has $\langle\langle V^2 \rangle\rangle_i = 0$. Indeed, as it is the only member of the $M = 0$ subspace it cannot decay. However, small values of dispersion are reached also for the M -subspaces close to the critical one with

$\langle\langle V^2 \rangle\rangle_i = 1/2j$, which indicates an asymptotically slow decay of the respective initial states in the $j \rightarrow \infty$ limit.

Let us now proceed to concrete examples of FQPs within two M -subspaces, the critical one with $M = 2j$ and the non-critical with $M = j$. In the following we consider $j = 2000$. Fig. 4 depicts both the survival probability and the strength function for several initial states from the above mentioned subspaces.

In the first row of Fig. 4 (panels a and d) we compare the highest excited states. The envelope of the strength function has a Gaussian shape, giving rise to an initial Gaussian decay of the survival probability [22]. After the initial decay, strong revivals appear at about the Heisenberg time t_H . Their amplitude decreases as $\propto 1/t$ until the saturation regime around $P(t) \sim \mathcal{N}^{-1}$ is reached. The power-law modulation $\propto 1/t^\alpha$ of the oscillations with various exponents α was observed in various systems and has been attributed to several specific mechanisms [19, 22, 54]. The present case $\alpha = 1$ results from two conditions: an approximately Gaussian envelope of the strength function and its discrete energy sampling

$$E_{fl} \approx e_0 + e_1 l + e_2 l^2 \quad (25)$$

with parameters e_0, e_1 and $e_2 \neq 0$ satisfying $|e_2| \ll |e_1|$ [54]. As can be numerically checked, both these conditions are valid in our case.

In the second row of Fig. 4 (panels b and e) we compare the decay of $\lambda_i = 0$ initial states from the middle of $M = 2j$ and $M = j$ spectra. In both cases, the strength function has a bimodal shape with large dispersion. As a result, the initial decay is faster than Gaussian. We again observe $\propto 1/t$ modulated oscillations, but *before* the Heisenberg time t_H . In this case, the origin of the power-law dependence lies purely in the profile of the strength function, namely in its U-shaped envelope. Although the ESQPT does not visibly affect the survival probability, the inset of panel (b) shows that the strength function forms a small dip at the critical energy.

Finally, the last row of Fig. 4 (panels c and f) depicts FQPs with the lowest states from both $M = 2j$ and $M = j$ subspaces. Panel (c) shows the critical quench—the initial ground state is displaced directly into the region of ESQPT between the A and F phases at energy E_{c4} (see the phase diagram inset). The initial decay is significantly slowed down (even slower than the Gaussian decay). Semiclassically this can be viewed as a slowdown of the dynamics due to the localization of the initial state at the stationary point (q_s, p_s) of the final Hamiltonian, see the end of Sec. II B. A very narrow strength function indicates a high localization of the initial state in the final eigenbasis. As the Gaussian envelope is lost, we do not observe any power-law modulated oscillations around the Heisenberg time. On the other hand, in the non-critical subspace (panel f) we obtain a similar decay pattern as for the highest excited state (panel d), manifesting that the presence of an ESQPT is crucial for the existence of the localization. The stabilization of the initial state due to an ESQPT within a similar quench protocols in different $f = 1$ systems was also studied in Refs. [21, 24].

2. Backward quench protocols, $f = 1$

In the backward quench protocols (BQPs), we set λ_i above the critical value (in this case λ_c) and choose various values of $\lambda_f < \lambda_i$ [16]. In Fig. 5 we consider the initial ground state at $\lambda_i = 2.5$. The survival probabilities and strength functions for $\lambda_f = 0.5$ (panel a), $\lambda_f = 0.8$ (panel c) and $\lambda_f = 1$ (panel d) are qualitatively similar to those in panels (a), (d) and (f) of Fig. 4. However, the quench with $\lambda_f = 0.772$ in panel (b) of Fig. 5 has a different character.

The quench in Fig. 5(b) is critical in the sense that its final state population is centered roughly at the ESQPT energy E_{c4} . We see that the corresponding strength function has a bimodal form with a dip at the critical energy. Note that a similar behavior [see also Fig. 4(b)] would be observed for quenches within a certain interval around the present value of λ_f . The initial decay of the survival probability after the critical quench does not differ from the other cases in Fig. 5, but the $\propto 1/t$ dependence of

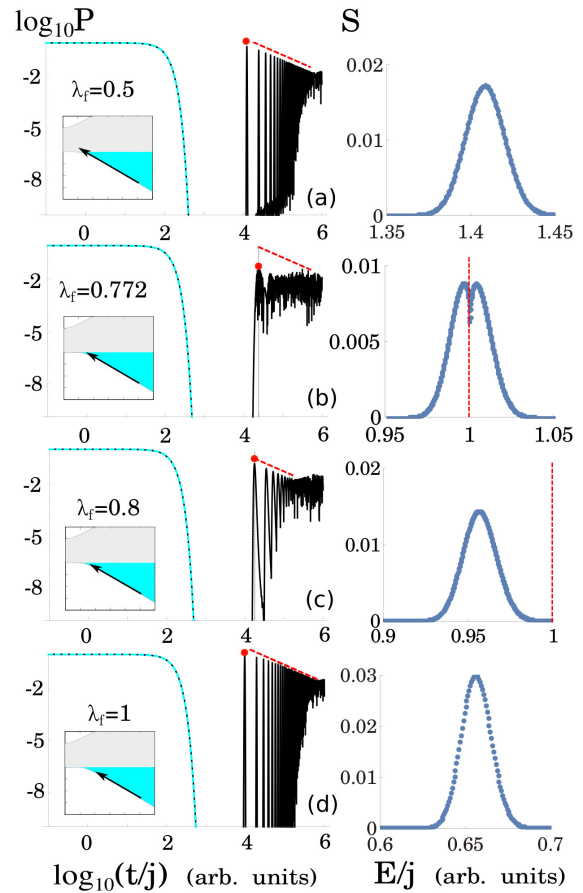


FIG. 5. (Color online) The survival probability and the strength function corresponding to the BQPs in the critical $M = 2j$ subspace of the $\delta = 0$ model. The parameters and meaning of symbols are the same as in Fig. 4.

revivals after the Heisenberg time is not present. The evolution of the survival probability gets to the saturation regime right after the survival collapse, which can be interpreted as a speed-up of the decay. This difference from the FQP case, where the ESQPT caused a longer survival, demonstrates that the quench protocol (the choice of the initial state) plays an important role for the ESQPT-induced effects.

The reason for absence of the $1/t$ behavior lies in the violation of formula (25) for quenches populating states across the ESQPT. This is demonstrated in Fig. 6, where correlations between the energy spacings $E_{fl} - E_{f(l-1)}$ and the mean populations $(|s_l|^2 + |s_{l-1}|^2)/2$ of the respective neighboring levels are visualized for quenches from panels (a) and (b) of Fig. 5. The left column in Fig. 6 shows the energy spacing as a function of l , with the mean populations marked by sizes of the green dots. The right column depicts the energy spacing versus the mean population. In the upper row of Fig. 6, which corresponds to the non-critical quench, we see that the energy spacing is approximately a linear function of l , in agreement with

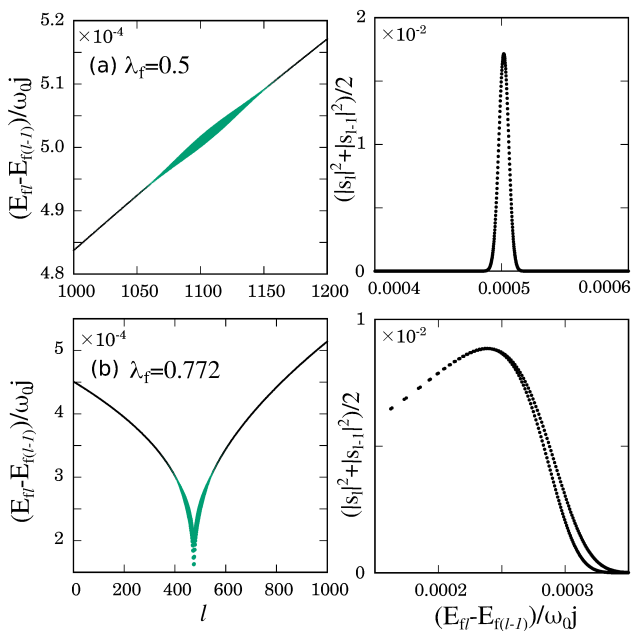


FIG. 6. (Color online) Distributions of the the energy spacing between neighboring levels of the final Hamiltonian after the quenches from panels (a) and (b) of Fig. 5. Left graphs show the dependence of the energy spacing on the level index l . The green dots mark the levels populated in the quench—the dot area is proportional to the mean size of the strength function in the respective pair of levels. The plots on the right display the level spacings correlated with the mean sizes of the strength function. The critical quench in the lower row yields dependences with two distinct branches.

Eq. (25), which leads to a sharply peaked distribution of energy spacings in the populated ensemble of levels. In contrast, for the critical quench in the lower row both dependences exhibit two distinct branches. These are associated with the states below and above the critical energy E_{c4} , where the spacing vanishes.

From the semiclassical viewpoint, the suppression of the power-law oscillations for the critical quench in Fig. 5(b) can be attributed to some peculiar features of the long-time dynamics of the phase-space distribution associated with the evolving quantum state—see the discussion at the end of Sec. II B. As the global minimum (q_0, p_0) of the initial Hamiltonian $H_i(q, p)$ is far from the $E = E_{c4}$ stationary point (q_s, p_s) of the final Hamiltonian $H_f(q, p)$, the support of the initial state's Wigner function localized around (q_0, p_0) does not considerably overlap with (q_s, p_s) . Therefore, the latter stationary point does not affect the short time decay of the initial state but only its recurrences at the $t \sim t_H$ time scale.

In Fig. 7 we compare the BQPs in both critical and non-critical subspaces by plotting the Heisenberg time t_H and the participation ratio \mathcal{N} as a function of λ_f . We see that both t_H and \mathcal{N} have a sharp maximum at the critical quench in panel (a) while the non-critical dependences

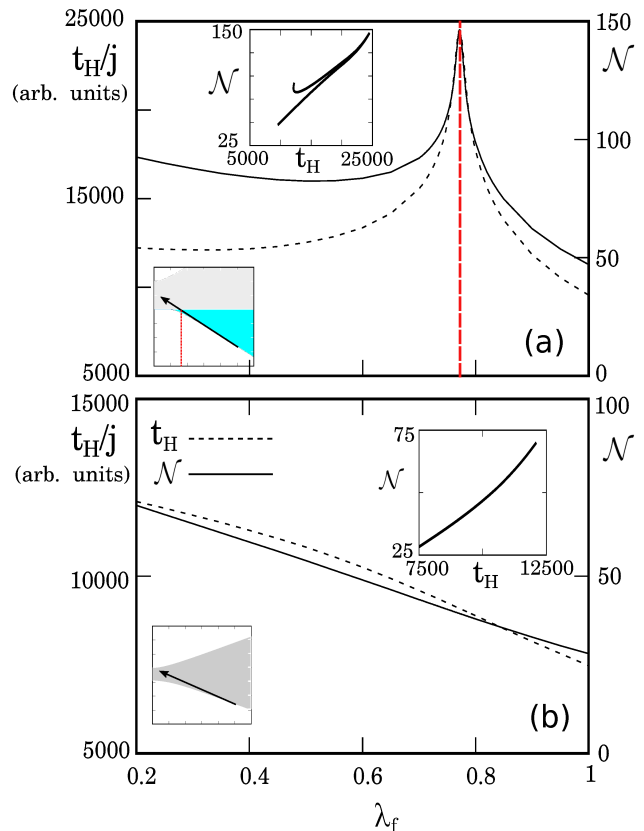


FIG. 7. (Color online) The Heisenberg time t_H and participation ratio \mathcal{N} for BQPs from $\lambda_i = 2.5$ to various values of λ_f in the critical $M = 2j$ (panel a) and non-critical $M = j$ (panel b) subspaces of the $\delta = 0$ model. The parameters are the same as in Fig. 4. The critical quench in panel (a) is marked with vertical line. The insets above the curves show the correlation between the quantities t_H and \mathcal{N} .

in panel (b) are smooth and monotonous. This can be qualitatively understood as follows: Given a smoothed strength function $\bar{S}(E)$ and smoothed density of states $\bar{\rho}_f(E)$ of the final Hamiltonian (where smoothing means elimination of δ -functions by a local averaging), the inverse participation ratio can be approximated by

$$\mathcal{N}^{-1} \approx \int dE \bar{\rho}_f(E)^{-1} \bar{S}(E)^2. \quad (26)$$

Assuming now (i) a Gaussian shape of $\bar{S}(E)$ with an average $\langle E_f \rangle_i$ and variance $\langle \langle E_f^2 \rangle \rangle_i$, and (ii) an analytic energy dependence of the inverse level density $\bar{\rho}_f(E)^{-1} = d_0 + d_1 E + d_2 E^2 + \dots$ (where d_0, d_1, d_2, \dots are some coefficients), we obtain the formula

$$\mathcal{N}^{-1} \approx \frac{d_0 + d_1 \langle E_f \rangle_i + d_2 \langle \langle E_f^2 \rangle \rangle_i / 2 + \dots}{2\sqrt{\pi} \langle \langle E_f^2 \rangle \rangle_i}, \quad (27)$$

which can be further transformed to the form depending on the parameter shift $\Delta\lambda$ by inserting expressions from

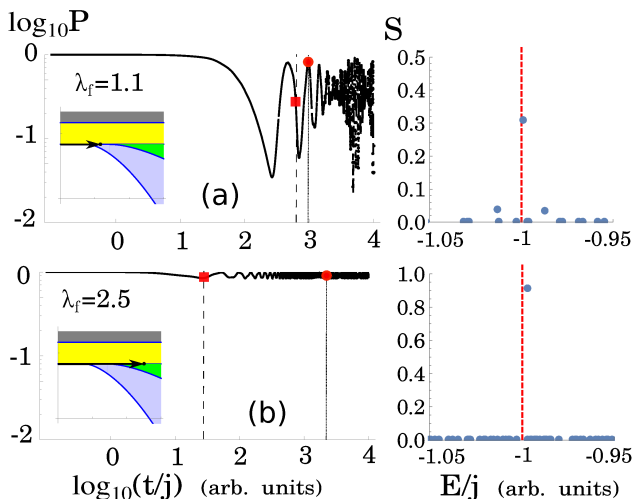


FIG. 8. (Color online) The survival probability and the strength function corresponding to the FQPs from the $\lambda_i = 0$ ground state of the $\delta = 0.3$ model with parameters $j = 20$, $\omega = \omega_0 = 1$ in the even parity sector. The standard and modified Heisenberg times t_H and t'_H are marked with the red bullet and square, respectively.

Eqs. (17) and (18). If $|d_0| \gg |d_1|, |d_2|, \dots$, the participation ratio \mathcal{N} becomes roughly proportional to $|\Delta\lambda|$, which is exactly the behavior observed in panel (b) of Fig. 7. On the other hand, the critical dependence of \mathcal{N} shown in panel (a) is a consequence of the violation of both the above conditions (i) and (ii) for the quenches populating states across the ESQPT. Note also that the divergence of the Heisenberg time t_H at the critical λ_f can be deduced from the dependences in Fig. 6(b).

B. General $\delta \neq 0$ regime

1. Forward quench protocols, $f = 2$

We now proceed to study the quench dynamics in a general $\delta \neq 0$ model with two degrees of freedom. We set the model parameter $\delta = 0.3$ and tune the system to resonance $\omega = \omega_0 = 1$. In contrast to the integrable case, we consider only the initial states associated with the ground state of H_i . In the FQPs, we choose the ground state at $\lambda_i = 0$ and perform a quench to $\lambda_f = 1.1$ and $\lambda_f = 2.5$, see Fig. 8. These values were selected because we want to test different types of ESQPTs (see the insets in the respective figure). Indeed, for $\lambda_f = 1.1$ the strength function is centered at the $(f, r) = (2, 1)$ ESQPT critical energy E_{c1} between the D and N phases. On the other hand, for $\lambda_f = 2.5$ the strength function is localized at the $(f, r) = (2, 2)$ ESQPT critical energy E_{c2} between the TC and N phases.

Panel (a) of Fig. 8 presents a similar decay pattern as the integrable case in Fig. 4(c). We again observe that the

strength function has only a few non-zero components in the vicinity of the ESQPT energy, indicating a rather high level of localization of the initial state in the final eigenbasis. However, if we increase the final parameter value to $\lambda_f = 2.5$, the localization becomes nearly perfect, see Fig. 8(b). Indeed, the $\lambda_i = 0$ ground state has a 96% overlap with the $\lambda_f = 2.5$ eigenstate closest to the ESQPT. This difference between D-N and TC-N phase borderlines has been pointed out in Ref. [41]. As a consequence, in the long-time regime the survival probability in Fig. 8(b) oscillates around a quite high value $P \approx 0.85$. Note that the onset of oscillations neatly coincides with the modified Heisenberg time t'_H (see Sec. IIB), which is marked with the red square and the vertical dashed line.

2. Backward quench protocols, $f = 2$

Using the same setting of the model, we employ BQPs starting from the superradiant ground state at $\lambda_i = 6 > \lambda_c$. There are several ESQPTs to be probed in this way. In Fig. 9, results for several values of λ_f are depicted. We observe an initial Gaussian decay in all cases. Further, we can see that the first revival appears roughly around the modified Heisenberg time t'_H . These revivals decay in most cases as $1/t$. Apparently, this behavior of the revivals is also present in the $\lambda_f = 3.1$ critical quench probing the $(f, r) = (2, 2)$ ESQPT between the TC and N phases at $E = E_{c2}$ (the same type of ESQPT between the N and S phases at $E = E_{c3}$ was also examined, showing the same result). However, if we choose $\lambda_f \doteq 3.27$, corresponding to critical quench to the $(f, r) = (2, 1)$ ESQPT between the D and TC phases at $E = E_{c1}$, we observe the vanishing of the $1/t$ modulated revivals. This is again due to the splitting of the strength function at the critical energy—a similar effect as in the $f = 1$ critical case, compare Fig. 9(d) with Fig. 5(b).

All the strength functions in Fig. 9 have a common property that their support is only a certain subset of the final Hamiltonian spectrum (see the zero base corresponding to levels which are virtually unpopulated). This can be interpreted so that the system is in a quasi-regular regime where the overlap with only some selected final states is allowed. So the modified Heisenberg time t'_H , restricted only on these states, agrees better with the onset of revivals.

The quasi-regularity of the populated final states is illustrated in Fig. 10 where we present a so-called Peres lattice [56] of the final Hamiltonian. The Peres lattice depicts the spectrum of eigenstates as a mesh of points in the plane $E_l \times \langle O \rangle_l$, where E_l is energy and $\langle O \rangle_l$ an expectation value of a certain observable (here the number of photons) in the l th eigenstate. Orderly arranged points in the lattice indicate regularity of the respective eigenstates whereas disordered points imply chaoticity of eigenstates [57]. The states populated in the critical quench from Fig. 9(d) are displayed by the highlighted dots, the size of each dot corresponds to the value $|s_l|^2$ of

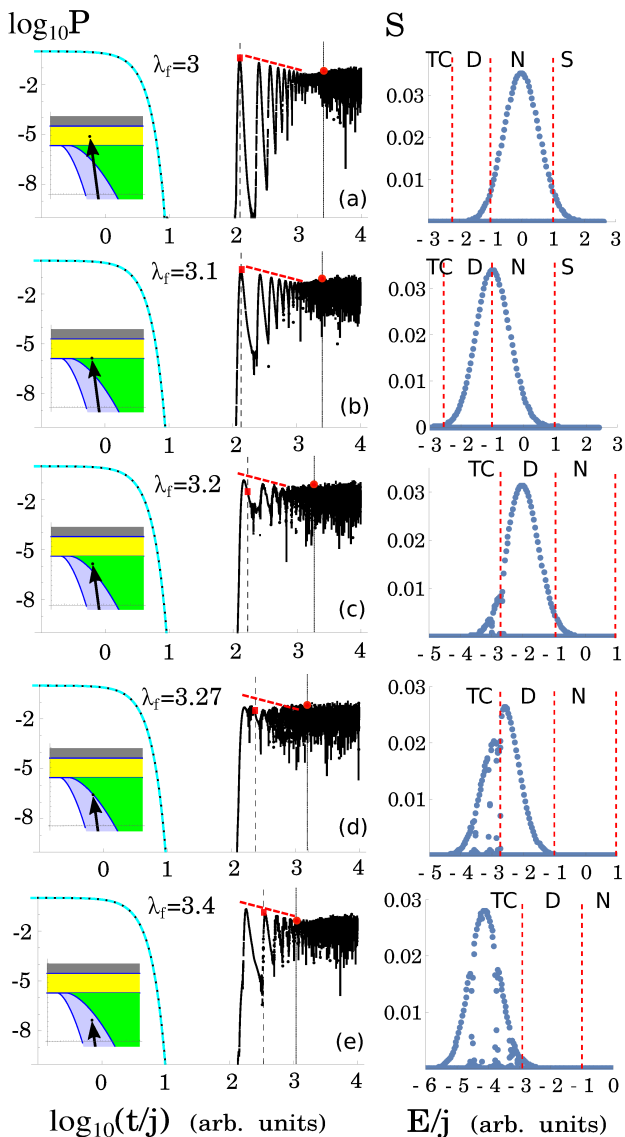


FIG. 9. (Color online) The survival probability and the strength function corresponding to the BQPs from the $\lambda_i = 6$ ground state of the $\delta = 0.3$ model with parameters $j = 20$, $\omega = \omega_0 = 1$ in the even parity sector. The standard and modified Heisenberg times t_H and t'_H are depicted with the red bullet and square, respectively. The $1/t$ decay of oscillations is marked with the red dashed lines.

the strength function. We observe a localization of the populated states in the regular domain. The same is true for the other quenches in Fig. 9.

In Fig. 11, the modified Heisenberg time t'_H and the participation ratio \mathcal{N} are plotted for several values of λ_f . Both dependences show maxima close to the critical value $\lambda_f = 3.27$, in a rough correspondence to the BQPs for $f = 1$ critical system (cf. Fig. 7). Note that the other critical value $\lambda_f = 3.1$ induces no effect.

If we increase the parameter δ , the overall degree of

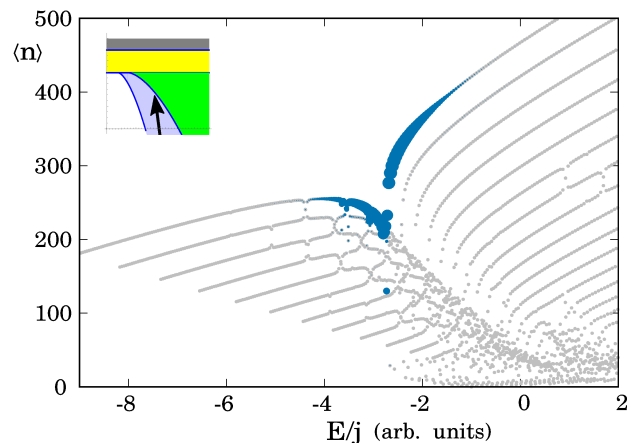


FIG. 10. (Color online) The Peres lattice with the average number of photons $\langle n \rangle$ for the $\lambda = 3.27$, $\delta = 0.3$ Hamiltonian (the same parameters as in Fig. 9). The strength function from Fig. 9(d) is displayed by blue dots, the dot area encodes the respective $|s_l|^2$ value.

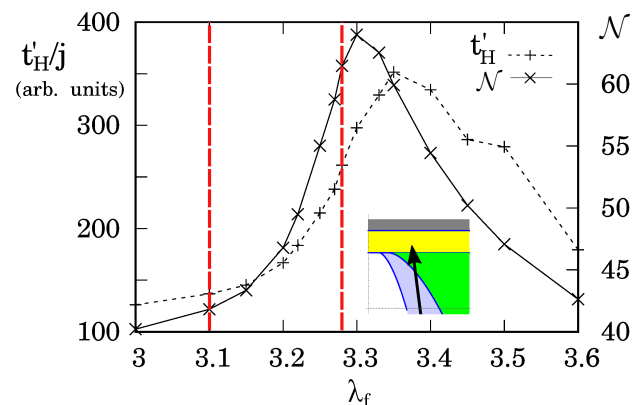


FIG. 11. (Color online) The modified Heisenberg time t'_H and the participation ratio \mathcal{N} for the BQPs in the $\delta = 0.3$ model with the $\lambda_i = 6$ ground state. The parameters are the same as in Fig. 9. The critical quenches are marked with vertical lines. Lines connecting points serve as guides for eyes.

chaoticity involved in the model grows. Let us move on to probing the quench dynamics in the full Dicke model with $\delta = 1$. In Fig. 12, the survival probability is shown along with the respective strength function for several BQPs from the $\lambda_i = 4$ ground state. As λ_f we choose three values, with $\lambda_f = 2.06$ (panel b) corresponding to the critical quench to the $(f, r,) = (2, 1)$ ESQPT between the D and N phases at $E = E_{c1}$.

As in Fig. 9, the initial decay for the quenches in Fig. 12 is Gaussian. The revivals after the survival collapse can be partially fitted by the $1/t$ envelope in panel (c) whereas in panel (b) the oscillations are weakened and in panel (a) they are not present at all. This follows from the fact that

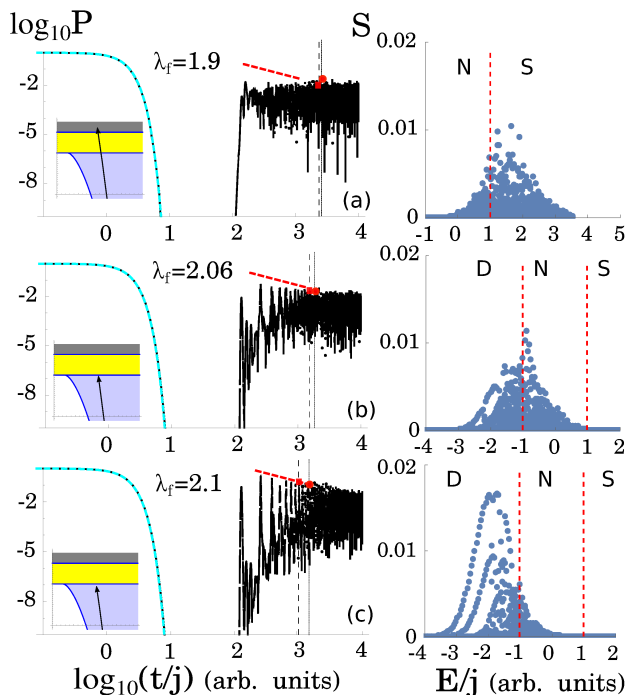


FIG. 12. (Color online) The survival probability and the strength function corresponding to the BQPs from $\lambda_i = 4$ ground state of the $\delta = 1$ model. The settings and symbols are the same as in Fig. 9.

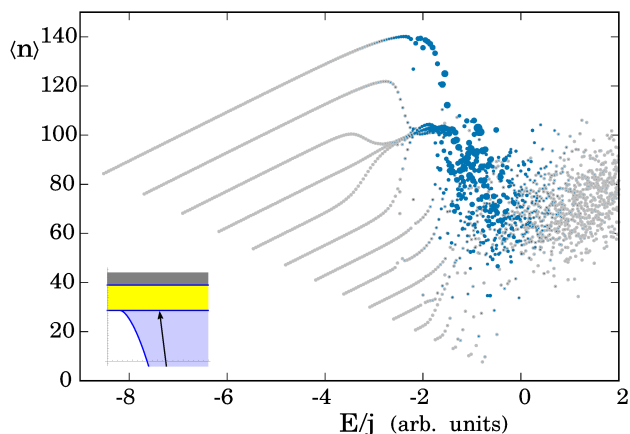


FIG. 13. (Color online) The Peres lattice as in Fig. 10 but for the $\lambda = 2.06$, $\delta = 1$ Hamiltonian. The strength function from Fig. 12(b) is depicted by blue dots.

the corresponding strength functions have much more complex structure than those for $\delta = 0.3$. It is shown in Ref. [54] that if the strength function consists of several embedded Gaussian profiles—a clear example is panel (c) of Fig. 12—the interference terms in the survival probability distort the power-law decay.

The growing complexity of the strength function indi-

cates a higher number of final eigenstates with non-zero $|s_l|^2$. In Fig. 13 we show the Peres lattice of the final spectrum for the critical quench $\lambda_f = 2.06$ with the strength function encoded in the size of blue points. We observe that the initial state is distributed mainly in the chaotic part of the spectrum. This is a radically different situation than for the critical quench to the same ESQPT type with $\delta = 0.3$, cf. Fig. 10. Apparently, quantum chaos plays a dominant role in the presently observed disappearance of the power-law modulated revivals at $t \sim t_H$, smearing possible ESQPT effects. Anyway, in Fig. 12(b) the presence of the ESQPT between D and N phases is still captured by a partially bimodal form of the critical strength function.

We now attempt to identify some ESQPT-induced effects in the evolution of suitably selected physical observables. In particular, we look at the number of bosons $\hat{n} = \hat{b}^\dagger \hat{b}$, whose average $\langle n \rangle$ is directly related to the photon flux leaving the cavity in the experimental setup described in Ref. [5]. The evolution of this quantity after the quench can be computed as

$$\langle n \rangle = \sum_l |s_l|^2 n_{ll} + 2 \sum_{l > l'} \text{Re} \left[s_l s_{l'}^* e^{i(E_{ll} - E_{l'l'})t} \right] n_{ll'}, \quad (28)$$

where $n_{ll'} = \langle \phi_{ll} | \hat{n} | \phi_{l'l'} \rangle$.

In Fig. 14 we present results for the above-described BQPs in the $\delta = 0.3$ and $\delta = 1$ versions of the model. The $\delta = 0.3$ case with $\lambda_i = 6$ is depicted in panels (a)–(c). The results are qualitatively similar as in the time evolution of the survival probability, cf. Fig. 9. In non-critical cases, panels (a) and (c) in Fig. 14, the oscillations appear after the initial decay. These are further attenuated, so $\langle n \rangle$ reaches its saturation value given simply by the first term in Eq. (28). In panel (b), which corresponds to the critical quench, the oscillatory part of the evolution is suppressed and the saturation regime is reached sooner. In other words, the time evolution of this observable captures the presence of ESQPTs in the same way as the survival probability.

The time dependence of $\langle n \rangle$ after the BQPs in the $\delta = 1$ Dicke model with $\lambda_i = 4$ is plotted in panels (d)–(f) of Fig. 14. The critical quench is shown in panel (e). In analogy to the above described behavior of the survival probability for the same quench protocols, the ESQPT effect in $\langle n \rangle$ is suppressed due to a high degree of chaoticity of the populated eigenstates of the final Hamiltonian.

IV. SUMMARY

We employed various types of quantum quench protocols in multiple settings of the extended Dicke model with the aim to test dynamical signatures of ESQPTs. Although the information in the time signal is often lost, effects of ESQPTs can be observed in the strength function which is an inverse Fourier transform of the survival probability. Nevertheless, in the protocols involving the

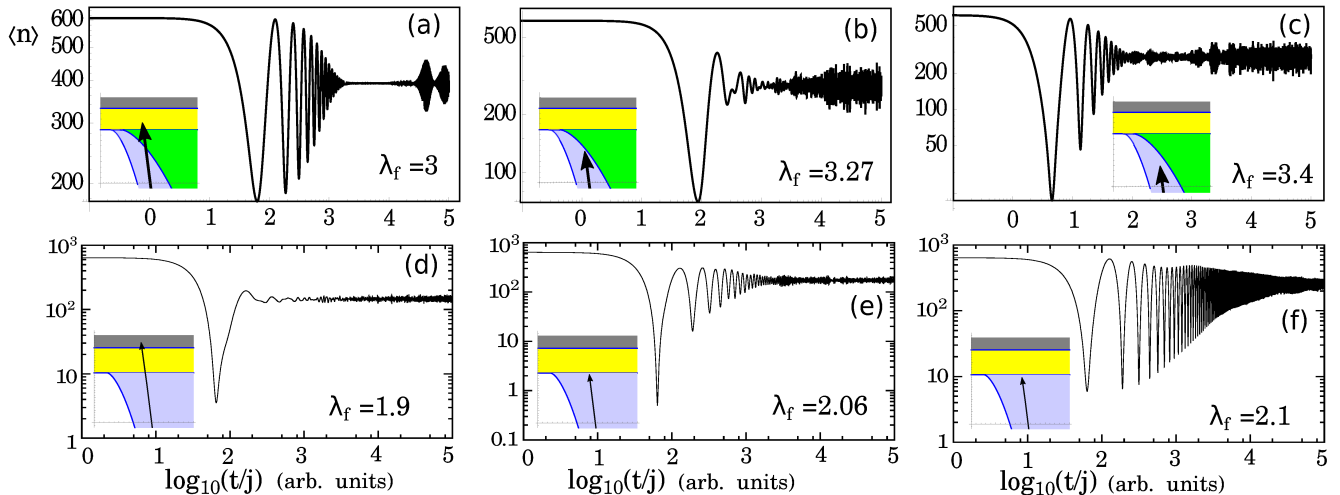


FIG. 14. (Color online) The time evolution of the average number of photons in the cavity $\langle n \rangle$ after the BQPs from the initial ground state. Panels (a)–(c) correspond to the $\delta = 0.3$ model with $\lambda_i = 6$ (the same quenches as in Fig 9). Panels (d)–(f) correspond to the $\delta = 1$ model with $\lambda_i = 4$ (the same quenches as in Fig 12). Other parameters are as in Fig. 9.

ground states of the initial Hamiltonians, the effect is often visible even in the time dependences. We observed essentially two types of effects: either the stabilization of the initial state, or a speed-up of its decay.

In the context of the present model, the ESQPT-induced stabilization was observed in the class of forward quench protocols with $\Delta\lambda > 0$. It appears because the final Hamiltonian has a stationary point at the place of the initial Hamiltonian's global minimum. In our model, the stationary point is stable below the critical coupling (λ_c or $\bar{\lambda}_c$) and unstable above (hence inducing an ESQPT). We examined three different cases:

- Integrable $\delta = 0$ model in its critical $M = 2j$ subspace. The unstable stationary point affecting the quenches with $\lambda_f \in (\bar{\lambda}_c, \infty)$ leads to the logarithmic divergence of the level density as in an ESQPT of the type $(f, r) = (1, 1)$. The stabilization effect was seen in Fig. 4(c).
- Non-integrable $\delta \in (0, 1]$ model. The unstable stationary point affecting quenches with $\lambda_f \in (\lambda_c, \lambda_0)$ constitutes an ESQPT with $(f, r) = (2, 1)$. The quench dynamics was shown in Fig. 8(a).
- Non-integrable $\delta \in (0, 1)$ model. The unstable stationary point affecting quenches with $\lambda_f \in [\lambda_0, \infty)$ constitutes an ESQPT with $(f, r) = (2, 2)$. In this case we observed even stronger stabilization due to nearly perfect localization of the strength function, see Fig. 8(b).

On the contrary, the ESQPT-induced speed-up of the decay of the initial state was observed in some backward quench protocols. The initial parameter value λ_i was chosen above the critical coupling (λ_c or $\bar{\lambda}_c$) and the parameter shift $\Delta\lambda < 0$ was set such that the strength function was centered at the ESQPT energy. The speed-up is

manifested as a disappearance or considerable suppression of the power-law stage of the quench dynamics at long time scales. The effect was clear in the following cases:

- Integrable $\delta = 0$ model in its critical $M = 2j$ subspace, see Fig. 5(b).
- Non-integrable $\delta \in (0, 1)$ model for quenches to the $(f, r) = (2, 1)$ ESQPT separating the D and TC phases, see Fig. 9(d).

The presence of the power-law decay at long time scales in the non-critical quenches is due to a combination of (a) Gaussian envelope of the strength function and (b) discrete sampling of the strength function with a quadratic variation of the level spacings. For the above specified critical quenches, this interplay is violated because of different quadratic dependences of level spacings on both sides of the ESQPT, see Fig. 6 that depicts the situation in the $\delta = 0$ model. Note that in both these cases the Heisenberg time (either t_H or t'_H) and the participation ratio \mathcal{N} locally increase, see Figs. 7 and 11.

The suppression of the power-law stage of the quench dynamic is not observed for quenches to ESQPTs of the type $(f, r) = (2, 2)$. Moreover, in the $\delta = 1$ model, the speed-up effect disappears even for $(f, r) = (2, 1)$ ESQPT. This is because the support of the strength function lies in the chaotic part of the final spectrum, cf. Figs. 10 and 13.

We have demonstrated that similar effects as in the survival probability can be detected in observables like the average photon number in the cavity. As seen in Fig. 14 this quantity shows a disappearance of the medium-time oscillations for critical quenches to the $(f, r) = (2, 1)$ ESQPT in $\delta \in (0, 1)$ model. This may suggest a way of experimental verification of ESQPT-related effects within

a cold atom realization of the Dicke-like systems.

V. ACKNOWLEDGEMENT

We acknowledge funding of the Charles University under project UNCE/SCI/013.

-
- [1] C. Gardiner, P. Zoller, *The Quantum World of Ultra-Cold Atoms and Light*, Books I, II and III (Imperial College Press, London, 2014, 2015, 2016).
- [2] I. M. Georgescu, S. Ashhab and F. Nori, *Rev. Mod. Phys.* **86**, 153 (2014).
- [3] A. Gheorghiu, T. Kapourniotis and E. Kashefi, arXiv:1709.06984 [quant-ph] (2017).
- [4] M. Greiner *et al.*, *Nature (London)* **415**, 39 (2002); **419**, 51 (2002).
- [5] K. Baumann *et al.*, *Nature* **464**, 1301 (2010); *Phys. Rev. Lett.* **107**, 140402 (2011).
- [6] J. Klinder *et al.*, *Proc. Nat. Acad. Sci.* **112**, 3290 (2015).
- [7] A. Polkovnikov *et al.*, *Rev. Mod. Phys.* **83**, 863 (2011).
- [8] J. Eisert, M. Friesdorf and C. Gogolin, *Nature Phys.* **11**, 124 (2015).
- [9] K. Sengupta, S. Powell and S. Sachdev *Phys. Rev. A* **69**, 053616 (2004).
- [10] P. Calabrese and J. Cardy, *Phys. Rev. Lett.* **96**, 136801 (2006).
- [11] A. Silva, *Phys. Rev. Lett* **101**, 120603 (2008).
- [12] F. Borgonovi *et al.*, *Phys. Rep.* **626**, 1 (2016).
- [13] M. Cramer *et al.*, *Phys. Rev. Lett.* **100**, 030602 (2008).
- [14] C. De Grandi, V. Gritsev and A. Polkovnikov, *Phys. Rev. B* **81**, 012303 (2010).
- [15] L. Campos Venuti and P. Zanardi, *Phys. Rev. A* **81**, 032113 (2010); *Phys. Rev. E* **89**, 022101 (2014).
- [16] P. Pérez-Fernández *et al.*, *Phys. Rev. A* **83**, 033802 (2011).
- [17] S. Montes and A. Hamma, *Phys. Rev. E* **86**, 021101 (2012).
- [18] L.F. Santos and F. Pérez-Bernal, *Phys. Rev. A* **92**, 050101(R) (2015); L.F. Santos, M. Távora and F. Pérez-Bernal, *Phys. Rev. A* **94**, 012113 (2016).
- [19] M. Távora, E.J. Torres-Herrera and L.F. Santos, *Phys. Rev. A* **94**, 041603(R) (2016).
- [20] R. Jafari and H. Johannesson, *Phys. Rev. Lett.* **118**, 015701 (2017).
- [21] F. Pérez-Bernal and L.F. Santos, *Fortschr. Phys.* **65**, 1600035 (2017).
- [22] M. Távora, E.J. Torres-Herrera and L.F. Santos, *Phys. Rev. A* **95**, 013604 (2017).
- [23] M. Heyl, *Rep. Prog. Phys.* **81**, 054001 (2018).
- [24] E. J. Torres-Herrera, A. M. García-García, L. F. Santos, *Phys. Rev. B* **97**, 060303(R) (2018).
- [25] A. Mitra, *Annu. Rev. Condens. Matter Phys.* **9**, 245 (2018).
- [26] S. Sachdev, *Quantum Phase Transitions* (Cambridge Univ. Press, Cambridge, 2011).
- [27] *Understanding Quantum Phase Transitions*, edited by L.D. Carr (CRC, Boca Raton, 2011).
- [28] P. Cejnar *et al.*, *J. Phys. A: Math. Gen.* **39**, L515 (2006).
- [29] M. Caprio, P. Cejnar, and F. Iachello, *Ann. Phys. (N.Y.)* **323**, 1106 (2008).
- [30] P. Cejnar and P. Stránský, *Phys. Rev. E* **78**, 031130 (2008).
- [31] P. Stránský, M. Macek, and P. Cejnar, *Ann. Phys. (N.Y.)* **345**, 73 (2014); P. Stránský *et al.*, *ibid.* **356**, 57 (2015).
- [32] P. Stránský and P. Cejnar, *Phys. Lett. A* **380**, 2637 (2016).
- [33] R.H. Dicke, *Phys. Rev.* **93**, 99 (1954).
- [34] K. Hepp and E. H. Lieb, *Ann. Phys. (N.Y.)* **76**, 360 (1973).
- [35] Y.K. Wang and F.T. Hioe, *Phys. Rev. A* **7**, 831 (1973).
- [36] C. Emary and T. Brandes, *Phys. Rev. Lett.* **90**, 044101 (2003); *Phys. Rev. E* **67**, 066203 (2003).
- [37] T. Brandes, *Phys. Rev. E* **88**, 032133 (2013).
- [38] M.A. Bastarrachea-Magnani, S. Lerma-Hernández and J.G. Hirsch, *Phys. Rev. A* **89** 032101; 032102 (2014).
- [39] M.A. Bastarrachea-Magnani, S. Lerma-Hernández and J.G. Hirsch, *J. Stat. Mech.* 093105 (2016).
- [40] C.M. Lóbez and A. Relaño, *Phys. Rev. E* **94**, 012140 (2016).
- [41] M. Kloc, P. Stránský, and P. Cejnar, *Ann. Phys. (N.Y.)* **382**, 85 (2017).
- [42] M. Kloc, P. Stránský and P. Cejnar, *J. Phys. A: Math. Theor.* **50** 315205 (2017).
- [43] M. Tavis and F. W. Cummings, *Phys. Rev* **170**, 379 (1968).
- [44] F. Dimer *et al.*, *Phys. Rev. A* **75**, 013804 (2007).
- [45] Z. Zhiqiang *et al.*, *Optica* **4**, 424 (2017).
- [46] P. Cejnar and P. Stránský, *Phys. Scr.* **91**, 083006 (2016).
- [47] F. Leyvraz and W.D. Heiss, *Phys. Rev. Lett.* **95**, 050402 (2005); P. Ribeiro, J. Vidal and R. Mosseri, *Phys. Rev. Lett.* **99**, 050402 (2007).
- [48] A. Relaño *et al.*, *Phys. Rev. A* **78**, 060102(R) (2008).
- [49] V.M. Bastidas *et al.*, *Phys. Rev. Lett.* **112**, 140408 (2014).
- [50] W. Kopylov and T. Brandes, *New J. Phys.* **17**, 103031 (2015).
- [51] A. Peres, *Phys. Rev. A* **30**, 1610 (1984).
- [52] T. Gorin *et al.*, *Phys. Rep.* **435**, 33 (2006).
- [53] A. Goussev *et al.*, *Scholarpedia*, 7(8):11687 (2012).
- [54] S. Lerma-Hernández *et al.*, arXiv:1710.05937 [quant-ph] (2017).
- [55] P. Bocchieri and A. Loinger, *Phys. Rev.* **107**, 337 (1957); L.S. Schulman, *Phys. Rev. A* **18**, 2379 (1978).
- [56] A. Peres, *Phys. Rev. Lett.* **53**, 1711 (1984).
- [57] P. Stránský, P. Hruška, P. Cejnar, *Phys. Rev. E* **79**, 066201 (2009).

Bibliography

- [1] M. Kloc, P. Stránský, and P. Cejnar, *Ann. Phys. (N.Y.)* **382**, 85 (2017).
- [2] M. Kloc, P. Stránský, and P. Cejnar, *J. Phys. A: Math. Theor.* **50**, 315205 (2017).
- [3] M. Kloc, P. Stránský, and P. Cejnar, arXiv:1805.06285 [quant-ph] (2018).
- [4] S. Sachdev, *Quantum Phase Transitions* (Cambridge Univ. Press, Cambridge, 2011).
- [5] *Understanding Quantum Phase Transitions*, edited by L.D. Carr (CRC, Boca Raton, 2011).
- [6] J. Hertz, *Phys. Rev. B* **14**, 1165 (1976).
- [7] E. Ising, *Z. Phys.* **31**, 253 (1925).
- [8] L. Onsager, *Phys. Rev.* **65**, 117 (1944).
- [9] R. Gilmore, D. H. Feng, *Nucl. Phys. A* **301**, 189 (1979).
- [10] F. Iachello, A. Arima, *The Interacting Boson Model* (Cambridge Univ. Press, Cambridge, 1987).
- [11] B. D. Kern, R. L. Mlekodaj, G. A. Leander, M. O. Kortelahti, E. F. Zganjar, R. A. Braga, R. W. Fink, C. P. Perez, W. Nazarewicz, and P. B. Semmes, *Phys. Rev. C* **36**, 1514 (1987).
- [12] F. Iachello, R. D. Levine, *Algebraic Theory of Molecules* (Oxford Univ. Press, Oxford, 1995).
- [13] A. Frank, P. van Isacker, *Symmetry Methods in Molecules and Nuclei* (México D. F.: S y G editores, 2005).
- [14] H. J. Lipkin, N. Meshkov, and N. Glick, *Nucl. Phys. A* **62** 188 (1965).
- [15] R. H. Dicke, *Phys. Rev.* **93**, 99 (1954).
- [16] P. Cejnar, *J. Phys.: Conf. Ser.* **322**, 012012 (2011).
- [17] R. Gilmore, *Catastrophe Theory for Scientists and Engineers* (New York: Wiley, 1981).

- [18] P. Cejnar, M. Macek, S. Heinze, J. Jolie, and J. Dobeš, *J. Phys. A: Math. Gen.* **39**, L515 (2006).
- [19] M. A. Caprio, P. Cejnar, and F. Iachello, *Ann. Phys.* **323**, 1106 (2008).
- [20] P. Cejnar, P. Stránský, *Phys. Rev. E* **78**, 031130 (2008).
- [21] P. Stránský, M. Macek, and P. Cejnar, *Ann. Phys.* **345**, 73 (2014).
- [22] P. Stránský, M. Macek, A. Leviatan, and P. Cejnar, *Ann. Phys.* **356**, 57 (2015).
- [23] P. Cejnar, P. Stránský, and M. Kloc, *Phys. Scr.* **90**, 114015 (2015).
- [24] P. Stránský, P. Cejnar, *Phys. Lett. A* **380**, 2637 (2016).
- [25] L. van Hove, *Phys. Rev.* **89**, 1189 (1953).
- [26] Guohong Li, A. Luican, J. M. Lopes dos Santos, A. H. Castro Neto, A. Reina, J. Kong, and E. Y. Andrei, *Nature Physics* **6**, 109 (2010).
- [27] M. S. Child, T. Weston, and J. Tennyson, *Mol. Phys.* **96**, 371 (1999).
- [28] N. F. Zobov, S. V. Shirin, O. L. Polyansky, J. Tennyson, P. F. Coheur, P. F. Bernath, M. Carleer, and R. Colin, *Chem. Phys. Lett.* **414**, 193 (2005).
- [29] D. A. Sadovskii, B. I. Zhilinskií, *Mol. Phys.* **104**, 2595 (2006) .
- [30] M. S. Child, *Adv. Chem. Phys.* **136**, 39 (2007).
- [31] D. Larese, F. Iachello, *J. Mol. Struct.* **1006**, 611 (2011).
- [32] J. R. Cary, D. F. Escande, and J. L. Tennyson, *Phys. Rev. A* **34**, 4256 (1986).
- [33] J. L. Tennyson, J. R. Cary, and D. F. Escande, *Phys. Rev. Lett.* **56**, 2117 (1986).
- [34] T. Brandes, *Phys. Rev. E* **88**, 032133 (2013).
- [35] M. A. Bastarrachea-Magnani, S. Lerma-Hernández, and J. G. Hirsch, *Phys. Rev. A* **89** 032101; 032102 (2014).
- [36] Y. K. Wang, F. T. Hioe, *Phys. Rev. A* **7**, 831 (1973).
- [37] K. Hepp, E.H. Lieb, *Phys. Rev. A* **8**, 2517 (1973).
- [38] K. Hepp, E. H. Lieb, *Ann. Phys. (N.Y.)* **76**, 360 (1973).
- [39] M. Gross, S. Haroche, *Phys. Rep.* **93**, 301 (1982).
- [40] *Super-radiance: Multiatomic Coherent Emission*, edited by M. G. Benedict (Taylor & Francis, New York, 1996).
- [41] A. Volya, V. Zelevinsky, *J. Opt. B: Quantum Semiclass. Opt.* **5**, S450 (2003).
- [42] N. Auerbach, V. Zelevinsky, *Rev. Prog. Phys.* **74**, 106301 (2011).
- [43] H. Eleuch, I. Rotter, *Eur. Phys. J. D* **68**, 74 (2014).

- [44] K. Cong, Q. Zhang, Y. Wang, G. T. Noe, A. Belyanin, and J. Kono, *J. Opt. Soc. Am. B* **33**, C80 (2016).
- [45] C. Emary, T. Brandes, *Phys. Rev. Lett.* **90**, 044101 (2003).
- [46] M. Tavis, F. W. Cummings, *Phys. Rev.* **170**, 379 (1968).
- [47] P. Cejnar, P. Stránský, *Phys. Lett. A* **381**, 984 (2017).
- [48] M. A. Bastarrachea-Magnani, S. Lerma-Hernández, and J.G. Hirsch, *J. Stat. Mech.* **2016**, 093105 (2016).
- [49] P. Pérez-Fernández, A. Relaño, *Phys. Rev. E* **96**, 012121 (2017)
- [50] K. Baumann, C. Guerlin, F. Brennecke, and T. Esslinger, *Nature* **464**, 1301 (2010).
- [51] K. Baumann, R. Mottl, F. Brennecke, and T. Esslinger, *Phys. Rev. Lett.* **107**, 140402 (2011).
- [52] K. Rzazewski, K. Wodkiewicz, and W. Zakowicz, *Phys. Rev. Lett.* **35**, 432 (1975).
- [53] M. J. Bhaseen, J. Mayoh, B. D. Simons, and J. Keeling *Phys. Rev. A* **85**, 013817 (2012).
- [54] Z. Zhiqiang, C. H. Lee, R. Kumar, K. J. Arnold, S. J. Masson, A. S. Parkins, and M. D. Barrett , *Optica* **4**, 424 (2017).
- [55] A. Peres, *Phys. Rev. Lett.* **53**, 1711 (1984).
- [56] O. Babelon, L. Cantini, and B. Douçot, *J. Stat. Mech.* **2009**, P07011 (2009).
- [57] D. J. Rowe, P. Rochford, and J. Repka, *J. Math. Phys. (N.Y.)* **29**, 572 (1988).
- [58] M. Macek, J. Dobeš, P. Stránský, and Pavel Cejnar, *Phys. Rev. Lett.* **105**, 072503 (2010).
- [59] J. J. Duistermaat, *Commun. Pure Appl. Math.* **33**, 687 (1980).
- [60] R. Cushman, J. J. Duistermaat, *Bull. Am. Math. Soc.* **19**, 474 (1988).
- [61] E. Schmidt, *Mathematische Annalen* **63**, 433 (1906).
- [62] M. Kloc, Diploma thesis, Charles University (2013).
- [63] C. H. Bennett, D. P. DiVincenzo, J. Smolin, and W. K. Wootters, *Phys. Rev. A* **54**, 3824 (1996).
- [64] C. H. Bennett, G. Brassard, S. Popescu, B. Schumacher, J. Smolin, and W. K. Wootters, *Phys. Rev. Lett.* **76**, 722 (1996).
- [65] S. Hill, W. K. Wootters, *Phys. Rev. Lett.* **78**, 26 (1997).
- [66] W. K. Wootters, *Phys. Rev. Lett.* **80**, 10 (1997).
- [67] X. Wang, K. Mølmer, *Eur. Phys. J. D* **18**,385 (2002).

- [68] A. Osterloh, L. Amico, G. Falci, and R. Fazio, *Nature* **416**, 608 (2002).
- [69] T. J. Osborne, M. A. Nielsen, *Phys. Rev. A* **66**, 032110 (2002).
- [70] G. Vidal, J. I. Latorre, E. Rico, and A. Kitaev, *Phys. Rev. Lett* **90**, 227902 (2003).
- [71] J. I. Latorre, E. Rico, and G. Vidal, *Quant. Inf. and Comp.* **4**, 48 (2004).
- [72] N. Lambert, C. Emary, and T. Brandes, *Phys. Rev. Lett* **92**, 073602 (2004).
- [73] N. Lambert, C. Emary, and T. Brandes, *Phys. Rev. A* **71**, 053804 (2005).
- [74] J. Vidal, S. Dusuel, and T. Barthel, *J. Stat. Mech.*, P01015 (2007).
- [75] L. Bakemeier, A. Alvermann, and H. Fehske, *Phys. Rev. A* **85**, 043821 (2012).
- [76] L. Bakemeier, A. Alvermann, and H. Fehske, *Phys. Scr.* **2015**, 014001 (2015).
- [77] K. Sengupta, S. Powell and S. Sachdev, *Phys. Rev. A* **69**, 053616 (2004).
- [78] P. Calabrese, J. Cardy, *Phys. Rev. Lett.* **96**, 136801 (2006).
- [79] L.F. Santos and F. Pérez-Bernal, *Phys. Rev. A* **92**, 050101(R) (2015).
- [80] L.F. Santos, M. Távora and F. Pérez-Bernal, *Phys. Rev. A* **94**, 012113 (2016).
- [81] P. Pérez-Fernández, , P. Cejnar, J. M. Arias, and J. Dukelsky, *Phys. Rev. A* **83**, 033802 (2011).
- [82] F. Pérez-Bernal and L.F. Santos, *Fortschr. Phys.* **65**, 1600035 (2017).
- [83] S. Lerma-Hernández, J. Chávez-Carlos, M. A. Bastarrachea-Magnani, L. F. Santos, and J. G. Hirsch, *arXiv:1710.05937 [quant-ph]* (2017).
- [84] S. Lerma-Hernández, J. Chávez-Carlos, M. A. Bastarrachea-Magnani, B. López-del-Carpio, and J. G. Hirsch, *AIP Conference Proceedings* **1950**, 030002 (2018).

List of Abbreviations

A	-	Atomic (phase)
D	-	Dicke (phase)
EDM	-	Extended Dicke model
ESQPT	-	Excited-state quantum phase transition
F	-	Field (phase)
IBM	-	Interacting Boson model
LMG	-	Lipkon-Meshkov-Glick model
N	-	Normal (phase)
QPT	-	Quantum phase transition
RWA	-	Rotating wave approximation
S	-	Saturated (phase)
TC	-	Tavis-Cummings (phase)
TPT	-	Thermal phase transition

List of Publications

1. **Quantum quench dynamics in Dicke superradiance models**

M. Kloc, P. Stránský, P. Cejnar
accepted by Physical Review A,
14 pages, regular article

<https://arxiv.org/abs/1805.06285>

2. **Excited-state quantum phase transitions and their manifestations in an extended Dicke model**

P. Stránský, M. Kloc, P. Cejnar
AIP Conference Proceedings 1912 (2017) 020018
10 pages, conference contribution

<https://aip.scitation.org/doi/abs/10.1063/1.5016143>

3. **Monodromy in Dicke superradiance**

M. Kloc, P. Stránský, P. Cejnar
Journal of Physics A 50 (2017) 31
14 pages, regular article

<http://iopscience.iop.org/article/10.1088/1751-8121/aa7a95/meta>

<https://arxiv.org/abs/1702.07224>

4. **Quantum phases and entanglement properties of an extended Dicke model**

M. Kloc, P. Stránský, P. Cejnar
Annals of Physics 382 (2017) 85
34 pages, regular article

<https://www.sciencedirect.com/science/article/pii/S0003491617301112>

<https://arxiv.org/abs/1609.02758>

5. **Excited-state quantum phase transitions in finite many-body systems**

P. Cejnar, P. Stránský, M. Kloc
Physica Scripta 90 (2015) 114015
7 pages, conference contribution

[http://iopscience.iop.org/article/10.1088/0031-8949/90/11/114015/
meta](http://iopscience.iop.org/article/10.1088/0031-8949/90/11/114015/meta)